# Improved Understanding of Multicentury Greenland Ice Sheet Response to Strong Warming in the Coupled CESM2-CISM2 with Regional Grid Refinement

Ziqi Yin[1], Adam R Herrington[2], Rajashree Datta[3], Aneesh C. Subramanian[4], Jan Thérèse Maria Lenaerts[5], and Andrew Gettelman[6]

[1]University of Colorado, Boulder
[2]National Center for Atmospheric Research
[3]NASA Goddard Space Flight Center
[4]University of Colorado
[5]University of Colorado Boulder
[6]Pacific Northwest National Laboratory

March 05, 2024

**Abstract**

The simulation of ice sheet-climate interaction such as surface mass balance fluxes are sensitive to model grid resolution. Here we simulate the multicentury evolution of the Greenland Ice Sheet (GrIS) and its interaction with the climate using the Community Earth System Model version 2.2 (CESM2.2) including an interactive GrIS component (the Community Ice Sheet Model v2.1 [CISM2.1]) under an idealized warming scenario (atmospheric CO2 increases by 1% yr-1 until quadrupling the pre-industrial level and then is held fixed). A variable-resolution (VR) grid with 1/4* regional refinement over broader Arctic and 1* resolution elsewhere is applied to the atmosphere and land components, and the results are compared to conventional 1* lat-lon grid simulations to investigate the impact of grid refinement. An acceleration of GrIS mass loss is found at around year 110, caused by rapidly increasing surface melt as the ablation area expands with associated albedo feedback and increased turbulent fluxes. Compared to the 1* runs, the VR run features slower melt increase, especially over Western and Northern Greenland, which slope gently towards the peripheries. This difference pattern originates primarily from the weaker albedo feedback in the VR run, complemented by its smaller cloud longwave radiation. The steeper VR Greenland surface topography favors slower ablation zone expansion, thus leading to its weaker albedo feedback. The sea level rise contribution from the GrIS in the VR run is 53 mm by year 150 and 831 mm by year 350, approximately 40% and 20% smaller than the 1* runs, respectively.

# Improved Understanding of Multicentury Greenland Ice Sheet Response to Strong Warming in the Coupled CESM2-CISM2 with Regional Grid Refinement

**Ziqi Yin[1], Adam R. Herrington[2], Rajashree Tri Datta[1], Aneesh Subramanian[1], Jan T. M. Lenaerts[1], and Andrew Gettelman[3]**

[1]Department of Atmospheric and Oceanic Sciences, University of Colorado Boulder, Boulder, CO, USA
[2]National Center for Atmospheric Research, Boulder, CO, USA
[3]Pacific Northwest National Laboratory, Richland, WA, USA

**Key Points:**

- For the first time, a variable-resolution atmosphere is coupled with the ocean and sea ice components in CESM with a dynamic GrIS
- Slower Greenland surface melt increase is detected in the Arctic-refined simulation compared with simulations using a conventional 1° grid
- The steeper VR GrIS surface topography favors slower ablation zone expansion, leading to weaker albedo feedback and slower melt increase

Corresponding author: Ziqi Yin, Ziqi.Yin@colorado.edu

## Abstract

The simulation of ice sheet-climate interaction such as surface mass balance fluxes are sensitive to model grid resolution. Here we simulate the multicentury evolution of the Greenland Ice Sheet (GrIS) and its interaction with the climate using the Community Earth System Model version 2.2 (CESM2.2) including an interactive GrIS component (the Community Ice Sheet Model v2.1 [CISM2.1]) under an idealized warming scenario (atmospheric $CO_2$ increases by 1% $yr^{-1}$ until quadrupling the pre-industrial level and then is held fixed). A variable-resolution (VR) grid with 1/4° regional refinement over broader Arctic and 1° resolution elsewhere is applied to the atmosphere and land components, and the results are compared to conventional 1° lat-lon grid simulations to investigate the impact of grid refinement. An acceleration of GrIS mass loss is found at around year 110, caused by rapidly increasing surface melt as the ablation area expands with associated albedo feedback and increased turbulent fluxes. Compared to the 1° runs, the VR run features slower melt increase, especially over Western and Northern Greenland, which slope gently towards the peripheries. This difference pattern originates primarily from the weaker albedo feedback in the VR run, complemented by its smaller cloud longwave radiation. The steeper VR Greenland surface topography favors slower ablation zone expansion, thus leading to its weaker albedo feedback. The sea level rise contribution from the GrIS in the VR run is 53 mm by year 150 and 831 mm by year 350, approximately 40% and 20% smaller than the 1° runs, respectively.



## Plain Language Summary

As one of the main contributors to global sea level rise, the Greenland Ice Sheet (GrIS) has been losing mass as an accelerating rate during the recent decades. Better understanding the interactions between the GrIS and the climate can help us make more reliable future projections of GrIS mass loss. To simulate these interactions, a fully coupled model infrastructure is necessary. Additionally, the model resolution needs to be higher enough to resolve the surface topography and processes like orographic precipitation. This study applies a 1/4° Arctic refined grid to an Earth System Model which includes an interactive GrIS model to simulate multicentury GrIS evolution under an idealized warming scenario, and compares the results with simulations using a lower resolution grid. We show that the simulation with the grid refinement has a slower increase in melt, thus contributing less to global sea level rise. This difference mainly results from the slower ablation zone expansion and thus weaker albedo feedback in the Arctic refined grid simulation, with the smaller cloud longwave radiation playing a supporting role.


## 1 Introduction

Recent data reveals an acceleration in the mass loss from the Greenland Ice Sheet (GrIS), averaging 257 Gt $yr^{-1}$ between 2017 and 2020, a sevenfold increase compared to the early 1990s (Otosaka et al., 2023). GrIS mass loss is driven both by atmospheric warming (Hanna et al., 2021), which increases surface melt and meltwater runoff (Trusel et al., 2018), and oceanic warming, which has caused glacier acceleration and enhanced ice discharge (Straneo & Heimbach, 2013). Though the ice discharge increase played a stronger role in GrIS mass loss between 1992 and 2018 (66 ± 8%), during the last two decades, surface mass balance (SMB) decrease has become the dominant contributor due to increased surface melt (Enderlin et al., 2014; Mouginot et al., 2019). The exceptional summer surface melting causes a maximum mass loss of 444 Gt $yr^{-1}$ in 2019 (Tedesco & Fettweis, 2020). The interactions between the ice sheet, the atmosphere, and the ocean can initiate feedback effects, further amplifying or dampening the mass imbalance signals. One important positive feedback is the albedo/melt feedback. As snow or ice melts, the surface with lower albedo, e.g., warmer snow/firn/bare ice/ground, is exposed, lead-

ing to increased absorption of shortwave radiation and thus further promoting melt of the original and nearby regions. Many other feedbacks can enhance or restrain GrIS mass loss, such as geometry/SMB feedbacks (Fyke et al., 2018). So, to better model the evolution of the GrIS, a coupled model that can represent these bidirectional interactions/feedbacks is necessary.

The accuracy of simulated SMB is sensitive to model grid resolution, especially in regions with steep and complex terrains. The mountainous GrIS margins, also where steep topographic gradients are located, are too smooth in conventional 1° to 2° global climate models (GCMs). Such models fail to resolve processes like orographic precipitation and allow too much moisture to penetrate into the ice sheet interior, causing positive precipitation biases (Pollard & Groups, 2000). Research has shown that, with a higher horizontal resolution, the orographic precipitation can be better resolved and thus the positive precipitation biases can be reduced (van Kampenhout et al., 2019; Herrington et al., 2022). In addition, the ablation zone around the GrIS margins where the majority of summer melt occurs can be as narrow as tens of kilometers, which cannot be resolved by 1° to 2° grids. It is therefore important to have a finer resolution for more accurate representation of GrIS SMB processes.

Modeling with a variable-resolution grid has several advantages. Though rapidly developing, widespread use of global-uniform high-resolution climate models (e.g., models participated in the High-Resolution Model Intercomparison Project (HighResMIP; Haarsma et al., 2016)) is still impractical due to current limits in computational resources. Regional climate models (RCMs), usually in one-way nesting mode, offer regional high resolution with a lower computational cost. However, they need boundary conditions from GCMs or reanalysis, thus not allowing two-way interactions across the boundaries. Moreover, the boundary conditions derived from a separate host model can introduce inconsistencies between the host model and the RCM. Variable-resolution modeling overcomes some of these challenges using a unified modeling framework, which can model the two-way interactions between the regional and large scales and is more computationally efficient.

The application of regional grid refinement in GCMs can be dated back to the early use of stretched grids in late 1970s (Schmidt, 1977; Staniforth & Mitchell, 1978) and now it has been developed in many state-of-the-art GCMs (Harris et al., 2016; Zängl et al., 2022; Sakaguchi et al., 2023; Tang et al., 2023). In the Community Earth System Model, version2 (CESM2; Danabasoglu et al., 2020), regional grid refinement is supported by the spectral-element (SE; Lauritzen et al., 2018) dynamical core of the atmospheric component. Studies have proven its consistency in modeling global circulation and climatology (Zarzycki et al., 2015; Gettelman et al., 2018), fidelity in representing tropical and extra-tropical cyclones (Zarzycki & Jablonowski, 2014; Zarzycki et al., 2014; Zarzycki, 2016) and regional climate, especially at regions with mountains or steep terrain (Rhoades et al., 2016; Huang et al., 2016; Huang & Ullrich, 2017; Wu et al., 2017; Rhoades et al., 2018; Rahimi et al., 2019; Bambach et al., 2022; Wijngaard et al., 2023). The variable-resolution CESM2 (VR-CESM2) has also been applied to the polar regions. van Kampenhout et al. (2019) shows that the simulation of GrIS SMB in the accumulation zone is significantly improved by using two regionally refined grids over the GrIS at 1/2° and 1/4°. In addition to improvements where a refined resolution is applied to the GrIS, the simulated clouds and precipitation in the Arctic is also substantially improved with two Arctic-refined meshes, one at 1/4° and another with an additional 1/8° patch of refinement over Greenland (Herrington et al., 2022). For the Antarctic, 1/4° regional refinement over the Antarctic Ice Sheet and the surrounding Southern Ocean indicates both improvements, mainly in temperature and wind fields, and degradations, primarily related to surface melt, over the Antarctic Ice Sheet compared to 1° CESM2 (Datta et al., 2023). The VR-CESM2 in the above-mentioned studies are run in the coupled land-atmosphere

mode following the Atmospheric Model Intercomparison Project protocols (AMIP; Gates, 1992).

This study analyzes the results from a set of simulations using the fully coupled configuration of CESM2 with a dynamic GrIS under an idealized strong warming scenario. A variable-resolution grid, which has 1/4° regional refinement over the broader Arctic region and 1° horizontal resolution elsewhere, is applied to the atmosphere and land components of CESM2. Unlike prior VR-CESM2 studies, we include coupling to a dynamic ocean model, similar to Tang et al. (2023). This work aims to: first, investigate multicentury future GrIS evolution, and second, compare the results of the variable-resolution run with those of global 1° resolution runs, to see where the regional refinement provides added value. Section 2 documents the model, grids, and experiment design information. Section 3 presents the results and the comparison of the simulations. Finally, in Section 4, a discussion and conclusions are provided.

## 2 Methods

### 2.1 Model Description

CESM2 is an Earth System Model (ESM) maintained by the National Center for Atmosphere Research, which consists of atmosphere, ocean, land, sea ice, and land ice components and can be run in configurations with different levels of complexity. The ocean component, Parallel Ocean Program version 2 (POP2; Smith et al., 2010), runs on a nominal 1° displaced-pole grid with 60 vertical levels. Sea ice is represented by the Community Ice CodE for sea ice version 5 (CICE5; Hunke et al., 2015), using the same horizontal grid as POP2. Land processes are simulated by the Community Land Model version 5 (CLM5; Lawrence et al., 2019), using the same horizontal grid as the atmosphere model. CLM5 also embeds the Model for Scale Adaptive River Transport (MOSART; Li et al., 2013) to handle land surface runoff based on topographic gradients.

The GrIS is simulated using the Community Ice Sheet Model, version 2.1 (CISM2.1; Lipscomb et al., 2019), using a 4-km rectangular grid with 11 terrain-following vertical levels. To simulate ice flow, a depth-integrated higher-order approximation (Goldberg, 2011) of the Stokes equations is employed in the velocity solver. The parameterization of basal sliding utilizes a pseudo-plastic sliding law and a simple basal hydrology model, following the approach described by Aschwanden et al. (2016). In this parameterization, the yield stress is determined by the till friction angle and the effective pressure, with the former being influenced by the bedrock elevation through a fixed piecewise linear relationship. The bedrock evolution due to Glacial Isostatic Adjustment (GIA) effect is governed by an Elastic plate Lithosphere plus Relaxing Asthenosphere (ELRA) model (see for example Rutt et al., 2009). This study accounts for calving processes through a flotation criterion, where floating ice is instantaneously discharged to the ocean.

Two versions of CESM2 are used for the simulations in this study: CESM2.1 and CESM2.2. In CESM2.1, the atmosphere is simulated with the Community Atmosphere Model version 6 (CAM6; Gettelman et al., 2019), using the Finite-Volume (FV; Lin, 2004) dynamical core, with 32 vertical hybrid pressure-sigma levels. The CAM6 physical parameterization package is described in detail in Gettelman et al. (2019). CESM2.1 is one of the ESMs to contribute to the Coupled Model Intercomparison Project Phase 6 (CMIP6; Eyring et al., 2016) and the Ice Sheet Model Intercomparison Project for CMIP6 (ISMIP6; Nowicki et al., 2016).

CESM2.2 uses the same CAM physics parameterizations and vertical grid, but contains enhanced functionality for the SE dynamical core, including the capability for running VR grids (Herrington et al., 2022). The CMIP6 CESM2.1 simulations using CAM-FV are not reproducible in CESM2.2, and therefore two versions of the model are required to compare the VR grids to the CMIP6 workhorse configuration.

### 2.2 Surface Mass Balance

The GrIS SMB simulated in CESM2 is the sum of ice accumulation and ice ablation. The SMB processes of the GrIS are aggregated in CLM5, which includes up to 10 vertical snowpack layers with a maximum total depth of 10-m water equivalent. Only snow accumulated over the 10-m threshold contributes to ice accumulation. Ice ablation incorporates surface ice melt as well as sublimation. Part of rain and melt water penetrates into the snow layers and refreezes, as another source of ice, while the rest runs off to the ocean. Melt energy is calculated from the sum of net surface radiation, latent and sensible turbulent heat fluxes, and ground heat fluxes at the atmosphere-snow interface. To account for sub-grid variability, each glaciated grid cell in CLM5 is subdivided into 10 elevation classes (ECs) with fixed elevation ranges (Lipscomb et al., 2013; Sellevold et al., 2019). The area fractions of the ECs are calculated from the higher-resolution CISM topography. For each EC, the surface energy fluxes and SMB are calculated independently by downscaling atmospheric variables. Near-surface temperature and downward longwave radiation are downscaled with fixed lapse rates (6 K $km^{-1}$ and 32 W $m^{-2}$ $km^{-1}$). Relative humidity is assumed uniform vertically. Due to a CAM6 model bias leading to excessive rainfall over the GrIS, precipitation is repartitioned based on near-surface temperature thresholds: precipitation falls as snow when the temperature is below -2°C, as rain when the temperature is above 0°C, and as a linear combination of snow and rain for temperatures between -2°C and 0°C.

Though with biases such as overestimated precipitation, CESM2.1 at 1° with a fixed GrIS geometry simulates a realistic historical Greenland SMB (van Kampenhout et al., 2020). When coupled to CISM2, higher Greenland SMB and interannual variability is simulated, partly due to the different ice sheet topography (Muntjewerf, Petrini, et al., 2020).

### 2.3 Coupling Scheme

In the model framework, the GrIS is interactively coupled to the other Earth system components. CISM2 receives the CLM5 SMB for each EC, and is then downscaled by the coupler using a trilinear remapping scheme (bilinear horizontally and linear vertically), with corrections of accumulation and ablation to conserve global water mass. As the ice sheet evolves, the coupler updates the EC fractional glacier coverage in each CLM5 grid cell based on the CISM2 ice sheet extent at annual frequency. The mean surface elevation in CAM6 is manually updated based on the CISM2 topography every 20 model years, using the CESM topography software (Lauritzen et al., 2015). Surface runoff from CLM5, basal melt and ice discharge from CISM2 constitute the freshwater fluxes inputted into the ocean, which are supplied as salinity anomalies. More detailed description of the coupling scheme can be found in Muntjewerf et al. (2021).

### 2.4 Grids

The variable-resolution grid we use here - the `Arctic` grid (Fig.1a), is a 1° SE grid with 1/4° regional refinement over the broader Arctic region (Herrington et al., 2022). It is generated by using the software package SQuadgen (https://github.com/ClimateGlobalChange/squadgen). The global 1° resolution runs use the latitude-longitude 1° grid, referred to as `f09`, supported by the FV dynamical core. Figure 1b and 1c show a snapshot of the surface topography over the GrIS before the start of the warming scenario for the `f09` grid and the `Arctic` grid, respectively. The `Arctic` grid represents more detailed Greenland topography (e.g., the south dome and ice sheet periphery) with a more accurate ice sheet mask. The surface elevation differences between two grids can range up over 700 m (Fig.1d), which is partly caused by the initial ice sheet volume difference. The physics time step of the `Arctic` simulations is 450 s, which is a 4× reduction relative to the default 1800 s time step used in the 1° grid.

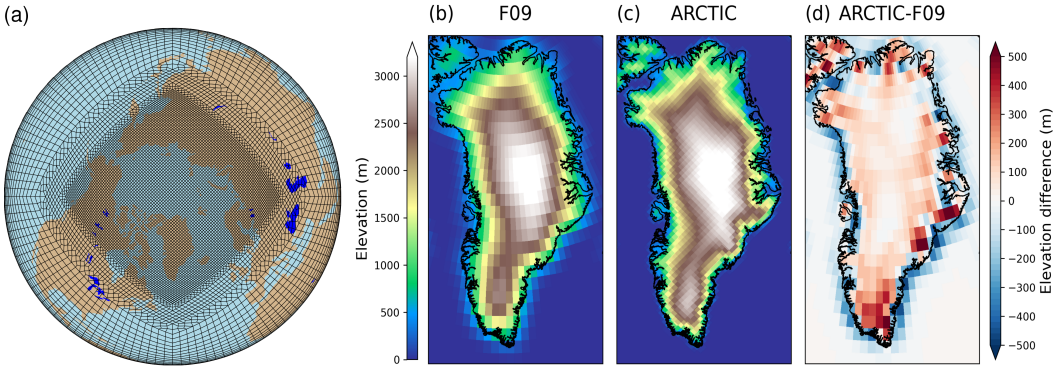


**Figure 1.** (a) The `Arctic` grid (Herrington et al., 2022). Note what is shown is the element grid; the computational grid has 3 × 3 independent grid points per element. Surface topography (m) of the Greenland Ice Sheet represented by (b) the `f09` grid, (c) the `Arctic` grid, and (d) their difference before the start of the warming scenario.

### 2.5 Experiment Design

First, a pre-industrial simulation was branched off from the last leg of the spun-up pre-industrial Earth system/ice sheet state (Lofverstrom et al., 2020). A series of experiments were ran to bring the top of atmosphere radiative forcing into balance using common tuning parameters such `clubb_gamma` (Guo et al., 2015). The tuned pre-industrial control was then run for 180 years until the GrIS achieved near equilibrium state. Then an idealized warming scenario was started, in which the atmospheric $CO_2$ concentration increased by 1% per year until reaching 4× the pre-industrial value after 140 years, followed by a 210-year simulation with the fixed 4× pre-industrial $CO_2$ concentration (Fig.2a). This set of simulations using the `Arctic` grid (hereafter `ARCTIC`) was compared to two sets of simulations under the same forcing but using the f09 grid, in the older CESM2.1 code base. One is from Muntjewerf, Sellevold, et al. (2020) (hereafter `F09M`). In this code base, to reduce the too-high SMB over portions of the GrIS in CESM2 coupled runs, the cold rain (< -2°C) produced by CAM immediately runs off to the ocean instead of being converted to snow by CLM. Also, to facilitate low level convergence and precipitation near the coasts, the sub-grid roughness over Greenland is artificially increased. To limit the differences between models, we ran another set of f09 simulation using CESM2.1 but without these two adjustments (hereafter `F09`).

### 2.6 Analysis

#### *2.6.1 Atmospheric and Oceanic Circulation Metrics*

The Greenland blocking index (GBI) uses the 500-hPa geopotential height ($Z_{500}$) to estimate blocking over the Greenland region (Fang, 2004). Strong and persistent blocking can result in extreme summer melt at the ice sheet surface (Hanna et al., 2014). The revised GBI from Hanna et al. (2018) is used, which is calculated by subtracting the area-averaged $Z_{500}$ over the Arctic region (60°N to 80°N) from the area-averaged $Z_{500}$ over the Greenland region (60°N to 80°N, and 80°W to 20°W). Then the resulting time series is standardized with respect to the last 80 years of the pre-industrial period. Here only the JJA mean GBI is considered.

The North Atlantic Meridional Overturning Circulation (NAMOC) index measures the strength of the North Atlantic Meridional Overturning Circulation, which is predicted to be weaken with the addition of GrIS meltwater to the ocean (Vizcaíno et al., 2010;

Muntjewerf, Sellevold, et al., 2020). The NAMOC index is defined as the maximum of the overturning stream function north of 28°N and below 500-m depth.

#### *2.6.2 Melt/albedo Feedback*

We use the melt/albedo feedback (or albedo feedback) calculations following Box et al. (2012). The albedo feedback ($\alpha_{feedback,a}$) is quantified by regression between 20 annual samples of detrended anomalies of summer (JJA) average net shortwave radiation ($SW_{net}$) and near-surface air temperature ($T_{air}$) in units of W m$^{-2}$ K$^{-1}$, with anomalies indicated by the $'$ character in $\Delta'$:

$$\alpha_{feedback,a} = \Delta' SW_{net} / \Delta' T_{air} \tag{1}$$

The regression uses annual pairs of anomalies instead of successive values in the time series. This pairing is illustrated in Fig.S1. Since this definition of albedo feedback does not include lags that may cause albedo change (e.g., a low albedo year pre-conditions the next year for low albedo), an alternative formulation of albedo feedback (referred to as the bulk albedo feedback ($\alpha_{feedback,b}$) is considered, which is the change in $SW_{net}$ over the change of $T_{air}$:

$$\alpha_{feedback,b} = \Delta SW_{net} / \Delta T_{air} \tag{2}$$

#### *2.6.3 Equilibrium Line Altitude (ELA)*

Equilibrium line has zero annual mean SMB, separating the ice sheet accumulation zone and the ablation zone. To calculate the average ELA of the GrIS in our model, we define the following algorithm: Loop through the ablation grids using the annual mean SMB field. If any of the neighboring grids has positive SMB, compute the elevation where SMB equals zero using the two SMB and elevation values of this positive SMB grid (with grid area $a_p$) and the ablation grid (with grid area $a_n$). Save this computed elevation as one ELA value, with an approximate length of the shared edge of the two grids as the weight. The approximate edge length is calculated by $(\sqrt{a_n}+\sqrt{a_p})/2$. The final average ELA is the length-weighted average of all the saved ELA values.

## 3 Results

### 3.1 Response of the GrIS in the VR Run

To help visualize the spatial change patterns through time and later analyze the differences between `F09M`, `F09`, and `ARCTIC`, we will focus on three time periods: year 131-150, year 231-250, and year 331-350. Year 131-150 represents the $CO_2$ stabilization period. Year 231-250 and year 331-350 are one and two centuries after, respectively, with the latter also representing the end of our simulation.

Since atmospheric $CO_2$ radiative forcing is nearly logarithmic in concentration, the 1% yr$^{-1}$ increase of $CO_2$ causes a nearly linear rise in the annual average near-surface temperature (0.3 K per decade; Fig.2b). By $CO_2$ stabilization, the temperature increase is 5.0 K over the GrIS. Polar amplification (the ratio of Arctic and global temperature increase) is 1.8. GrIS amplification (the ratio of GrIS and global temperature increase) is much smaller (1.1) due to its perennial ice and snow cover. After $CO_2$ stops increasing, the annual average near-surface temperature still rises, albeit more slowly (0.2 K per decade) due to oceanic warming, adding another 3.8 K by the end of the simulation. The relatively small area of the GrIS results in a larger variability of annual average near-surface temperature compared to the Arctic and global mean.

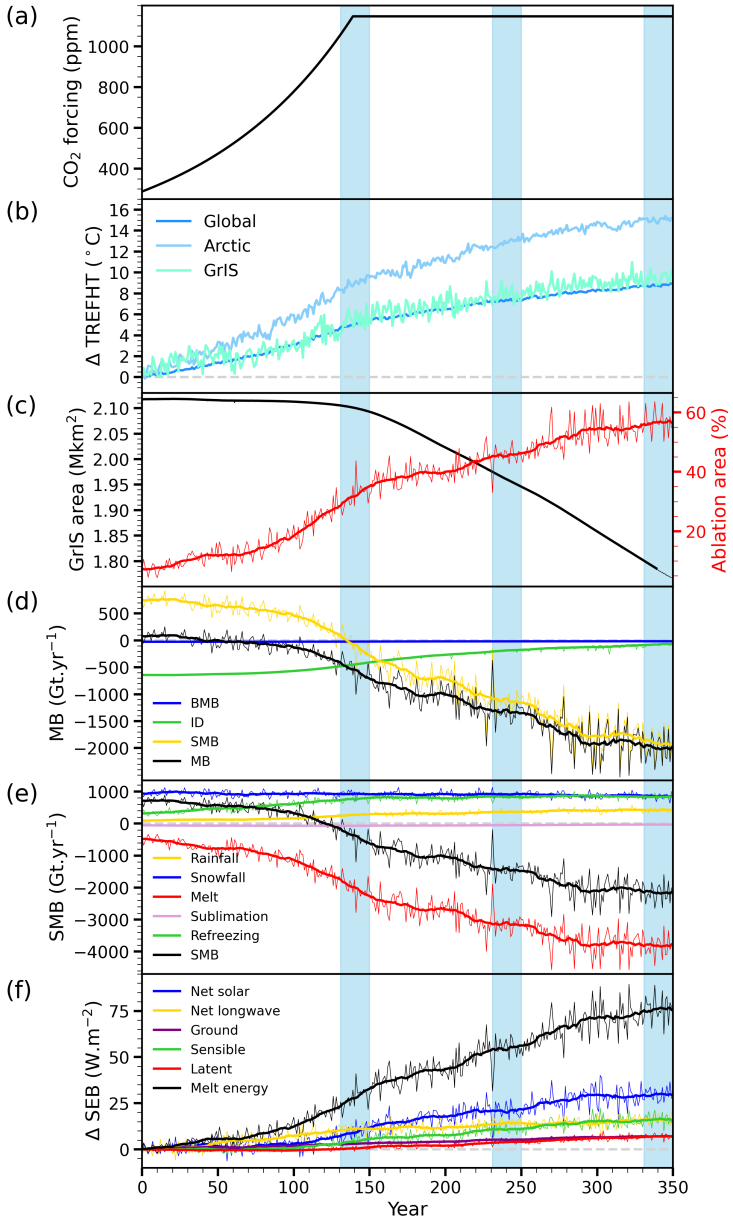


**Figure 2.** Evolution of (a) atmospheric $CO_2$ concentration (ppm), (b) global, GrIS, and Arctic region (north of 60°N) annual near-surface temperature anomaly with respect to the end of pre-industrial period (°C), (c) GrIS total area (left vertical axis, million km$^2$) and ablation area (%; as percentage of total ice sheet area), (d) mass balance (MB, black) and components (Gt yr$^{-1}$), (e) SMB (black) and components (Gt yr$^{-1}$), and (f) JJA anomaly of surface energy balance components compared to the end of pre-industrial period (W m$^{-2}$). The thick lines in (c)-(f) show the 20-year running means. The blue shaded periods are used in subsequent analysis.

Figure 2d shows the evolution of the GrIS-integrated mass balance and components. A similar pattern is found in Muntjewerf, Sellevold, et al. (2020). The mass loss accelerates after about 110 years, rising from 2.4 Gt yr$^{-2}$ before year 110 to 13.0 Gt yr$^{-2}$ between years 111 to 150. Then, after $CO_2$ stabilization, the GrIS mass loss decelerates

gradually, combined with larger oscillations and variability. With the mass loss, the ice sheet area shrinks, decreasing from 2.1 × $10^6$ km$^2$ to 1.8 × $10^6$ km$^2$ (Fig.2c). The cumulative contribution to global mean sea level rise (GMSLR) is 53 mm by year 150 and 831 mm by year 350 (Table 1). The decreasing SMB dominates the mass balance trend (Fig.2d), which becomes negative at around year 130. Ice discharge gradually decreases as marine-terminating outlet glaciers thin, decelerate, and even transition to land-terminating glaciers.

**Table 1.** Annual Rate of Mass Loss (mm yr$^{-1}$), Cumulative GrIS Mass Loss (mm), Mass Balance Components (Gt yr$^{-1}$), GrIS Area ($10^6$ km$^2$), and GrIS Volume ($10^6$ km$^3$).

| | Last 20 yrs of CTRL | | | Years 131-150 | | | Years 231-250 | | | Years 331-350 | | |
|---|---|---|---|---|---|---|---|---|---|---|---|---|
| | F09M | F09 | ARCTIC | F09M | F09 | ARCTIC | F09M | F09 | ARCTIC | F09M | F09 | ARCTIC |
| Annual mass loss | -0.04 | -0.10 | -0.05 | 2.08 | 2.06 | 1.48 | 5.28 | 4.49 | 3.50 | 6.36 | 5.93 | 5.40 |
| Cumulative mass loss | -0.8 | -2.0 | -1.1 | 97 | 84 | 53 | 501 | 447 | 344 | 1,098 | 976 | 831 |
| MB | 19 | 41 | 23 | -776 | -761 | -542 | -1,974 | -1,669 | -1,285 | -2,376 | -2,195 | -2,001 |
| SMB | 616 | 723 | 685 | -380 | -319 | -72 | -1,797 | -1,463 | -1,081 | -2,284 | -2,097 | -1,909 |
| ID | 573 | 654 | 636 | 376 | 420 | 448 | 161 | 187 | 187 | 78 | 81 | 77 |
| BMB | -24 | -27 | -25 | -20 | -22 | -22 | -16 | -18 | -18 | -14 | -16 | -16 |
| GrIS area | 1.97 | 2.00 | 2.02 | 1.92 | 1.96 | 1.99 | 1.77 | 1.80 | 1.83 | 1.60 | 1.64 | 1.66 |
| GrIS volume | 3.23 | 3.27 | 3.25 | 3.20 | 3.24 | 3.23 | 3.05 | 3.10 | 3.12 | 2.81 | 2.89 | 2.93 |

Notes: Mass Balance (MB) = Surface Mass Balance (MB) - Ice Discharge (ID) + Basal Melt Balance (BMB). Variables in this table are calculated using CISM2 outputs.

The accelerating SMB trend (decreasing) is dominated by the surface melt trend. Figure 2e shows the evolution of SMB components. Surface melt increases profoundly: the annual surface melt during year 131-150 and year 331-350 are more than four times and eight times larger than the pre-industrial value, respectively (Table 2). The total precipitation increases from the start due to increased rainfall but decreases during the last century as the decreasing trend of snowfall dominates. By the end of the simulation, the precipitation is about a quarter higher than the pre-industrial value (Table 2). Though snowfall remains the major precipitation type, the proportion of liquid phase precipitation gradually grows through time, making up nearly one-third of the total precipitation by the end of the simulation (Table 2). Refreezing increases before $CO_2$ stabilization as more liquid water is available from both increased rainfall and surface melt, and then becomes relatively stable due to saturated snow cover. This is also reflected by the refreezing capacity - defined as the fraction of refreezing to available liquid water - decreasing from 55.4% pre-industrial to 19.7% by the end of the simulation (Table 2). Sublimation is relatively small throughout the simulation, so is not discussed further.

**Table 2.** Annual Ice Sheet-Integrated Surface Mass Balance and Components Mean (Gt yr$^{-1}$).

| | Last 20 yrs of CTRL | | | Years 131-150 | | | Years 231-250 | | | Years 331-350 | | |
|---|---|---|---|---|---|---|---|---|---|---|---|---|
| | F09M | F09 | ARCTIC | F09M | F09 | ARCTIC | F09M | F09 | ARCTIC | F09M | F09 | ARCTIC |
| SMB (4km) | 616 | 723 | 685 | -380 | -319 | -72 | -1,797 | -1,463 | -1,081 | -2,284 | -2,097 | -1,909 |
| SMB | - | 701 | 651 | -745 | -620 | -369 | -2,213 | -1,752 | -1,398 | -2,552 | -2,254 | -2,159 |
| Precipitation | 942 | 1,026 | 955 | 1,047 | 1,273 | 1,200 | 1,106 | 1,374 | 1,277 | 1,156 | 1,308 | 1,265 |
| Snowfall | 850 | 934 | 869 | 782 | 961 | 930 | 699 | 932 | 913 | 695 | 819 | 849 |
| Rain | 92 | 92 | 86 | 265 | 312 | 270 | 406 | 443 | 364 | 461 | 488 | 416 |
| Refreezing | 142 | 295 | 307 | 680 | 872 | 758 | 784 | 956 | 824 | 781 | 1,019 | 830 |
| Melt | 485 | 476 | 468 | 2,147 | 2,400 | 1,986 | 3,662 | 3,606 | 3,083 | 4,009 | 4,073 | 3,806 |
| Sublimation | - | 52 | 57 | 60 | 53 | 70 | 34 | 34 | 52 | 19 | 19 | 32 |
| Rain (%) | 9.8 | 9.0 | 9.0 | 25.4 | 24.5 | 22.5 | 36.8 | 32.2 | 28.5 | 39.9 | 37.4 | 32.9 |
| Refreezing (%) | 24.6 | 51.9 | 55.4 | 28.2 | 32.2 | 33.6 | 19.3 | 23.6 | 23.9 | 17.5 | 22.3 | 19.7 |

Notes: SMB (4km) is calculated using CISM2 outputs. The other variables are calculated using CLM5 outputs. SMB = Snowfall + Refreezing – Melt – Sublimation. Rain (%) = Rain * 100 / (Snowfall + Rain). Refreezing (%) = Refreezing * 100 / (Rain + Melt).

316 The enhanced surface melt greatly reduces the SMB over the periphery of the GrIS.
317 Fig.3f-h show the spatial distribution of SMB difference compared to the pre-industrial
318 period, indicating the largest SMB decrease occurs along the southeast and west mar-
319 gins ($>$ 5,000 mm yr$^{-1}$ by the end of the simulation). In the ice sheet interior, SMB in-
320 creases due to the locally enhanced hydrological cycle. This spatial pattern of SMB changes
321 results in a similar spatial pattern of the ice sheet thickness changes, with slight thick-
322 ening over the high interior and significant thinning towards the margins (Fig.3j-l). The
323 largest thinning along the western margins can exceed 1000 m by the end of the simu-
324 lation. The surface ice velocity decreases at the ice sheet margins due to the thinning
325 of outlet glaciers, though generally, the surface ice velocity increases due to the steeper
326 surface slopes caused by the thickness changes (Fig.3n-p).

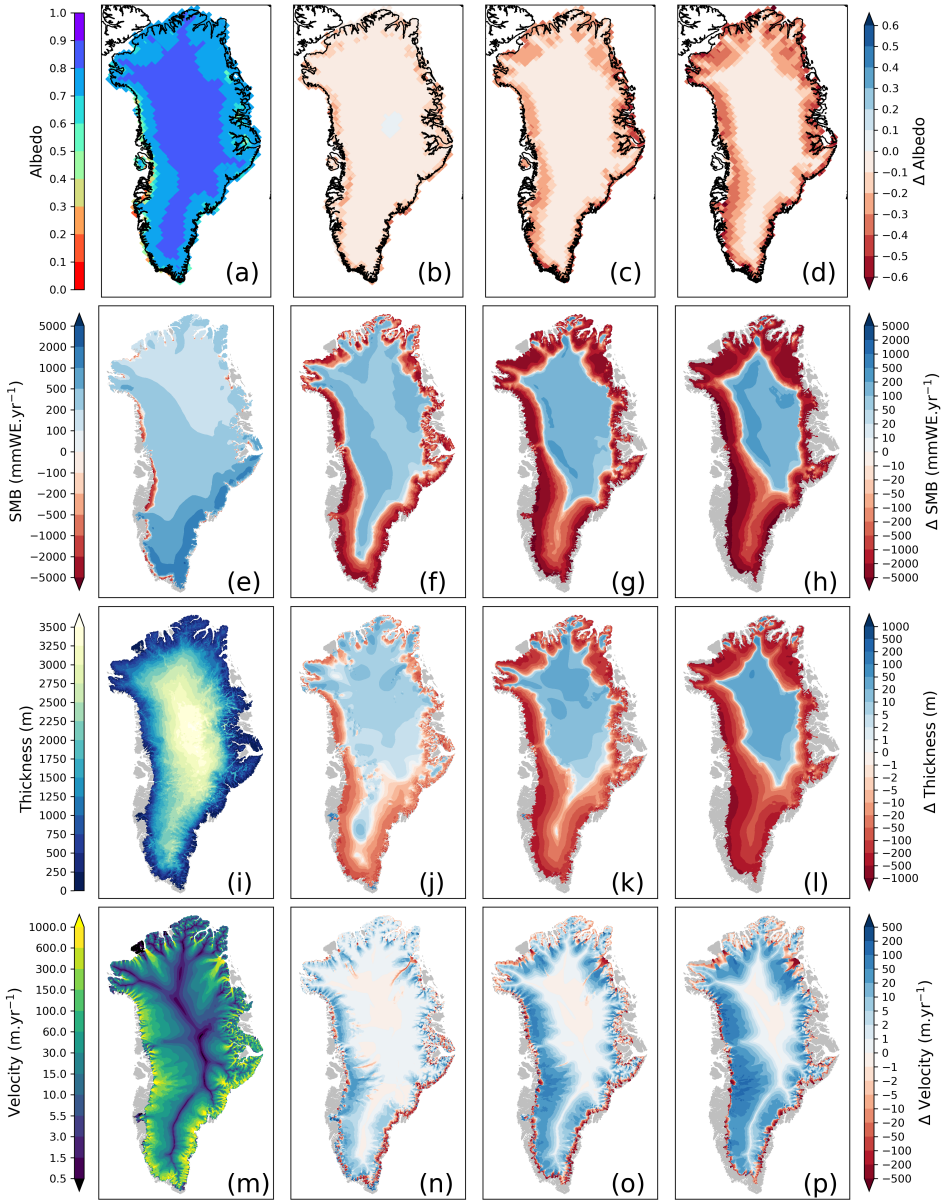


**Figure 3.** Spatial distribution over the GrIS for pre-industrial (first column) and differences with respect to the former by model years 131-150 (second column), 231-250 (thrid column) and 331-350 (forth column). (a-d) JJA mean albedo, (e-h) annual mean surface mass balance (mmWE $yr^{-1}$) with accumulation zones (SMB $> 0$) and ablation zones (SMB $< 0$), (i-l) ice sheet thickness (m), and (m-p) surface velocity (m $yr^{-1}$).

### 3.2 Drivers for melt changes

The spatiotemporal evolution of surface energy balance (SEB) components over the GrIS provides an explanation for the main physical drivers of accelerating surface melt. Figure 2f shows the summer (JJA) average anomalies of surface energy terms compared to the pre-industrial period. During the first century, the enhancement in net longwave radiation (less longwave cooling) from increased atmospheric temperature and cloudiness (Fig.S2a) provides most of the additional melting energy. The increased net short-

wave radiation is dampened by reduced incoming shortwave radiation (Fig.S2b) resulting from enhanced cloudiness (Fig.S2a). At around year 110, the contribution of net shortwave radiation to the melt energy increases rapidly, surpassing net longwave radiation at around year 148, and becoming the dominant melt energy contributor. At the end of the simulation, net shortwave radiation provides 37.3% of the total additional melt energy (Table 3). The accelerated net shortwave radiation increase at about year 110 is speculated to be due to the activation of the melt/albedo feedback. We find that the accelerated net shortwave radiation and melt increase coincides with a faster increase of ablation area (Fig.2c). As the ablation zone expands, darker surfaces with lower albedo are exposed, which absorbs more shortwave radiation and further enhances surface melting. The decrease of surface albedo mainly occurs within the ablation zones, with little change in the ice sheet interior (Fig.3b-d). The ice sheet hypsometry also contributes to the accelerated expansion of the ablation zone - the quasi-parabolic shape favors faster ablation area expansion as it approaches the interior plateau. The turbulent fluxes also increase at around year 110, although at slower speeds. As near-surface air temperature continues to rise, the surface temperature inversion becomes stronger, thus enhancing the turbulent fluxes. The contribution of sensible heat flux to total additional melt energy is comparable to the contribution of net longwave radiation by the end of the simulation (22.5% and 21.5%, respectively; Table 3). The latent heat flux becomes less negative through the simulation, which is potentially due to the decrease of sublimation as well as an increase in deposition and condensation. At the end of the simulation, 10.1% of the additional melt energy comes from latent heat flux (Table 3). The ground heat flux rises from negative to positive, which is potentially a result of more refreezing in the snow layer, and contributes 8.6% of the additional melt energy at the end of the simulation (Table 3).

**Table 3.** Summer GrIS-averaged Albedo, Near-Surface Temperature and Skin Temperature (°C), Incoming Shortwave Radiation, Incoming Longwave Radiation at the Surface, and Surface Energy Balance Components Mean (W $m^{-2}$).

| | Last 20 yrs of CTRL | | | Years 131-150 | | | Years 231-250 | | | Years 331-350 | | |
|---|---|---|---|---|---|---|---|---|---|---|---|---|
| | F09M | F09 | ARCTIC | F09M | F09 | ARCTIC | F09M | F09 | ARCTIC | F09M | F09 | ARCTIC |
| Albedo | 0.78 | 0.78 | 0.78 | 0.71 | 0.72 | 0.73 | 0.64 | 0.66 | 0.68 | 0.61 | 0.62 | 0.65 |
| $T_{2m}$ | -7.00 | -7.05 | -7.34 | -1.22 | -1.11 | -1.88 | 0.50 | 0.43 | -0.22 | 1.03 | 1.21 | 0.79 |
| $T_{skin}$ | -7.83 | -7.83 | -8.42 | -2.14 | -2.15 | -3.10 | -0.74 | -0.85 | -1.74 | -0.31 | -0.20 | -0.96 |
| $SW_{in}$ | 288.3 | 286.4 | 294.3 | 262.0 | 261.7 | 272.6 | 255.9 | 254.9 | 266.6 | 250.9 | 253.4 | 264.0 |
| $LW_{in}$ | 231.0 | 232.6 | 224.1 | 267.7 | 268.5 | 257.8 | 276.1 | 276.8 | 266.7 | 280.3 | 280.7 | 271.6 |
| Melt energy | 8.8 | 8.5 | 8.4 | 40.3 | 43.4 | 35.7 | 71.0 | 68.3 | 59.7 | 84.6 | 83.6 | 80.0 |
| $SW_{net}$ | 64.0 | 62.1 | 64.9 | 73.5 | 72.8 | 73.5 | 89.5 | 84.9 | 83.2 | 94.8 | 92.8 | 91.6 |
| $LW_{net}$ | -50.6 | -49.0 | -55.3 | -38.2 | -37.3 | -44.0 | -36.1 | -34.9 | -41.2 | -34.1 | -34.1 | -39.9 |
| SHF | 4.8 | 4.5 | 7.1 | 8.4 | 10.4 | 11.2 | 14.2 | 14.7 | 17.6 | 16.1 | 16.7 | 23.3 |
| LHF | -8.3 | -8.0 | -7.5 | -6.9 | -5.4 | -7.1 | -2.7 | -2.3 | -3.6 | -0.6 | 0.1 | -0.3 |
| GHF | -1.2 | -1.1 | -0.8 | 3.6 | 2.9 | 2.1 | 6.1 | 5.9 | 3.8 | 8.4 | 8.2 | 5.3 |

Notes: Melt energy = net shortwave radiation $SW_{net}$ + net longwave radiation $LW_{net}$ + sensible heat flux SHF + latent heat flux LHF + ground heat flux GHF.

To examine the role of large scale circulation on summer GrIS surface melt, we calculated the GBI. Figure 4a shows the evolution of the GBI for ARCTIC. There is a negative trend of the GBI before $CO_2$ stabilization, which indicates weakening summer blocking over the Greenland region. This agrees with the result of Sellevold and Vizcaíno (2020), which uses an AMIP style configuration of CESM2.1 under the same 1% $yr^{-1}$ $CO_2$ warming scenario. After $CO_2$ stabilization, there is no significant trend for GBI. Figure 4b shows the linear regression between GrIS-integrated JJA melt, and the JJA GBI. Both variables are filtered with a 10-year high-pass filter, thus representing the sub-decadal timescale. On sub-decadal timescales, the GBI explains 40% of the annual variability of summer surface melt. A more negative GBI results in less surface melt. Therefore, this indicates the GBI (more general the atmospheric circulation pattern) is not a driver of the melt

acceleration at about year 110, but actually counteracts part of the effect of global warming on the surface melt before $CO_2$ stabilization.

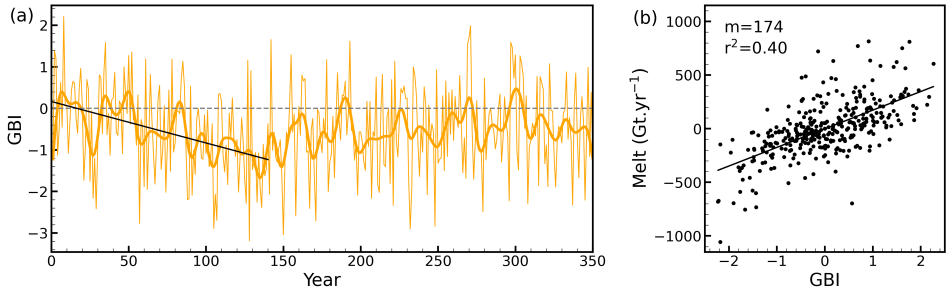


**Figure 4.** Evolution of the Greenland Blocking Index for `ARCTIC` (a), and the regression of JJA GrIS-integrated filtered surface melt (Gt $yr^{-1}$) onto JJA filtered Greenland Blocking Index (b). The thick orange line in (a) shows the 10-year low-pass filtered time series. The timescale of the filtered quantities effectively removes both the mean and the trend of each time series. Black line is drawn where the regression is significant, with an annotated m (slope), and $r^2$ for the explained variance for (b).

## 3.3 Impacts of Enhanced Resolution

### *3.3.1 Large-scale Climate*

Before delving into the simulated GrIS responses, we first compare the representations of large-scale climate conditions between the regionally-refined `ARCTIC` run and the 1° runs. Figure 5a-c show the summer mean 500 hPa geopotential height for `ARCTIC` during the three time periods - year 131-150, year 231-250, and year 331-350. As the atmosphere warms, the 500 hPa geopotential height increases over the northern high latitudes. The differences between `ARCTIC` and the 1° runs show a consistent pattern during each period (Fig.5d-i). Compared to `F09M` and `F09`, `ARCTIC` has significantly lower 500 hPa geopotential height over Greenland except for the period year 331-350 for `ARCTIC` and `F09M`, which possibly indicates weaker blocking and less anticyclonic flows over the GrIS in `ARCTIC`. This lower geopotential region in `ARCTIC` extends over the Canadian Archipelago during year 131-150. There is also significant higher geopotential over subpolar regions in `ARCTIC` compared to `F09M` and `F09`, especially during year 331-350.

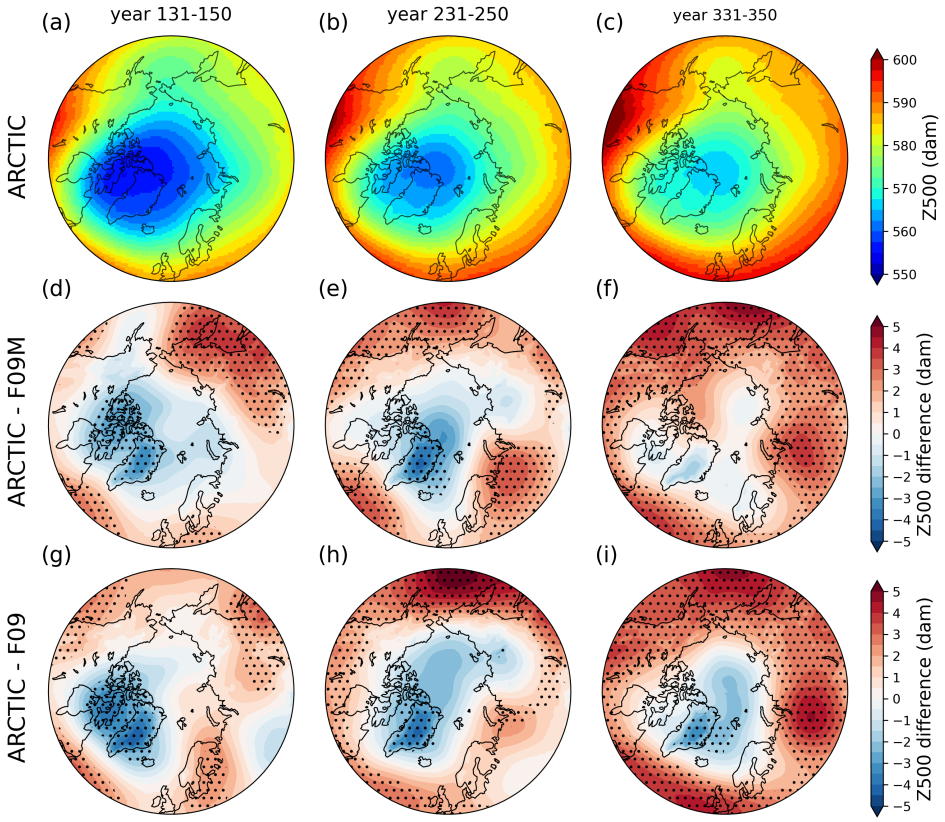


**Figure 5.** Northern hemisphere summer 500 hPa geopotential height (dam) of `ARCTIC` (a-c), and the difference between `ARCTIC` and `F09M` (d-f), `ARCTIC` and `F09` (g-i). The three columns from left to right represent averaged periods year 131-150, year 231-250, and year 331-350, respectively. Dotted regions are where the two simulations are significantly different ($p < 0.05$) by student t test.

Figure 6 compares the summer temperature over the northern hemisphere between `ARCTIC` and the 1° runs. The lower-troposphere summer virtual temperature, computed by equating a layer mean virtual temperature with the 500–1,000 hPa geopotential thickness, is higher in `ARCTIC` over much of the northern hemisphere (Fig.6a-f). This agrees with the common response to increasing horizontal resolution (also reducing physics time step) in general circulations models (GCMs) (Pope & Stratton, 2002; Roeckner et al., 2006) including CAM (Herrington & Reed, 2020): increasing the horizontal resolution warms the climate, since higher resolved vertical velocities generate more condensational heating. However, `F09M` and `F09` have warmer lower troposphere than `ARCTIC` centered over the GrIS, which also extends to Canadian Archipelago and Alaska during year 131-150 (Fig.6a,d) and to East Siberia during year 231-250 (Fig.6b,e). This spatial pattern of lower-troposphere virtual temperature differences agrees with that of the 500 hPa geopotential height difference, indicating that probably the stronger summer blocking over Greenland regions in `F09M` and `F09` causes the higher lower-troposphere virtual temperature there. Compared to the lower troposphere, the near-surface temperature difference shows a distinct spatial pattern with larger magnitudes (Fig.6g-l). Except for some terrestrial regions (e.g., parts of Siberia and Eurasia), `ARCTIC` is significantly cooler than `F09M` and `F09` at near-surface level. This results from the different pre-industrial climate, in which `ARCTIC` is cooler, likely due to increasing the albedo of snow over sea ice to tune this run. The regions where the lower troposphere is cooler in `ARCTIC` during year 131-150 and year

231-250 also have much lower near-surface temperature. However, the near-surface temperature differences over the GrIS are much smaller due to its perennial ice and snow cover. There are also regions at the ice sheet periphery that are warmer in ARCTIC. This is caused by the difference of cloud conditions, which is discussed in Section 3.3.3.

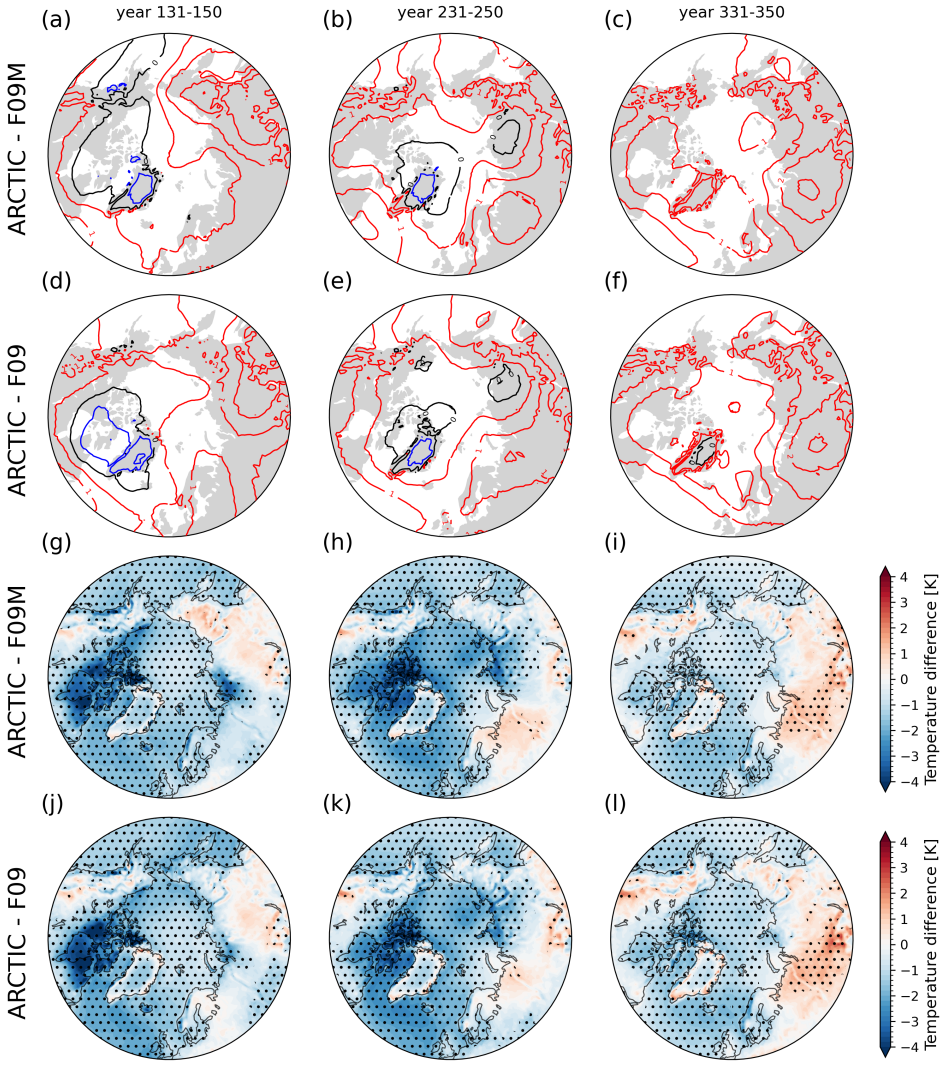


**Figure 6.** Northern hemisphere summer lower troposphere virtual temperature differences (K) between ARCTIC and F09M(a-c), ARCTIC and F09(d-f). Lower troposphere layer mean virtual temperature is derived from the 1,000–500 hPa geopotential thickness, using the hypsometric equation. Northern hemisphere summer near-surface air temperature differences (K) between ARCTIC and F09M(g-i), ARCTIC and F09(j-l). The three columns from left to right represent averaged periods year 131-150, year 231-250, and year 331-350, respectively. Dotted regions are where the two simulations are significantly different ($p < 0.05$) by student t test.

The NAMOC evolution is insensitive to the enhanced resolution in the atmosphere. The three simulations have very similar NAMOC index, and even their initial differences are diminished. During the period of $CO_2$ increase, the NAMOC weakens significantly (Fig.7a, with the NAMOC index decreasing by 0.14 Sv $yr^{-1}$, 0.13 Sv $yr^{-1}$, and 0.12 Sv

414 $yr^{-1}$ in `ARCTIC`, `F09M`, and `F09`, respectively. Then the NAMOC index gradually stabi-
415 lizes and remains at about 5 Sv for almost two centuries. We also compare the evolu-
416 tion of the NAMOC index with the total freshwater flux from the GrIS into the ocean
417 (Fig.7b). The total freshwater flux is calculated by adding up surface runoff, basal melt,
418 and solid ice discharge. The NAMOC index declines at the start of $CO_2$ increase, which
419 is much earlier than the rapid increase freshwater flux at around year 110, and remains
420 stable when the freshwater flux keeps increasing. This relationship is also found in sim-
421 ulations under SSP5-8.5 forcing (Muntjewerf, Petrini, et al., 2020), which suggests the
422 relatively limited role of additional freshwater input from the GrIS on NAMOC weak-
423 ening compared to global warming in CESM2.

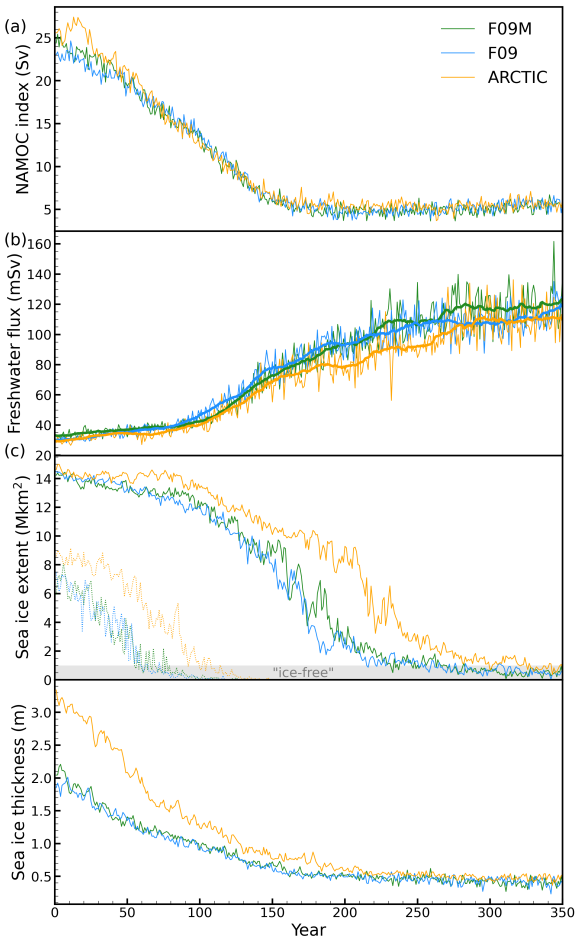


**Figure 7.** Evolution of the annual mean (a) NAMOC index (Sv), (b) total freshwater flux into the ocean (mSv), (c) Northern Hemisphere sea ice extent (million $km^2$; ice concentration > 15%), and (d) averaged sea ice thickness (m). The thick lines in (b) represent 20-year running means. The dotted lines in (c) represent September mean sea ice extent and the gray shaded range represents the "ice-free" condition.

424 Slower decline of Northern Hemisphere sea ice extent is found in `ARCTIC` compared
425 to the 1° runs (Fig.7c). In the 1° runs, the Arctic becomes ice-free (sea ice extent < one
426 million $km^2$) in September after about 60 years, while this happens about five decades
427 later in `ARCTIC`. There is an acceleration of annual sea ice decline ((Fig.7c)) at around

year 90 for all the simulations. This is possibly because the ice-free Arctic ocean absorbs more radiation, which stores more heat in the ocean and slows down sea ice formation in colder seasons, but the reason for the timing needs further investigation. Before the Arctic becomes ice-free all year round by the end of the simulation, `ARCTIC` has larger sea ice extent than the 1° runs due to its slower sea ice decline during the first two centuries. This is mostly driven by the larger initial sea ice thickness in `ARCTIC` of the warming scenario (Fig.7d), which is a result of increasing the albedo of snow over sea ice in `ARCTIC` during the tuning process.

#### *3.3.2 SMB Evolution and Ice Sheet Changes*

The evolution of ice sheet-integrated quantities in the three simulations follows a similar pattern but with different magnitudes and timing. Figure 8b compares the evolution of the GrIS-integrated SMB of the three simulations. Compared to the 1° runs, the SMB in `ARCTIC` decreases more slowly, such that by the end of the simulation, the drop of annual SMB in `ARCTIC` is 306 Gt $yr^{-1}$ and 226 Gt $yr^{-1}$ (∼10%) smaller than `F09M` and `F09`, respectively (Table 1). This SMB difference mainly results from the difference in melt, with `ARCTIC` generally producing less surface melt than `F09M` and `F09`, especially around the period year 180-260 (Fig.8a). During year 231-250, the GrIS-integrated melt in `F09M` and `F09` is 579 Gt $yr^{-1}$ and 523 Gt $yr^{-1}$ larger than `ARCTIC`, respectively (Table 1). The difference in precipitation is relatively small (Fig.8a). `F09` has larger precipitation than `ARCTIC`, which compensates some of its larger melt and results in smaller SMB difference. In `F09M`, the adjustments that direct cold-rain to surface runoff and increase sub-grid roughness over Greenland greatly reduce precipitation. Compared to `F09`, it causes a 204 Gt $yr^{-1}$ reduction of annual total precipitation averaged over the 350 years. The slower SMB decrease of `ARCTIC` causes slower decrease of MB (Fig.8c), and thus slower ice volume decrease (Fig.8d) and smaller global mean sea level rise (GMSLR) contribution (Fig.8e). Over the whole 350 years, `F09M` and `F09` contribute to 267 mm and 145 mm (∼20%) more GMSLR than `ARCTIC`, respectively (Table 1). We note the different initial ice volume and initial mass balance of the three simulations, which will be discussed in Section 4.

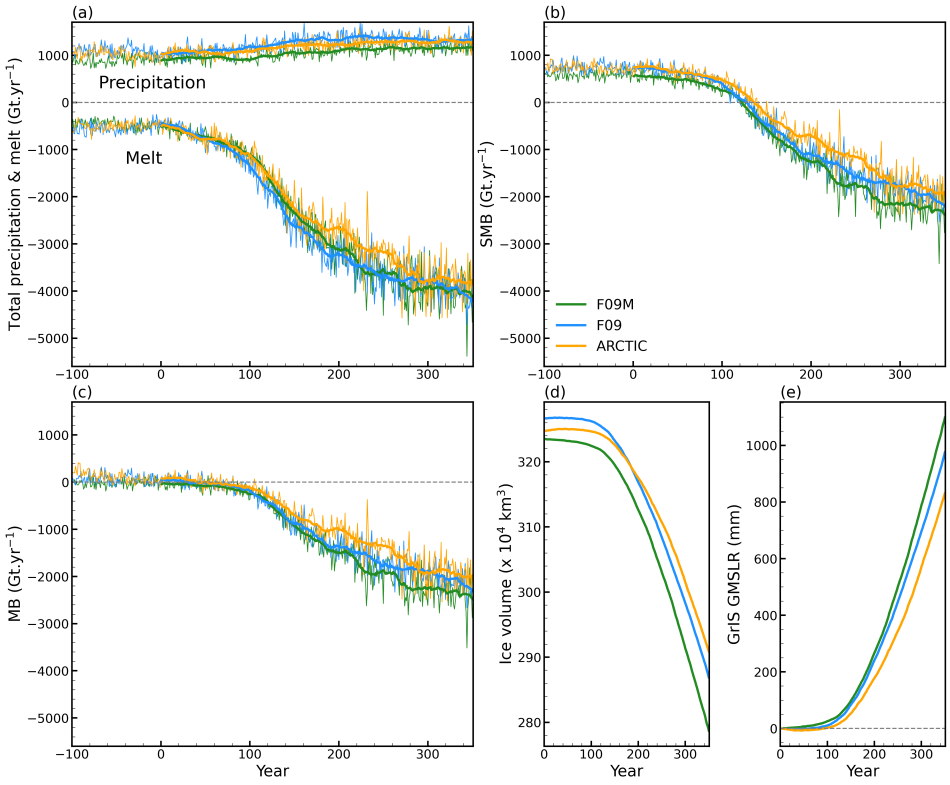


**Figure 8.** Evolution of GrIS-integrated (a) total precipitation and melt (Gt yr$^{-1}$), (b) SMB (Gt yr$^{-1}$), (c) MB (Gt yr$^{-1}$), (d) ice volume ($\times$ 10$^4$ km$^3$), and (e) accumulated contribution to global mean sea level rise (mm) for the three simulations. The thick lines in (a)-(c) represent 20-year running means.

Averaged over the whole 350 years, the smaller melt in `ARCTIC` is most significant along the ice sheet periphery in western and northern GrIS, where `F09M` and `F09` melt over 300 mm more ice each year (Fig.9c,d). The south tip shows the reverse of the larger spatial pattern, with more melt in `ARCTIC`. This is due to the weaker cloud shortwave cooling there in `ARCTIC` (discussed in Section 3.3.3). The spatial pattern of melt difference is consistent for `ARCTIC` compared to `F09M` and `F09` despite their different initial conditions (Fig.8d). The spatial pattern of total precipitation difference is almost the opposite for `ARCTIC` compared to `F09M` and `F09`, with the former having lower precipitation and the latter having larger precipitation centered over the south and southeast coasts (Fig.9a,b). Due to the smoother topography in the 1° grid, there is more moisture penetration into the ice sheet from southeast. For `F09M`, the effect of directing cold-rain to surface runoff and increasing sub-grid roughness is evident, which greatly reduces the total precipitation. Over the 350 years, weaker ice sheet thinning (difference $>$ 100 m) is found in `ARCTIC` especially along the western and northern peripheries compared to the 1° runs (Fig.9e,f). The larger precipitation in `F09` reinforces its smaller melt in the south tip, resulting in less ice sheet thinning there.

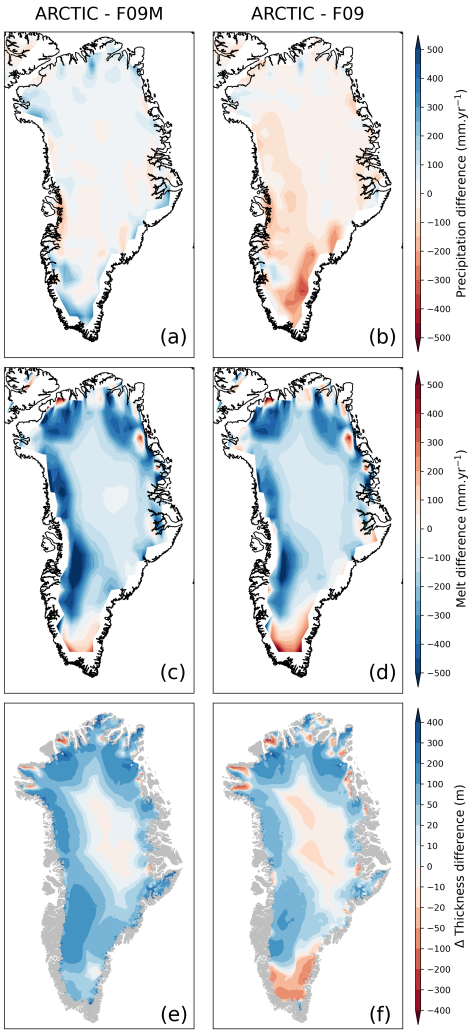


**Figure 9.** Maps of the difference between `ARCTIC` and `F09M` (left column), `ARCTIC` and `F09` (right column): (a-b) annual mean precipitation (mm $yr^{-1}$), (c-d) surface melt (mm $yr^{-1}$) averaged over the whole 350 years, and (e-f) ice thickness change (m) between the end of the simulation and the end of pre-industrial period. Blue color indicates more precipitation, less melt, or less thinning. For precipitation and melt, `ARCTIC` results are remapped to the `f09` grid for the comparison.

### *3.3.3 Surface Energy Balance*

To explain the differences in meltwater production between `ARCTIC` and the 1° runs, we examine how incident radiation is impacted by cloud conditions. Figure 10a,b illustrate the summer mean cloud fraction difference between `ARCTIC` and the 1° runs. There is a ring of cloud fraction surplus around the ocean perimeter of Greenland in `ARCTIC`, which is similar to previous findings in (Herrington et al., 2022). Lower cloud fraction in `ARCTIC` is found in the northern and southern peripheries, while in between the cloud fraction can be higher compared to the 1° runs, especially during year 231-250. This pattern is different to that in Herrington et al. (2022), where the smoother topography in lower resolution runs causes more moisture intrusion thus larger cloud fraction in the ice sheet interior. The higher pressure in the 1° runs over the GrIS (Fig.5) may contribute

to their lower cloud fraction by generating stronger large-scale subsidence and cloud dissipation. The spatial pattern of total cloud liquid water path (LWP) difference over the GrIS generally follows that of cloud fraction difference, except for the much larger LWP in the southern interior in `ARCTIC` (Fig.5c,d). The pattern of cloud difference impacts the incident radiation. In `ARCTIC`, the incident shortwave radiation is generally larger due to less cloud cover or thinner clouds, especially in northern Greenland and along the ice sheet margins (Fig.10e,f). At the same time, smaller incident longwave radiation is found all over the ice sheet for `ARCTIC` (Fig.10g,h), with the largest differences along the north and southeast margins. This is a combined effect of the cloud conditions and lower free atmosphere temperature over Greenland in `ARCTIC`.

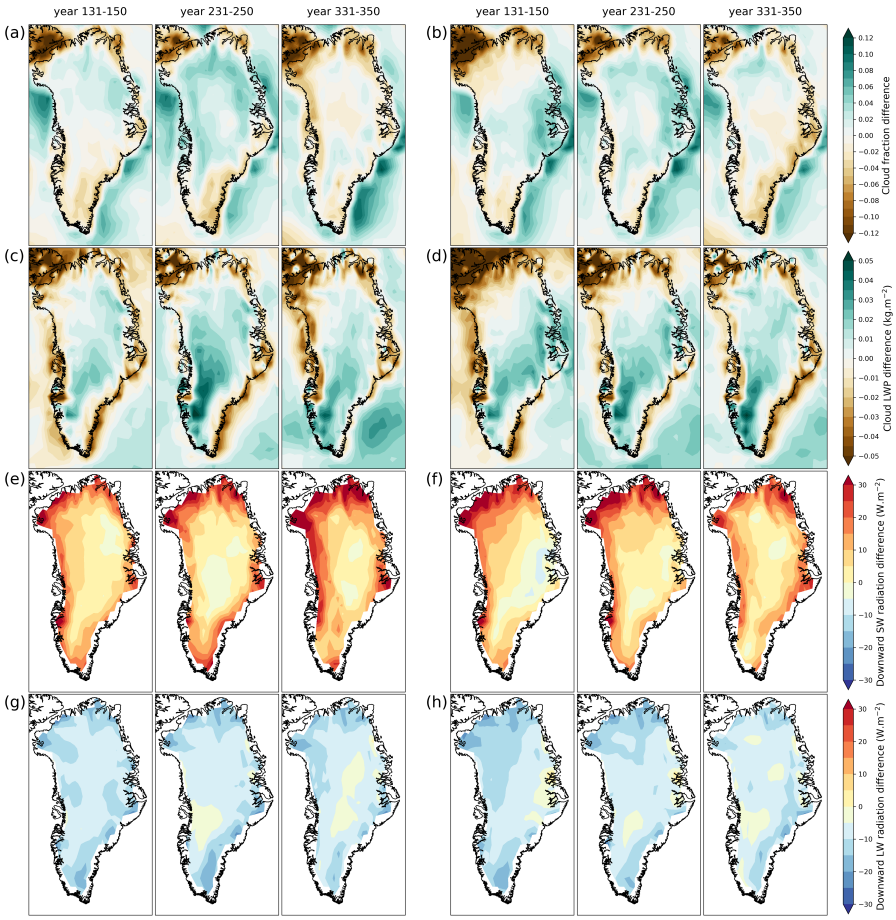


**Figure 10.** Maps of the difference between `ARCTIC` and `F09M` (left three columns), `ARCTIC` and `F09` (right three columns): (a-b) JJA mean cloud fraction, (c-d) total cloud liquid water path (kg m$^{-2}$), (e-f) downward shortwave radiation (W m$^{-2}$), and (g-h) downward longwave radiation (W m$^{-2}$) averaged over three periods: year 131-150, year 231-250, and year 331-350.

Differences in the representation of clouds and the resultant incident radiation have a direct impact on SEB terms and thus total energy available for melt. Despite the overall larger incident shortwave radiation in `ARCTIC`, especially along the ice sheet margins, it has smaller net shortwave radiation in the interior compared to the 1° runs, peaking at the gently sloping ice surface in the western and northern basins (or transitional area) (Fig.11a,b). Therefore, the albedo in these regions of `ARCTIC` must drop more slowly than

those in the 1° runs. The net shortwave radiation difference during year 131-150 is still small, and it becomes dominant in the SEB during year 231-250 and year 331-350. The spatial pattern of net longwave radiation difference (Fig.11c,d) is consistent with the pattern of incident longwave radiation (Fig.10g,h), suggesting the weaker cloud longwave warming effect in `ARCTIC`. The spatial pattern of differences in net longwave radiation is consistent through time. Compared to the radiative fluxes, the difference of turbulent fluxes between `ARCTIC` and the 1° runs is relatively small (Fig.11e-h). The above mentioned gently sloping ice surface in the western and northern basins also favors smaller sensible and latent heat fluxes in `ARCTIC`. Larger sensible heat flux is found in `ARCTIC` along the ice sheet margins especially during year 331-351, which originates from the higher near-surface temperature there (Fig.6g-l). The difference of ground heat flux is small between `ARCTIC` and the 1° runs (not shown). As the sum of the above SEB terms, the total melt energy difference has a spatial pattern that agrees with the averaged melt difference (Fig.9c,d). In the aggregate, the spatial distribution of the lower melt energy in `ARCTIC` (Fig.11a,b) mainly results from the combination of smaller net shortwave radiation due to higher surface albedo and smaller net longwave radiation due to lower cloud fraction.

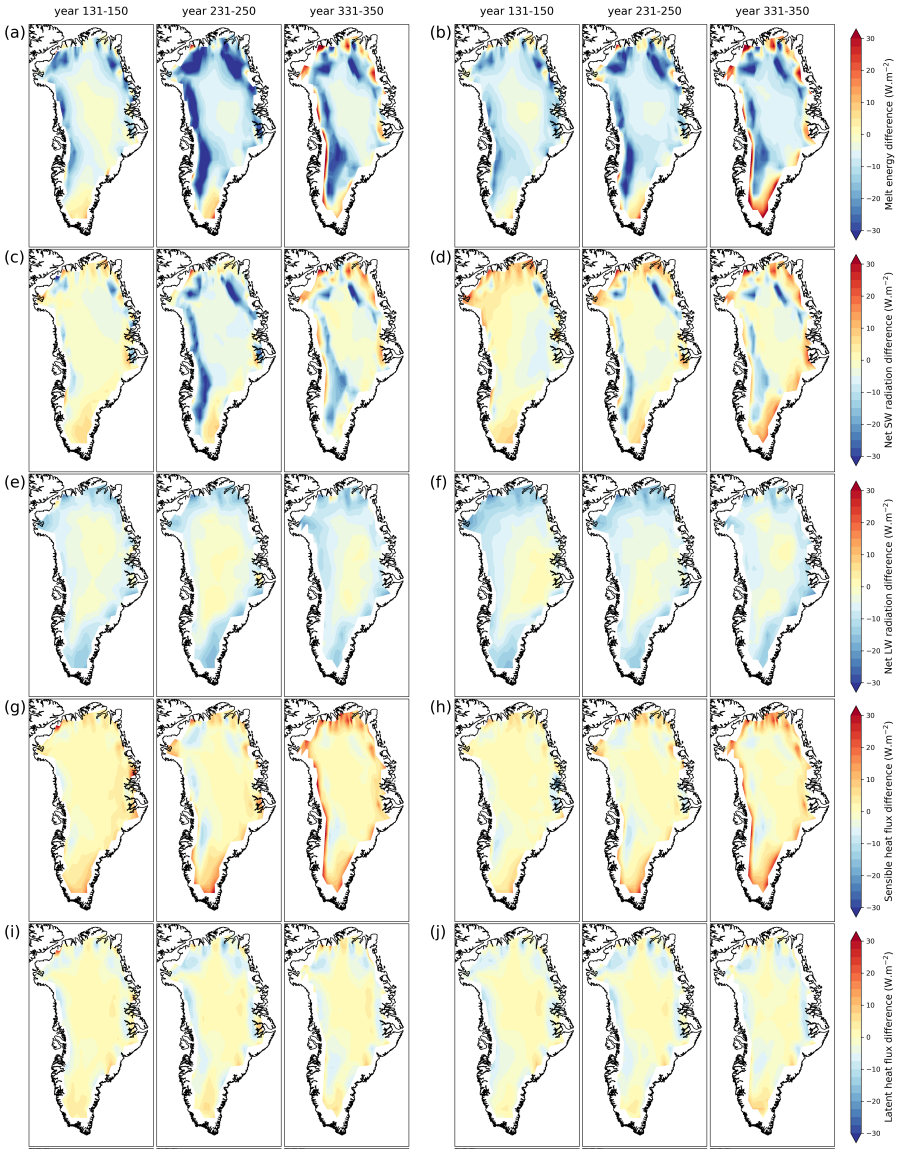


**Figure 11.** Maps of the difference between `ARCTIC` and `F09M` (left three columns), `ARCTIC` and `F09` (right three columns): (a-b) JJA mean total melt energy, (c-d) net shortwave radiation, (e-f) net longwave radiation, (g-h) sensible heat flux, and (i-j) latent heat flux averaged over three periods: year 131-150, year 231-250, and year 331-350 in the unit of W m$^{-2}$. Grids that do not have 100 percent ice fraction were masked out to avoid bias caused by comparing grids with different ice fraction.

### *3.3.4 Melt/albedo Feedback and the Impact of Ice Sheet Hypsometry*

We speculate that the slower decrease in albedo in `ARCTIC` is caused by a weaker albedo feedback. We first examine the bulk albedo feedback (Eq.2), which captures the long-term change in net shortwave radiation versus near-surface temperature when time-lags are considered. Over the whole 350 years, the bulk albedo feedback of `ARCTIC` (Fig.12a) and the 1° runs (not shown) is all positive over the GrIS, meaning more shortwave radiation is absorbed as near-surface temperature rises. The positive bulk albedo feedback is concentrated in the ablation zones, peaking in the lower elevations in the gently slop-

ing western and northern basins (> 15 W m$^{-2}$ K$^{-1}$). Figure 12b and 12c show the difference of the bulk albedo feedback between `ARCTIC` and `F09M`, `ARCTIC` and `F09`, respectively. In general, `ARCTIC` has weaker bulk albedo feedback compared to the 1° runs. A weaker bulk albedo feedback means less shortwave radiation is absorbed given the same amount of near-surface temperature increase. The spatial patterns of the bulk albedo feedback difference agree well with those of the net shortwave radiation difference (Fig.11c,d), indicating a limited role of near-surface temperature increase on causing this pattern. Unlike the bulk albedo feedback that peaks in the lower elevations, the differences are larger over the higher ablation zones. We also examine the albedo feedback (Eq.1) using annual paired detrended anomalies of net shortwave radiation and near-surface temperature over the three 20-year periods. By definition, the albedo feedback reveals an interplay of physical mechanisms, but it is more sensitive to interannual variabilities (e.g., of snowfall), which may make it harder to interpret. The albedo feedback differences show a similar but more variable spatial pattern compared to those of the bulk albedo feedback during year 231-250 and year 331-350 (Fig.S3e-f,h-i) when the albedo feedback is strong (Fig.S3b-c). The difference between bulk albedo feedback and albedo feedback also stresses the importance of melt preconditioning effect on following melt seasons.

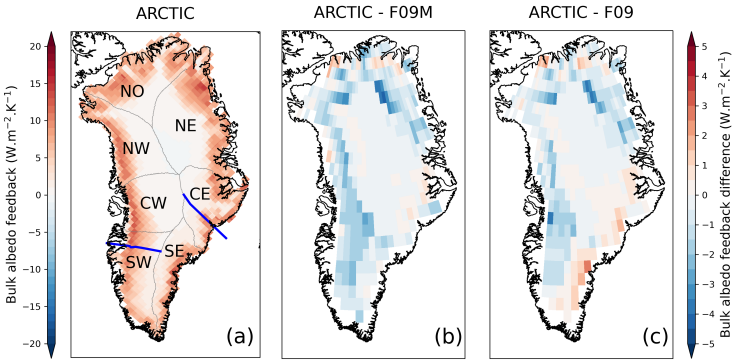


**Figure 12.** Maps of the bulk albedo feedback (W m$^{-2}$ K$^{-1}$) defined by $\Delta SW_{net}/\Delta T_{air}$ of `ARCTIC` (a), and the difference between `ARCTIC` and `F09M` (b), `ARCTIC` and `F09` (c). Time changes from the end of pre-industrial period to the end of the simulation. Gray lines in (a) separate the seven drainage basins defined by Rignot and Mouginot (2012), and blue lines show the location of the two transects plotted in Figure 15.

The difference in albedo feedback between `ARCTIC` and the 1° runs can be largely explained by the different representations of surface topography in different resolution. Figure 13 shows the surface elevation-cumulative area relationships in the three simulations for the whole ice sheet and the individual basins defined by Rignot and Mouginot (2012). A steeper slope in the elevation-cumulative area relationship indicates a larger area increase per meter of elevation rise, thus representing a flatter topography. Ryan et al. (2019) demonstrates the dominant role of Greenland's seasonally fluctuating snowline for reducing ice sheet albedo compared to bare ice albedo reduction caused by melt processes. Here, instead of the end-of-summer snowline elevation, we use the ELA to avoid the possible difficulties of snowline classification. Though different due to processes like superimposed ice formation (Cogley et al., 2011), a significant correlation is found between the ELA and the end-of-summer snowline elevation (Fausto & the PROMICE team*, 2018). For the whole ice sheet, the average ELA rises from around 600 m to 2,500 m over the 350 years. Within this range, `ARCTIC` has a less steep slope of the elevation-cumulative area relationship than the 1° runs (Fig.13a), indicating a smaller area increase with the

same amount of elevation rise. The slope difference between `ARCTIC` and the 1° runs becomes even larger at the end of the simulation compared to the start. Figure 14b shows the relationships between annual mean ELA and ablation area of the three simulations. The match between the simulated ELA-ablation area relationship and the elevation-cumulative area relationship demonstrates the role of topography on regulating the speed of ablation zone expansion. With the same amount of ELA increase, the ablation area increment in `ARCTIC` is smaller due to its steeper topography, which results in a slower ablation zone expansion (Fig.14a) and thus smaller albedo feedback of `ARCTIC` (Fig.12b,c). To further verify the result, the annual mean ablation area and ELA are also computed based on the `ARCTIC` outputs but remapped to the f09 grid (`ARCTIC2f09`) using the Earth System Modeling Framework (ESMF) first-order conservative remapping algorithm (ESMF Joint Specification Team, 2021). A similar slower ablation area expansion and smaller slope of the ELA-ablation area relationship is found for `ARCTIC2f09` (purple line and dots in Fig.14) compared to the 1° runs, which attests our theory.

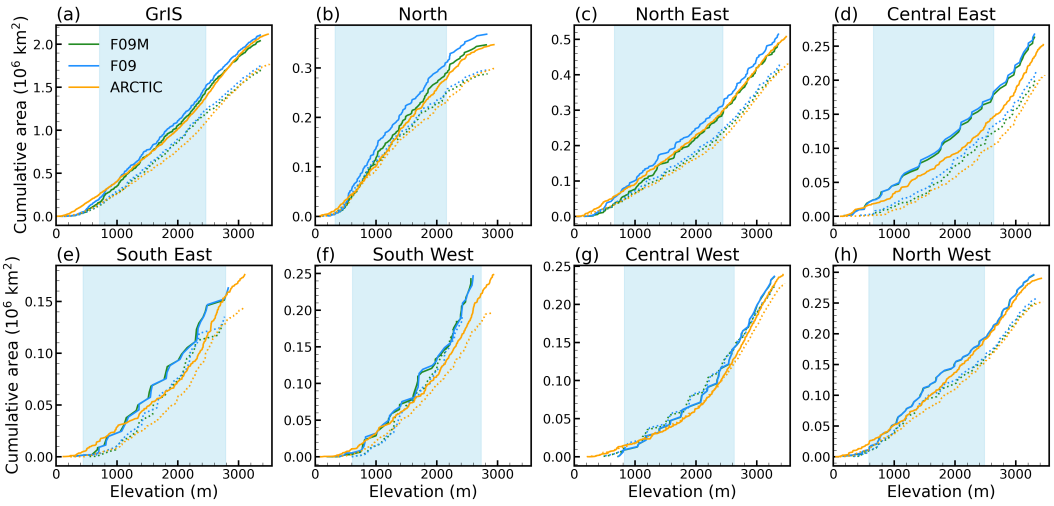


**Figure 13.** Hypsometric surface elevation-area relationships for the whole GrIS (a) and for different basins defined by Rignot and Mouginot (2012) (b-h). For the colored lines, the solid lines represent year 0, and the dotted lines represent year 350. The blue shaded elevation range indicates the annual GrIS- or basin-mean ELA variability in `ARCTIC` during the 350 years.

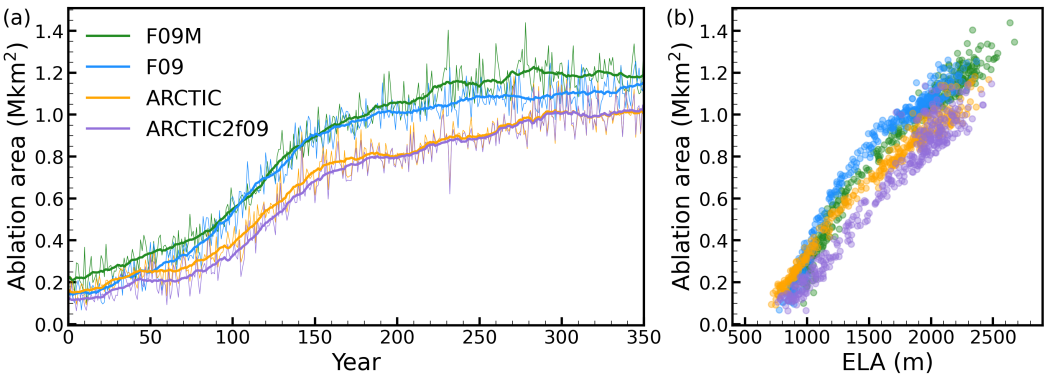


**Figure 14.** Evolution of the annual mean ablation area (Mkm$^2$) (a) and the relationship between ablation area and mean equilibrium line altitude over the Greenland Ice Sheet (b).

Aside from topography, other factors can also affect albedo feedback. Along the southeast coast, the larger precipitation in `F09` (Fig.9b) potentially slows down the albedo reduction more effectively, leading to its smaller bulk albedo feedback there compared to `ARCTIC` (Fig.12c). The impact of clouds on net shortwave radiation also cannot be eliminated from the bulk albedo feedback calculation. However, since the cloud pattern differences that cause more downward shortwave radiation in `ARCTIC` (Fig.10e,f) would play en opposite role, it is not considered as a contributor to the major albedo feedback differences.

Due to the regional dependence of ELA and surface topography, we also check the elevation-cumulative area relationship within separate GrIS drainage basins. The slope difference between `ARCTIC` and the 1° runs is largest within the steepest Central East and South East Basins (Fig.13d,e), but due to the narrow ablation zones and large precipitation in these basins, it does not result in large difference of the albedo feedback. For all the other basins where the albedo feedback is smaller in `ARCTIC` such as the South West, we also find that it has less steep slopes of the elevation-cumulative area relationship compared to the 1° runs (Fig.13f). This consists with our hypothesis that the topography represented in different resolution grids causes the albedo feedback differences.

The different representations of surface topography originate from the grid resolution differences and also the related numerical modeling requirements. Figure 15 shows the representation of the ice sheet surface along two transects (positions shown in Figure 12a) for the three simulations at different times. One is the east-west "K-transect" in southwest Greenland and the other is a transect extending from the central dome down to the Kangerlussuaq glacier on the southeast coast. Compared to `ARCTIC`, the coarser 1° grids have fewer grid cells along the transects, which may result in flatter surfaces locally. Moreover, the smoothing and flattening of the raw topography, necessary to prevent the model from exciting grid-scale numerical modes (Herrington et al., 2022), causes the lower-elevation ablation zones to extend beyond the true ice sheet margin more in the 1° runs. It results in flatter slopes along the transects in `F09M` and `F09`, which favor faster ablation zone expansion. For the more gently sloping K-transect (Fig.15a) with a relatively wide ablation zone (can climbs up the whole transect), this impact of surface slope is more significant as reflected in the bulk albedo feedback (Fig.12b,c). However, for the steeper southeast transect (Fig.15b) where the ablation zone below ∼2600 m is relatively narrow, the impact is limited.

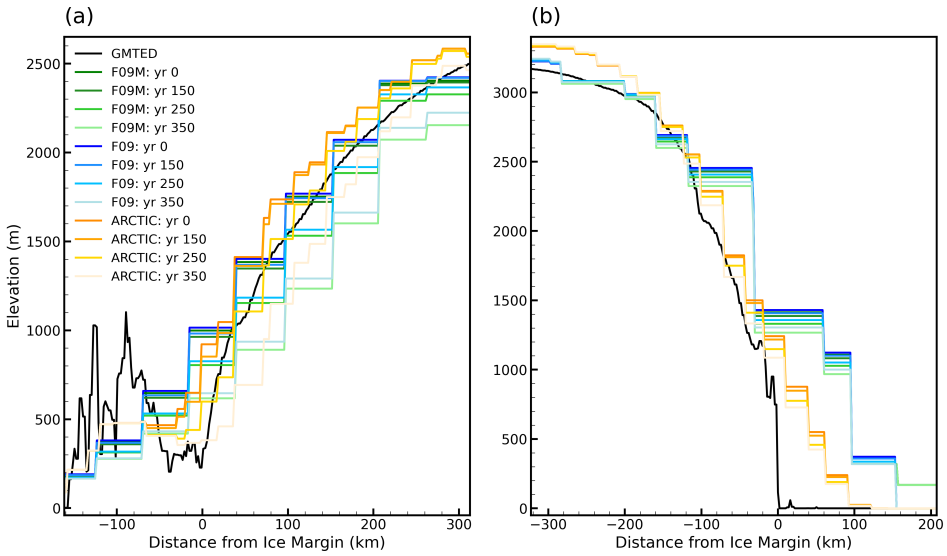


**Figure 15.** Model surface elevation (m) along the (a) K-transect, and (b) a transect spanning the central dome down to the Kangerlussuaq glacier in southeast Greenland, for `F09M`, `F09`, and `ARCTIC` at different times. The GMTED reference surface is a 1 km surface elevation data set Danielson and Gesch (2011) used for generating the CAM topographic boundary conditions.

## 4 Summary and Discussion

In this study, we applied an Arctic-refined variable-resolution grid to a coupled Earth system/ice sheet model, CESM2.2-CISM2.1, to investigate future, multicentury, climate and GrIS evolution. The variable-resolution grid has a horizontal resolution of 1/4° over the broader Arctic region and 1° elsewhere. The simulation was run under a multicentury idealized 4×$CO_2$ scenario and is compared with two other reference simulations under the same forcing scenario but using a lower resolution grid (1° lat-lon grid) to explore the impact of enhanced horizontal resolution.

Though with different magnitudes and timing, the response of the GrIS to the warming climate in the variable-resolution run is similar to what was found in Muntjewerf, Sellevold, et al. (2020). In the variable-resolution run, the global annual average near-surface temperature rises approximately linearly at a speed of 0.33 K per decade during 1% $yr^{-1}$ $CO_2$ increment. Polar amplification is 1.8, while GrIS amplification is much smaller (1.1). After $CO_2$ stabilization, the speed of global annual average near-surface temperature rise decreases more than 40 percents compared to the previous stage (0.19 K per decade). An acceleration of the GrIS mass loss is found at around year 110 (2.4 Gt $yr^{-2}$ before year 110 to 13.0 Gt $yr^{-2}$ during year 111-150), which is driven by faster SMB decrease. At this time, the expansion of the ablation area is large enough to trigger a large melt/albedo feedback, which reinforces the absorption of shortwave radiation and accelerates the melt. The increased sensible and latent heat fluxes also contribute to this process due to expanded and strengthened near-surface temperature inversion. By the end of the simulation, the ablation zone covers 57% of the ice sheet surface. The cumulative contribution from the GrIS to global mean sea level rise is 53 mm by year 150 and 831 mm by year 350, which is about 40% and 20% smaller compared to the 1° runs. The sea level rise contribution from our variable-resolution run by $CO_2$ stabilization is also small compared to other CESM simulations under the CMIP RCP8.5 and SSP5-8.5 scenarios by year 2100 (109 mm in Muntjewerf, Petrini, et al. (2020) and 76 mm in Lipscomb et al. (2013)), when the $CO_2$ concentration is close to 4×$CO_2$. If com-

pared to projections using GrIS models forced by outputs from CMIP5 GCMs (90±50 mm during 2015-2100; Goelzer et al., 2020), our estimation approaches the lower bound.

Compared to the 1° runs, the variable-resolution run has relatively slower MB and SMB decrease. This mainly originates from the smaller surface melt during summer in the variable-resolution run. The SMB difference between the simulations can be smaller than their difference in melt due to compensating terms, which stresses the importance of correctly modeling individual SMB components for making reliable projections of GrIS mass loss. The excessive melt in the 1° runs is concentrated in the western and northern transitional zones towards the margins, produced by the combined effect of greater net longwave and net shortwave radiation, with the latter playing a primary role. The larger net longwave radiation over the ice sheet peripheries in the 1° runs results from their larger and thicker cloud cover over these regions. The net shortwave radiation differences are a product of the stronger albedo feedback over the western and northern basins in the 1° runs. In coarser grids, stronger smoothing and flattening of topography due to grid resolution and necessity to prevent model from exciting grid-scale numerical modes leads to faster ablation zone expansion, thus stronger albedo feedback. Therefore, future sea level projections based on models with a coarse resolution may be biased high due to their inability of adequately resolving the Greenland topography.

Comparisons between these simulations are complicated by differences in grid resolution, physics time step and dynamical core (dycore). Similar to the effect of increasing resolution, reducing physics time step can also increase resolved vertical velocities and thus condensational heating. By comparing two AMIP style CESM2.2 simulations using the same quasi-uniform 1° SE grid but different time steps, Herrington et al. (2022) showed that the simulation with a reduced time step has a warmer troposphere over nearly all latitudes. Then by comparing two simulations using the same time step but different grids - the `Arctic` grid and the quasi-uniform 1° grid, Herrington et al. (2022) showed that the warmer temperature caused by enhanced resolution is confined to the refined Arctic region with a larger magnitude. Therefore, the differences of the simulated climate within the refined Arctic region in this study is more likely a result of changing the horizontal resolution though the impact from changing the physics time step cannot be eliminated. Since the SE dycore is less diffusive than the FV dycore, the resolved vertical velocities are larger in the SE dycore, which can also warm up the atmosphere. It is impossible to fully disentangle the impacts of changing resolution and dynamical core in the current simulations since these factors change simultaneously.

Another uncertainty in this study is the initial condition. The pre-industrial simulations of `ARCTIC` was branched off from an initial condition similar to the initial condition of the `F09M` 1% $CO_2$ simulation. The aim of this is to achieve a near equilibrium state of the GrIS after changing the grid. As a more direct comparison, `F09` went through a similar spin-up process as `ARCTIC`. The resulted initial ice sheet conditions before the start of the idealized warming period are different among the three simulations: `F09` has a larger initial ice volume than `ARCTIC`, while `F09M` has a smaller initial ice volume than `ARCTIC` (Fig.8d). We found that `ARCTIC` has slower SMB decrease and lower melt compared to the 1° runs in multicentury scale, no matter whether their initial ice volume is larger or smaller. Also, `ARCTIC` has a cooler pre-industrial climate than `F09M` and `F09`. The impact of this cooler climate is kept through the whole idealized warming simulation, which is reflected in Figure 6g-l. Moreover, we note that all the three simulations have small positive drifts of GrIS MB before the start of the warming scenario (Table 1). The cooler initial climate in `ARCTIC` results in a longer adjusting time for the GrIS to shift to mass loss, which degrades the specific projections of GrIS sea level rise contribution. However, our result suggests that the near-surface temperature is not the main driver for the different responses of the GrIS among the simulations. Considering all these, we can conclude that our finding is robust.

One limitation of the current model configuration lies in the ice-ocean interface. The direct impact of oceanic thermal forcing on ocean-terminating ice fronts is not included, and the floating criterion used in the calving parameterization is highly idealized. The limited understanding and implementation of processes such as calving and submarine melting in ice sheet models has been identified as a major source of uncertainties for future projections of the GrIS (Goelzer et al., 2020). Oceanic forcing can enhance solid ice discharge (Holland et al., 2008; Wood et al., 2018). Using another coupled Earth system/ice sheet model, EC-Earth-PISM, under the same 1% $yr^{-1}$ $CO_2$ warming scenario, Madsen et al. (2022) showed that even by embedding a constant oceanic thermal forcing and a simple geometric calving criterion, the ice discharge decrease is much smaller after 350 years. Most modeling studies that include oceanic forcing estimate a second order future sea level rise contribution from ice dynamics compared to SMB for the entire ice sheet (Price et al., 2011; Fürst et al., 2015; Aschwanden et al., 2019), but with improved bathymetry and bed topography mapping, Choi et al. (2021) showed that ice dynamics could contribute comparably as SMB or more to GrIS mass loss over this century. These studies illustrate the importance of properly including ice-ocean interactions for future GrIS projections at century to multicentury scale. Currently, the functionality of ice sheet-ocean interaction is under study in CESM and will be included in the future versions. The `Arctic` grid or grids with even higher-resolution refinement will also be helpful by providing a better resolved atmospheric forcing for modeling the ice dynamics in narrow fjords.

In the aggregate, our study demonstrates the value of employing variable-resolution grids for coupled climate-GrIS modeling, providing valuable insights into ice sheet-climate interactions. It underscores the critical role of grid resolution in modeling the evolution of the GrIS on multicentury time scales, particularly in capturing topography-related processes and feedbacks, and thus advances the projection of the GrIS' future sea level rise contribution.

**Acknowledgments**

AH and AG contributions to this material are supported by the National Center for Atmospheric Research (NCAR), a major facility sponsored by the NSF under Cooperative Agreement no. 1852977. Computing and data storage resources, including the Cheyenne supercomputer (Computational and Information Systems Laboratory, 2017), were provided by the Computational and Information Systems Laboratory (CISL) at NCAR, as part of the System for Integrated Modeling of the Atmosphere (SIMA) project. ZY, ACS, JT and RT are supported by the NSF (grant no. OPP 1952199) and HDR iHARP institute (grant no. 2118285).

## Open Research

The data presented in this manuscript are stored in https://doi.org/10.5281/zenodo.10685261, and the code for generating the plots are available at https://github.com/IceZYin/2022-VR-dynamic-GrIS.git.

## References

Aschwanden, A., Fahnestock, M. A., & Truffer, M. (2016). Complex greenland outlet glacier flow captured. *Nature communications*, *7*(1), 10524.

Aschwanden, A., Fahnestock, M. A., Truffer, M., Brinkerhoff, D. J., Hock, R., Khroulev, C., ... Khan, S. A. (2019). Contribution of the greenland ice sheet to sea level over the next millennium. *Science Advances*, *5*(6), eaav9396. Retrieved from https://www.science.org/doi/abs/10.1126/sciadv.aav9396 doi: 10.1126/sciadv.aav9396

Bambach, N. E., Rhoades, A. M., Hatchett, B. J., Jones, A. D., Ullrich, P. A., & Zarzycki, C. M. (2022). Projecting climate change in south america using variable-resolution community earth system model: An application to chile. *International Journal of Climatology*, *42*(4), 2514-2542. doi: https://doi.org/10.1002/joc.7379

Box, J. E., Fettweis, X., Stroeve, J. C., Tedesco, M., Hall, D. K., & Steffen, K. (2012, August). Greenland ice sheet albedo feedback: thermodynamics and atmospheric drivers. *The Cryosphere*, *6*(4), 821–839. Retrieved 2023-07-14, from https://tc.copernicus.org/articles/6/821/2012/ doi: 10.5194/tc-6-821-2012

Choi, Y., Morlighem, M., Rignot, E., & Wood, M. (2021). Ice dynamics will remain a primary driver of greenland ice sheet mass loss over the next century. *Communications Earth & Environment*, *2*(1), 26.

Cogley, J., Hock, R., Rasmussen, L., Arendt, A., Bauder, A., Braithwaite, R., ... Zemp, M. (2011, 01). Glossary of glacier mass balance and related terms. doi: 10.5167/uzh-53475

Computational and Information Systems Laboratory. (2017). *Cheyenne: HPE/SGI ICE XA System (Climate Simulation Laboratory), Boulder, CO: National Center for Atmospheric Research.* doi: 10.5065/D6RX99HX

Danabasoglu, G., Lamarque, J.-F., Bacmeister, J., Bailey, D. A., DuVivier, A. K., Edwards, J., ... Strand, W. G. (2020). The community earth system model version 2 (cesm2). *Journal of Advances in Modeling Earth Systems*, *12*(2), e2019MS001916. doi: https://doi.org/10.1029/2019MS001916

Danielson, J. J., & Gesch, D. B. (2011). Global multi-resolution terrain elevation data 2010 (gmted2010).

Datta, R. T., Herrington, A., Lenaerts, J. T. M., Schneider, D. P., Trusel, L., Yin, Z., & Dunmire, D. (2023). Evaluating the impact of enhanced horizontal resolution over the antarctic domain using a variable-resolution earth system model. *The Cryosphere*, *17*(9), 3847–3866. Retrieved from https://tc.copernicus.org/articles/17/3847/2023/ doi: 10.5194/tc-17-3847-2023

Enderlin, E. M., Howat, I. M., Jeong, S., Noh, M.-J., van Angelen, J. H., & van den Broeke, M. R. (2014). An improved mass budget for the greenland ice sheet. *Geophysical Research Letters*, *41*(3), 866-872. doi: https://doi.org/10.1002/2013GL059010

ESMF Joint Specification Team. (2021). *ESMF user guide* (Tech. Rep.).

Eyring, V., Bony, S., Meehl, G. A., Senior, C. A., Stevens, B., Stouffer, R. J., & Taylor, K. E. (2016). Overview of the coupled model intercomparison project phase 6 (cmip6) experimental design and organization. *Geoscientific Model Development*, *9*(5), 1937–1958. Retrieved from https://gmd.copernicus.org/articles/9/1937/2016/ doi: 10.5194/gmd-9-1937-2016

Fang, Z.-f. (2004). Statistical relationship between the northern hemisphere sea ice and atmospheric circulation during wintertime. In *Observation, theory and modeling of atmospheric variability. world scientific series on meteorology of east asia* (p. 131-141). Singapore: World Scientific Publishing Company. doi: 10.1142/9789812791139_0006

Fausto, R. S., & the PROMICE team*. (2018, Aug.). The greenland ice sheet–snowline elevations at the end of the melt seasons from 2000 to 2017. *GEUS Bulletin*, *41*, 71–74. Retrieved from https://geusbulletin.org/index.php/geusb/article/view/4346 doi: 10.34194/geusb.v41.4346

Fürst, J. J., Goelzer, H., & Huybrechts, P. (2015). Ice-dynamic projections of the greenland ice sheet in response to atmospheric and oceanic warming. *The Cryosphere*, *9*(3), 1039–1062. Retrieved from https://tc.copernicus.org/articles/9/1039/2015/ doi: 10.5194/tc-9-1039-2015

Fyke, J., Sergienko, O., Löfverström, M., Price, S., & Lenaerts, J. T. (2018). An overview of interactions and feedbacks between ice sheets and the earth system. *Reviews of Geophysics*, *56*(2), 361–408.

Gates, W. L. (1992). An ams continuing series: Global change–amip: The atmospheric model intercomparison project. *Bulletin of the American Meteorological Society*, *73*(12), 1962 - 1970. Retrieved from https://journals.ametsoc.org/view/journals/bams/73/12/1520-0477_1992_073_1962_atamip_2_0_co_2.xml doi: https://doi.org/10.1175/1520-0477(1992)073<1962:ATAMIP>2.0.CO;2

Gettelman, A., Callaghan, P., Larson, V. E., Zarzycki, C. M., Bacmeister, J. T., Lauritzen, P. H., ... Neale, R. B. (2018). Regional climate simulations with the community earth system model. *Journal of Advances in Modeling Earth Systems*, *10*(6), 1245-1265. doi: https://doi.org/10.1002/2017MS001227

Gettelman, A., Hannay, C., Bacmeister, J. T., Neale, R. B., Pendergrass, A. G., Danabasoglu, G., ... Mills, M. J. (2019). High climate sensitivity in the community earth system model version 2 (cesm2). *Geophysical Research Letters*, *46*(14), 8329-8337. doi: https://doi.org/10.1029/2019GL083978

Goelzer, H., Nowicki, S., Payne, A., Larour, E., Seroussi, H., Lipscomb, W. H., ... van den Broeke, M. (2020). The future sea-level contribution of the greenland ice sheet: a multi-model ensemble study of ismip6. *The Cryosphere*, *14*(9), 3071–3096. Retrieved from https://tc.copernicus.org/articles/14/3071/2020/ doi: 10.5194/tc-14-3071-2020

Goldberg, D. N. (2011). A variationally derived, depth-integrated approximation to a higher-order glaciological flow model. *Journal of Glaciology*, *57*(201), 157–170.

Guo, Z., Wang, M., Qian, Y., Larson, V. E., Ghan, S., Ovchinnikov, M., ... Zhou, T. (2015). Parametric behaviors of clubb in simulations of low clouds in the community atmosphere model (cam). *Journal of Advances in Modeling Earth Systems*, *7*(3), 1005-1025. Retrieved from https://agupubs.onlinelibrary.wiley.com/doi/abs/10.1002/2014MS000405 doi: https://doi.org/10.1002/2014MS000405

Haarsma, R. J., Roberts, M. J., Vidale, P. L., Senior, C. A., Bellucci, A., Bao, Q., ... von Storch, J.-S. (2016). High resolution model intercomparison project (highresmip v1.0) for cmip6. *Geoscientific Model Development*, *9*(11), 4185–4208. doi: 10.5194/gmd-9-4185-2016

Hanna, E., Cappelen, J., Fettweis, X., Mernild, S. H., Mote, T. L., Mottram, R., ... Hall, R. J. (2021). Greenland surface air temperature changes from 1981 to 2019 and implications for ice-sheet melt and mass-balance change. *International Journal of Climatology*, *41*(S1), E1336-E1352. doi: https://doi.org/10.1002/joc.6771

Hanna, E., Fettweis, X., & Hall, R. J. (2018, October). Brief communication: Recent changes in summer Greenland blocking captured by none of the CMIP5 models. *The Cryosphere*, *12*(10), 3287–3292. doi: 10.5194/tc-12-3287-2018

Hanna, E., Fettweis, X., Mernild, S. H., Cappelen, J., Ribergaard, M. H., Shuman, C. A., ... Mote, T. L. (2014, March). Atmospheric and oceanic climate forcing of the exceptional Greenland ice sheet surface melt in summer 2012: CLIMATE FORCING OF 2012 GREENLAND ICE MELT. *International Journal of Climatology*, *34*(4), 1022–1037. Retrieved 2023-08-28, from https://onlinelibrary.wiley.com/doi/10.1002/joc.3743 doi: 10.1002/joc.3743

Harris, L. M., Lin, S.-J., & Tu, C. (2016). High-resolution climate simulations using gfdl hiram with a stretched global grid. *Journal of Climate*, *29*(11), 4293 - 4314. Retrieved from https://journals.ametsoc.org/view/journals/clim/29/11/jcli-d-15-0389.1.xml doi: https://doi.org/10.1175/JCLI-D-15-0389.1

Herrington, A. R., Lauritzen, P. H., Lofverstrom, M., Lipscomb, W. H., Gettelman, A., & Taylor, M. A. (2022). Impact of grids and dynamical cores in cesm2.2 on the surface mass balance of the greenland ice sheet. *Journal of Advances in Modeling Earth Systems*, *14*(11), e2022MS003192. doi: https://doi.org/10.1029/2022MS003192

Herrington, A. R., & Reed, K. A. (2020). On resolution sensitivity in the community atmosphere model. *Quarterly Journal of the Royal Meteorological Society*, *146*(733), 3789-3807. doi: https://doi.org/10.1002/qj.3873

Holland, D. M., Thomas, R. H., De Young, B., Ribergaard, M. H., & Lyberth, B. (2008). Acceleration of jakobshavn isbræ triggered by warm subsurface ocean waters. *Nature geoscience*, *1*(10), 659–664.

Huang, X., Rhoades, A. M., Ullrich, P. A., & Zarzycki, C. M. (2016). An evaluation of the variable-resolution cesm for modeling california's climate. *Journal of Advances in Modeling Earth Systems*, *8*(1), 345–369.

Huang, X., & Ullrich, P. A. (2017). The changing character of twenty-first-century precipitation over the western united states in the variable-resolution cesm. *Journal of Climate*, *30*(18), 7555 - 7575. doi: https://doi.org/10.1175/JCLI-D-16-0673.1

Hunke, E., Lipscomb, W., Turner, A., Jeffery, N., & Elliott, S. (2015). *Cice: The los alamos sea ice model documentation and software user's manual, version 5.1. tech doc* (Tech. Rep.). T-3 Fluid Dynamics Group, Los Alamos National Laboratory, Tech. Rep. LA-CC-06-012.

Lauritzen, P. H., Bacmeister, J. T., Callaghan, P. F., & Taylor, M. A. (2015). Ncar_topo (v1.0): Ncar global model topography generation software for unstructured grids. *Geoscientific Model Development*, *8*(12), 3975–3986. Retrieved from `https://gmd.copernicus.org/articles/8/3975/2015/` doi: 10.5194/gmd-8-3975-2015

Lauritzen, P. H., Nair, R. D., Herrington, A. R., Callaghan, P., Goldhaber, S., Dennis, J. M., ... Tribbia, J. J. (2018). Ncar release of cam-se in cesm2.0: A reformulation of the spectral element dynamical core in dry-mass vertical coordinates with comprehensive treatment of condensates and energy. *Journal of Advances in Modeling Earth Systems*, *10*(7), 1537-1570. doi: https://doi.org/10.1029/2017MS001257

Lawrence, D. M., Fisher, R. A., Koven, C. D., Oleson, K. W., Swenson, S. C., Bonan, G., ... Zeng, X. (2019). The community land model version 5: Description of new features, benchmarking, and impact of forcing uncertainty. *Journal of Advances in Modeling Earth Systems*, *11*(12), 4245-4287.

Li, H., Wigmosta, M. S., Wu, H., Huang, M., Ke, Y., Coleman, A. M., & Leung, L. R. (2013). A physically based runoff routing model for land surface and earth system models. *Journal of Hydrometeorology*, *14*(3), 808 - 828. doi: https://doi.org/10.1175/JHM-D-12-015.1

Lin, S.-J. (2004). A "vertically lagrangian" finite-volume dynamical core for global models. *Monthly Weather Review*, *132*(10), 2293 - 2307. Retrieved from `https://journals.ametsoc.org/view/journals/mwre/132/10/1520-0493_2004_132_2293_avlfdc_2.0.co_2.xml` doi: https://doi.org/10.1175/1520-0493(2004)132<2293:AVLFDC>2.0.CO;2

Lipscomb, W. H., Fyke, J. G., Vizcaíno, M., Sacks, W. J., Wolfe, J., Vertenstein, M., ... Lawrence, D. M. (2013). Implementation and initial evaluation of the glimmer community ice sheet model in the community earth system model. *Journal of Climate*, *26*(19), 7352 - 7371. Retrieved from `https://journals.ametsoc.org/view/journals/clim/26/19/jcli-d-12-00557.1.xml` doi: https://doi.org/10.1175/JCLI-D-12-00557.1

Lipscomb, W. H., Price, S. F., Hoffman, M. J., Leguy, G. R., Bennett, A. R., Bradley, S. L., ... Worley, P. H. (2019). Description and evaluation of the community ice sheet model (cism) v2.1. *Geoscientific Model Development*,

*12*(1), 387–424. Retrieved from https://gmd.copernicus.org/articles/12/387/2019/ doi: 10.5194/gmd-12-387-2019

Lofverstrom, M., Fyke, J. G., Thayer-Calder, K., Muntjewerf, L., Vizcaino, M., Sacks, W. J., ... Bradley, S. L. (2020). An efficient ice sheet/earth system model spin-up procedure for cesm2-cism2: Description, evaluation, and broader applicability. *Journal of Advances in Modeling Earth Systems*, *12*(8), e2019MS001984. doi: https://doi.org/10.1029/2019MS001984

Madsen, M., Yang, S., Aðalgeirsdóttir, G., Svendsen, S., Rodehacke, C., & Ringgaard, I. (2022). The role of an interactive greenland ice sheet in the coupled climate-ice sheet model ec-earth-pism. *Climate Dynamics*, *59*(3-4), 1189–1211.

Mouginot, J., Rignot, E., Bjørk, A. A., Van den Broeke, M., Millan, R., Morlighem, M., ... Wood, M. (2019). Forty-six years of greenland ice sheet mass balance from 1972 to 2018. *Proceedings of the national academy of sciences*, *116*(19), 9239–9244.

Muntjewerf, L., Petrini, M., Vizcaino, M., Ernani Da Silva, C., Sellevold, R., Scherrenberg, M. D. W., ... Lofverstrom, M. (2020, May). Greenland Ice Sheet Contribution to 21st Century Sea Level Rise as Simulated by the Coupled CESM2.1-CISM2.1. *Geophysical Research Letters*, *47*(9), e2019GL086836. Retrieved 2023-09-26, from https://agupubs.onlinelibrary.wiley.com/doi/10.1029/2019GL086836 doi: 10.1029/2019GL086836

Muntjewerf, L., Sacks, W. J., Lofverstrom, M., Fyke, J., Lipscomb, W. H., Ernani da Silva, C., ... Sellevold, R. (2021). Description and demonstration of the coupled community earth system model v2 – community ice sheet model v2 (cesm2-cism2). *Journal of Advances in Modeling Earth Systems*, *13*(6), e2020MS002356. Retrieved from https://agupubs.onlinelibrary.wiley.com/doi/abs/10.1029/2020MS002356 doi: https://doi.org/10.1029/2020MS002356

Muntjewerf, L., Sellevold, R., Vizcaino, M., Ernani da Silva, C., Petrini, M., Thayer-Calder, K., ... Sacks, W. J. (2020). Accelerated greenland ice sheet mass loss under high greenhouse gas forcing as simulated by the coupled cesm2.1-cism2.1. *Journal of Advances in Modeling Earth Systems*, *12*(10), e2019MS002031. doi: https://doi.org/10.1029/2019MS002031

Nowicki, S. M. J., Payne, A., Larour, E., Seroussi, H., Goelzer, H., Lipscomb, W., ... Shepherd, A. (2016). Ice sheet model intercomparison project (ismip6) contribution to cmip6. *Geoscientific Model Development*, *9*(12), 4521–4545. Retrieved from https://gmd.copernicus.org/articles/9/4521/2016/ doi: 10.5194/gmd-9-4521-2016

Otosaka, I. N., Shepherd, A., Ivins, E. R., Schlegel, N.-J., Amory, C., van den Broeke, M. R., ... Wouters, B. (2023). Mass balance of the greenland and antarctic ice sheets from 1992 to 2020. *Earth System Science Data*, *15*(4), 1597–1616. doi: 10.5194/essd-15-1597-2023

Pollard, D., & Groups, P. P. (2000). Comparisons of ice-sheet surface mass budgets from paleoclimate modeling intercomparison project (pmip) simulations. *Global and Planetary Change*, *24*(2), 79–106.

Pope, V., & Stratton, R. (2002). The processes governing horizontal resolution sensitivity in a climate model. *Climate Dynamics*, *19*, 211–236.

Price, S. F., Payne, A. J., Howat, I. M., & Smith, B. E. (2011, May). Committed sea-level rise for the next century from Greenland ice sheet dynamics during the past decade. *Proceedings of the National Academy of Sciences*, *108*(22), 8978–8983. Retrieved 2023-09-19, from https://pnas.org/doi/full/10.1073/pnas.1017313108 doi: 10.1073/pnas.1017313108

Rahimi, S. R., Wu, C., Liu, X., & Brown, H. (2019). Exploring a variable-resolution approach for simulating regional climate over the tibetan plateau using vr-cesm. *Journal of Geophysical Research: Atmospheres*, *124*(8), 4490-4513. doi: https://doi.org/10.1029/2018JD028925

Rhoades, A. M., Huang, X., Ullrich, P. A., & Zarzycki, C. M. (2016). Characterizing sierra nevada snowpack using variable-resolution cesm. *Journal of Applied Meteorology and Climatology*, *55*(1), 173–196.

Rhoades, A. M., Ullrich, P. A., & Zarzycki, C. M. (2018). Projecting 21st century snowpack trends in western usa mountains using variable-resolution cesm. *Climate Dynamics*, *50*(1-2), 261–288.

Rignot, E., & Mouginot, J. (2012). Ice flow in greenland for the international polar year 2008–2009. *Geophysical Research Letters*, *39*(11). Retrieved from `https://agupubs.onlinelibrary.wiley.com/doi/abs/10.1029/2012GL051634` doi: https://doi.org/10.1029/2012GL051634

Roeckner, E., Brokopf, R., Esch, M., Giorgetta, M., Hagemann, S., Kornblueh, L., ... Schulzweida, U. (2006). Sensitivity of simulated climate to horizontal and vertical resolution in the echam5 atmosphere model. *Journal of Climate*, *19*(16), 3771–3791.

Rutt, I. C., Hagdorn, M., Hulton, N. R. J., & Payne, A. J. (2009). The glimmer community ice sheet model. *Journal of Geophysical Research: Earth Surface*, *114*(F2). Retrieved from `https://agupubs.onlinelibrary.wiley.com/doi/abs/10.1029/2008JF001015` doi: https://doi.org/10.1029/2008JF001015

Ryan, J. C., Smith, L. C., van As, D., Cooley, S. W., Cooper, M. G., Pitcher, L. H., & Hubbard, A. (2019). Greenland ice sheet surface melt amplified by snowline migration and bare ice exposure. *Science Advances*, *5*(3), eaav3738. Retrieved from `https://www.science.org/doi/abs/10.1126/sciadv.aav3738` doi: 10.1126/sciadv.aav3738

Sakaguchi, K., Leung, L. R., Zarzycki, C. M., Jang, J., McGinnis, S., Harrop, B. E., ... Mearns, L. (2023). Technical descriptions of the experimental dynamical downscaling simulations over north america by the cam–mpas variable-resolution model. *Geoscientific Model Development*, *16*(10), 3029–3081. Retrieved from `https://gmd.copernicus.org/articles/16/3029/2023/` doi: 10.5194/gmd-16-3029-2023

Schmidt, F. (1977). Variable fine mesh in spectral global models. *BEITR. PHYS. ATMOSPH.*, *50*, 211-217.

Sellevold, R., van Kampenhout, L., Lenaerts, J. T. M., Noël, B., Lipscomb, W. H., & Vizcaino, M. (2019). Surface mass balance downscaling through elevation classes in an earth system model: application to the greenland ice sheet. *The Cryosphere*, *13*(12), 3193–3208. Retrieved from `https://tc.copernicus.org/articles/13/3193/2019/` doi: 10.5194/tc-13-3193-2019

Sellevold, R., & Vizcaíno, M. (2020, September). Global warming threshold and mechanisms for accelerated greenland ice sheet surface mass loss. *Journal of Advances in Modeling Earth Systems*, *12*(9). Retrieved 2023-08-26, from `https://onlinelibrary.wiley.com/doi/10.1029/2019MS002029` doi: 10.1029/2019MS002029

Smith, R., Jones, P., Briegleb, B., Bryan, F., Danabasoglu, G., Dennis, J., ... others (2010). The parallel ocean program (pop) reference manual ocean component of the community climate system model (ccsm) and community earth system model (cesm). *LAUR-01853*, *141*, 1–140.

Staniforth, A. N., & Mitchell, H. L. (1978). A variable-resolution finite-element technique for regional forecasting with the primitive equations. *Monthly Weather Review*, *106*(4), 439 - 447. doi: https://doi.org/10.1175/1520-0493(1978)106<0439:AVRFET>2.0.CO;2

Straneo, F., & Heimbach, P. (2013). North atlantic warming and the retreat of greenland's outlet glaciers. *Nature*, *504*(7478), 36–43.

Tang, Q., Golaz, J.-C., Van Roekel, L. P., Taylor, M. A., Lin, W., Hillman, B. R., ... Bader, D. C. (2023). The fully coupled regionally refined model of e3sm version 2: overview of the atmosphere, land, and river results. *Geoscientific Model Development*, *16*(13), 3953–3995. Retrieved

from https://gmd.copernicus.org/articles/16/3953/2023/ doi: 10.5194/gmd-16-3953-2023

Tedesco, M., & Fettweis, X. (2020). Unprecedented atmospheric conditions (1948–2019) drive the 2019 exceptional melting season over the greenland ice sheet. *The Cryosphere*, *14*(4), 1209–1223. Retrieved from https://tc.copernicus.org/articles/14/1209/2020/ doi: 10.5194/tc-14-1209-2020

Trusel, L. D., Das, S. B., Osman, M. B., Evans, M. J., Smith, B. E., Fettweis, X., ... van den Broeke, M. R. (2018). Nonlinear rise in greenland runoff in response to post-industrial arctic warming. *Nature*, *564*(7734), 104–108.

van Kampenhout, L., Lenaerts, J. T. M., Lipscomb, W. H., Lhermitte, S., Noël, B., Vizcaíno, M., ... van den Broeke, M. R. (2020). Present-day greenland ice sheet climate and surface mass balance in cesm2. *Journal of Geophysical Research: Earth Surface*, *125*(2), e2019JF005318. Retrieved from https://agupubs.onlinelibrary.wiley.com/doi/abs/10.1029/2019JF005318 doi: https://doi.org/10.1029/2019JF005318

van Kampenhout, L., Rhoades, A. M., Herrington, A. R., Zarzycki, C. M., Lenaerts, J. T. M., Sacks, W. J., & van den Broeke, M. R. (2019). Regional grid refinement in an earth system model: impacts on the simulated greenland surface mass balance. *The Cryosphere*, *13*(6), 1547–1564. doi: 10.5194/tc-13-1547-2019

Vizcaíno, M., Mikolajewicz, U., Jungclaus, J., & Schurgers, G. (2010). Climate modification by future ice sheet changes and consequences for ice sheet mass balance. *Climate Dynamics*, *34*, 301–324.

Wijngaard, R. R., Herrington, A. R., Lipscomb, W. L., Leguy, G. R., & An, S.-I. (2023). Exploring the ability of the variable-resolution cesm to simulate cryospheric-hydrological variables in high mountain asia. *The Cryosphere Discussions*, *2023*, 1–39. Retrieved from https://tc.copernicus.org/preprints/tc-2022-256/ doi: 10.5194/tc-2022-256

Wood, M., Rignot, E., Fenty, I., Menemenlis, D., Millan, R., Morlighem, M., ... Seroussi, H. (2018). Ocean-induced melt triggers glacier retreat in northwest greenland. *Geophysical Research Letters*, *45*(16), 8334-8342. Retrieved from https://agupubs.onlinelibrary.wiley.com/doi/abs/10.1029/2018GL078024 doi: https://doi.org/10.1029/2018GL078024

Wu, C., Liu, X., Lin, Z., Rhoades, A. M., Ullrich, P. A., Zarzycki, C. M., ... Rahimi-Esfarjani, S. R. (2017). Exploring a variable-resolution approach for simulating regional climate in the rocky mountain region using the vr-cesm. *Journal of Geophysical Research: Atmospheres*, *122*(20), 10,939-10,965. doi: https://doi.org/10.1002/2017JD027008

Zängl, G., Reinert, D., & Prill, F. (2022). Grid refinement in icon v2.6.4. *Geoscientific Model Development*, *15*(18), 7153–7176. Retrieved from https://gmd.copernicus.org/articles/15/7153/2022/ doi: 10.5194/gmd-15-7153-2022

Zarzycki, C. M. (2016). Tropical cyclone intensity errors associated with lack of two-way ocean coupling in high-resolution global simulations. *Journal of Climate*, *29*(23), 8589 - 8610. doi: https://doi.org/10.1175/JCLI-D-16-0273.1

Zarzycki, C. M., & Jablonowski, C. (2014). A multidecadal simulation of atlantic tropical cyclones using a variable-resolution global atmospheric general circulation model. *Journal of Advances in Modeling Earth Systems*, *6*(3), 805-828. doi: https://doi.org/10.1002/2014MS000352

Zarzycki, C. M., Jablonowski, C., & Taylor, M. A. (2014). Using variable-resolution meshes to model tropical cyclones in the community atmosphere model. *Monthly Weather Review*, *142*(3), 1221 - 1239. doi: https://doi.org/10.1175/MWR-D-13-00179.1

Zarzycki, C. M., Jablonowski, C., Thatcher, D. R., & Taylor, M. A. (2015). Effects of localized grid refinement on the general circulation and climatology in the

community atmosphere model. *Journal of Climate*, *28*(7), 2777 - 2803. doi: https://doi.org/10.1175/JCLI-D-14-00599.1

# Improved Understanding of Multicentury Greenland Ice Sheet Response to Strong Warming in the Coupled CESM2-CISM2 with Regional Grid Refinement

**Ziqi Yin[1], Adam R. Herrington[2], Rajashree Tri Datta[1], Aneesh Subramanian[1], Jan T. M. Lenaerts[1], and Andrew Gettelman[3]**

[1]Department of Atmospheric and Oceanic Sciences, University of Colorado Boulder, Boulder, CO, USA
[2]National Center for Atmospheric Research, Boulder, CO, USA
[3]Pacific Northwest National Laboratory, Richland, WA, USA

**Key Points:**

- For the first time, a variable-resolution atmosphere is coupled with the ocean and sea ice components in CESM with a dynamic GrIS
- Slower Greenland surface melt increase is detected in the Arctic-refined simulation compared with simulations using a conventional 1° grid
- The steeper VR GrIS surface topography favors slower ablation zone expansion, leading to weaker albedo feedback and slower melt increase

Corresponding author: Ziqi Yin, Ziqi.Yin@colorado.edu

## Abstract

The simulation of ice sheet-climate interaction such as surface mass balance fluxes are sensitive to model grid resolution. Here we simulate the multicentury evolution of the Greenland Ice Sheet (GrIS) and its interaction with the climate using the Community Earth System Model version 2.2 (CESM2.2) including an interactive GrIS component (the Community Ice Sheet Model v2.1 [CISM2.1]) under an idealized warming scenario (atmospheric $CO_2$ increases by 1% $yr^{-1}$ until quadrupling the pre-industrial level and then is held fixed). A variable-resolution (VR) grid with 1/4° regional refinement over broader Arctic and 1° resolution elsewhere is applied to the atmosphere and land components, and the results are compared to conventional 1° lat-lon grid simulations to investigate the impact of grid refinement. An acceleration of GrIS mass loss is found at around year 110, caused by rapidly increasing surface melt as the ablation area expands with associated albedo feedback and increased turbulent fluxes. Compared to the 1° runs, the VR run features slower melt increase, especially over Western and Northern Greenland, which slope gently towards the peripheries. This difference pattern originates primarily from the weaker albedo feedback in the VR run, complemented by its smaller cloud longwave radiation. The steeper VR Greenland surface topography favors slower ablation zone expansion, thus leading to its weaker albedo feedback. The sea level rise contribution from the GrIS in the VR run is 53 mm by year 150 and 831 mm by year 350, approximately 40% and 20% smaller than the 1° runs, respectively.



## Plain Language Summary

As one of the main contributors to global sea level rise, the Greenland Ice Sheet (GrIS) has been losing mass as an accelerating rate during the recent decades. Better understanding the interactions between the GrIS and the climate can help us make more reliable future projections of GrIS mass loss. To simulate these interactions, a fully coupled model infrastructure is necessary. Additionally, the model resolution needs to be higher enough to resolve the surface topography and processes like orographic precipitation. This study applies a 1/4° Arctic refined grid to an Earth System Model which includes an interactive GrIS model to simulate multicentury GrIS evolution under an idealized warming scenario, and compares the results with simulations using a lower resolution grid. We show that the simulation with the grid refinement has a slower increase in melt, thus contributing less to global sea level rise. This difference mainly results from the slower ablation zone expansion and thus weaker albedo feedback in the Arctic refined grid simulation, with the smaller cloud longwave radiation playing a supporting role.


## 1 Introduction

Recent data reveals an acceleration in the mass loss from the Greenland Ice Sheet (GrIS), averaging 257 Gt $yr^{-1}$ between 2017 and 2020, a sevenfold increase compared to the early 1990s (Otosaka et al., 2023). GrIS mass loss is driven both by atmospheric warming (Hanna et al., 2021), which increases surface melt and meltwater runoff (Trusel et al., 2018), and oceanic warming, which has caused glacier acceleration and enhanced ice discharge (Straneo & Heimbach, 2013). Though the ice discharge increase played a stronger role in GrIS mass loss between 1992 and 2018 (66 ± 8%), during the last two decades, surface mass balance (SMB) decrease has become the dominant contributor due to increased surface melt (Enderlin et al., 2014; Mouginot et al., 2019). The exceptional summer surface melting causes a maximum mass loss of 444 Gt $yr^{-1}$ in 2019 (Tedesco & Fettweis, 2020). The interactions between the ice sheet, the atmosphere, and the ocean can initiate feedback effects, further amplifying or dampening the mass imbalance signals. One important positive feedback is the albedo/melt feedback. As snow or ice melts, the surface with lower albedo, e.g., warmer snow/firn/bare ice/ground, is exposed, lead-

ing to increased absorption of shortwave radiation and thus further promoting melt of the original and nearby regions. Many other feedbacks can enhance or restrain GrIS mass loss, such as geometry/SMB feedbacks (Fyke et al., 2018). So, to better model the evolution of the GrIS, a coupled model that can represent these bidirectional interactions/feedbacks is necessary.

The accuracy of simulated SMB is sensitive to model grid resolution, especially in regions with steep and complex terrains. The mountainous GrIS margins, also where steep topographic gradients are located, are too smooth in conventional 1° to 2° global climate models (GCMs). Such models fail to resolve processes like orographic precipitation and allow too much moisture to penetrate into the ice sheet interior, causing positive precipitation biases (Pollard & Groups, 2000). Research has shown that, with a higher horizontal resolution, the orographic precipitation can be better resolved and thus the positive precipitation biases can be reduced (van Kampenhout et al., 2019; Herrington et al., 2022). In addition, the ablation zone around the GrIS margins where the majority of summer melt occurs can be as narrow as tens of kilometers, which cannot be resolved by 1° to 2° grids. It is therefore important to have a finer resolution for more accurate representation of GrIS SMB processes.

Modeling with a variable-resolution grid has several advantages. Though rapidly developing, widespread use of global-uniform high-resolution climate models (e.g., models participated in the High-Resolution Model Intercomparison Project (HighResMIP; Haarsma et al., 2016)) is still impractical due to current limits in computational resources. Regional climate models (RCMs), usually in one-way nesting mode, offer regional high resolution with a lower computational cost. However, they need boundary conditions from GCMs or reanalysis, thus not allowing two-way interactions across the boundaries. Moreover, the boundary conditions derived from a separate host model can introduce inconsistencies between the host model and the RCM. Variable-resolution modeling overcomes some of these challenges using a unified modeling framework, which can model the two-way interactions between the regional and large scales and is more computationally efficient.

The application of regional grid refinement in GCMs can be dated back to the early use of stretched grids in late 1970s (Schmidt, 1977; Staniforth & Mitchell, 1978) and now it has been developed in many state-of-the-art GCMs (Harris et al., 2016; Zängl et al., 2022; Sakaguchi et al., 2023; Tang et al., 2023). In the Community Earth System Model, version2 (CESM2; Danabasoglu et al., 2020), regional grid refinement is supported by the spectral-element (SE; Lauritzen et al., 2018) dynamical core of the atmospheric component. Studies have proven its consistency in modeling global circulation and climatology (Zarzycki et al., 2015; Gettelman et al., 2018), fidelity in representing tropical and extra-tropical cyclones (Zarzycki & Jablonowski, 2014; Zarzycki et al., 2014; Zarzycki, 2016) and regional climate, especially at regions with mountains or steep terrain (Rhoades et al., 2016; Huang et al., 2016; Huang & Ullrich, 2017; Wu et al., 2017; Rhoades et al., 2018; Rahimi et al., 2019; Bambach et al., 2022; Wijngaard et al., 2023). The variable-resolution CESM2 (VR-CESM2) has also been applied to the polar regions. van Kampenhout et al. (2019) shows that the simulation of GrIS SMB in the accumulation zone is significantly improved by using two regionally refined grids over the GrIS at 1/2° and 1/4°. In addition to improvements where a refined resolution is applied to the GrIS, the simulated clouds and precipitation in the Arctic is also substantially improved with two Arctic-refined meshes, one at 1/4° and another with an additional 1/8° patch of refinement over Greenland (Herrington et al., 2022). For the Antarctic, 1/4° regional refinement over the Antarctic Ice Sheet and the surrounding Southern Ocean indicates both improvements, mainly in temperature and wind fields, and degradations, primarily related to surface melt, over the Antarctic Ice Sheet compared to 1° CESM2 (Datta et al., 2023). The VR-CESM2 in the above-mentioned studies are run in the coupled land-atmosphere

mode following the Atmospheric Model Intercomparison Project protocols (AMIP; Gates, 1992).

This study analyzes the results from a set of simulations using the fully coupled configuration of CESM2 with a dynamic GrIS under an idealized strong warming scenario. A variable-resolution grid, which has 1/4° regional refinement over the broader Arctic region and 1° horizontal resolution elsewhere, is applied to the atmosphere and land components of CESM2. Unlike prior VR-CESM2 studies, we include coupling to a dynamic ocean model, similar to Tang et al. (2023). This work aims to: first, investigate multicentury future GrIS evolution, and second, compare the results of the variable-resolution run with those of global 1° resolution runs, to see where the regional refinement provides added value. Section 2 documents the model, grids, and experiment design information. Section 3 presents the results and the comparison of the simulations. Finally, in Section 4, a discussion and conclusions are provided.

## 2 Methods

### 2.1 Model Description

CESM2 is an Earth System Model (ESM) maintained by the National Center for Atmosphere Research, which consists of atmosphere, ocean, land, sea ice, and land ice components and can be run in configurations with different levels of complexity. The ocean component, Parallel Ocean Program version 2 (POP2; Smith et al., 2010), runs on a nominal 1° displaced-pole grid with 60 vertical levels. Sea ice is represented by the Community Ice CodE for sea ice version 5 (CICE5; Hunke et al., 2015), using the same horizontal grid as POP2. Land processes are simulated by the Community Land Model version 5 (CLM5; Lawrence et al., 2019), using the same horizontal grid as the atmosphere model. CLM5 also embeds the Model for Scale Adaptive River Transport (MOSART; Li et al., 2013) to handle land surface runoff based on topographic gradients.

The GrIS is simulated using the Community Ice Sheet Model, version 2.1 (CISM2.1; Lipscomb et al., 2019), using a 4-km rectangular grid with 11 terrain-following vertical levels. To simulate ice flow, a depth-integrated higher-order approximation (Goldberg, 2011) of the Stokes equations is employed in the velocity solver. The parameterization of basal sliding utilizes a pseudo-plastic sliding law and a simple basal hydrology model, following the approach described by Aschwanden et al. (2016). In this parameterization, the yield stress is determined by the till friction angle and the effective pressure, with the former being influenced by the bedrock elevation through a fixed piecewise linear relationship. The bedrock evolution due to Glacial Isostatic Adjustment (GIA) effect is governed by an Elastic plate Lithosphere plus Relaxing Asthenosphere (ELRA) model (see for example Rutt et al., 2009). This study accounts for calving processes through a flotation criterion, where floating ice is instantaneously discharged to the ocean.

Two versions of CESM2 are used for the simulations in this study: CESM2.1 and CESM2.2. In CESM2.1, the atmosphere is simulated with the Community Atmosphere Model version 6 (CAM6; Gettelman et al., 2019), using the Finite-Volume (FV; Lin, 2004) dynamical core, with 32 vertical hybrid pressure-sigma levels. The CAM6 physical parameterization package is described in detail in Gettelman et al. (2019). CESM2.1 is one of the ESMs to contribute to the Coupled Model Intercomparison Project Phase 6 (CMIP6; Eyring et al., 2016) and the Ice Sheet Model Intercomparison Project for CMIP6 (ISMIP6; Nowicki et al., 2016).

CESM2.2 uses the same CAM physics parameterizations and vertical grid, but contains enhanced functionality for the SE dynamical core, including the capability for running VR grids (Herrington et al., 2022). The CMIP6 CESM2.1 simulations using CAM-FV are not reproducible in CESM2.2, and therefore two versions of the model are required to compare the VR grids to the CMIP6 workhorse configuration.

### 2.2 Surface Mass Balance

The GrIS SMB simulated in CESM2 is the sum of ice accumulation and ice ablation. The SMB processes of the GrIS are aggregated in CLM5, which includes up to 10 vertical snowpack layers with a maximum total depth of 10-m water equivalent. Only snow accumulated over the 10-m threshold contributes to ice accumulation. Ice ablation incorporates surface ice melt as well as sublimation. Part of rain and melt water penetrates into the snow layers and refreezes, as another source of ice, while the rest runs off to the ocean. Melt energy is calculated from the sum of net surface radiation, latent and sensible turbulent heat fluxes, and ground heat fluxes at the atmosphere-snow interface. To account for sub-grid variability, each glaciated grid cell in CLM5 is subdivided into 10 elevation classes (ECs) with fixed elevation ranges (Lipscomb et al., 2013; Sellevold et al., 2019). The area fractions of the ECs are calculated from the higher-resolution CISM topography. For each EC, the surface energy fluxes and SMB are calculated independently by downscaling atmospheric variables. Near-surface temperature and downward longwave radiation are downscaled with fixed lapse rates (6 K $km^{-1}$ and 32 W $m^{-2}$ $km^{-1}$). Relative humidity is assumed uniform vertically. Due to a CAM6 model bias leading to excessive rainfall over the GrIS, precipitation is repartitioned based on near-surface temperature thresholds: precipitation falls as snow when the temperature is below -2°C, as rain when the temperature is above 0°C, and as a linear combination of snow and rain for temperatures between -2°C and 0°C.

Though with biases such as overestimated precipitation, CESM2.1 at 1° with a fixed GrIS geometry simulates a realistic historical Greenland SMB (van Kampenhout et al., 2020). When coupled to CISM2, higher Greenland SMB and interannual variability is simulated, partly due to the different ice sheet topography (Muntjewerf, Petrini, et al., 2020).

### 2.3 Coupling Scheme

In the model framework, the GrIS is interactively coupled to the other Earth system components. CISM2 receives the CLM5 SMB for each EC, and is then downscaled by the coupler using a trilinear remapping scheme (bilinear horizontally and linear vertically), with corrections of accumulation and ablation to conserve global water mass. As the ice sheet evolves, the coupler updates the EC fractional glacier coverage in each CLM5 grid cell based on the CISM2 ice sheet extent at annual frequency. The mean surface elevation in CAM6 is manually updated based on the CISM2 topography every 20 model years, using the CESM topography software (Lauritzen et al., 2015). Surface runoff from CLM5, basal melt and ice discharge from CISM2 constitute the freshwater fluxes inputted into the ocean, which are supplied as salinity anomalies. More detailed description of the coupling scheme can be found in Muntjewerf et al. (2021).

### 2.4 Grids

The variable-resolution grid we use here - the `Arctic` grid (Fig.1a), is a 1° SE grid with 1/4° regional refinement over the broader Arctic region (Herrington et al., 2022). It is generated by using the software package SQuadgen (https://github.com/ClimateGlobalChange/squadgen). The global 1° resolution runs use the latitude-longitude 1° grid, referred to as `f09`, supported by the FV dynamical core. Figure 1b and 1c show a snapshot of the surface topography over the GrIS before the start of the warming scenario for the `f09` grid and the `Arctic` grid, respectively. The `Arctic` grid represents more detailed Greenland topography (e.g., the south dome and ice sheet periphery) with a more accurate ice sheet mask. The surface elevation differences between two grids can range up over 700 m (Fig.1d), which is partly caused by the initial ice sheet volume difference. The physics time step of the `Arctic` simulations is 450 s, which is a 4× reduction relative to the default 1800 s time step used in the 1° grid.

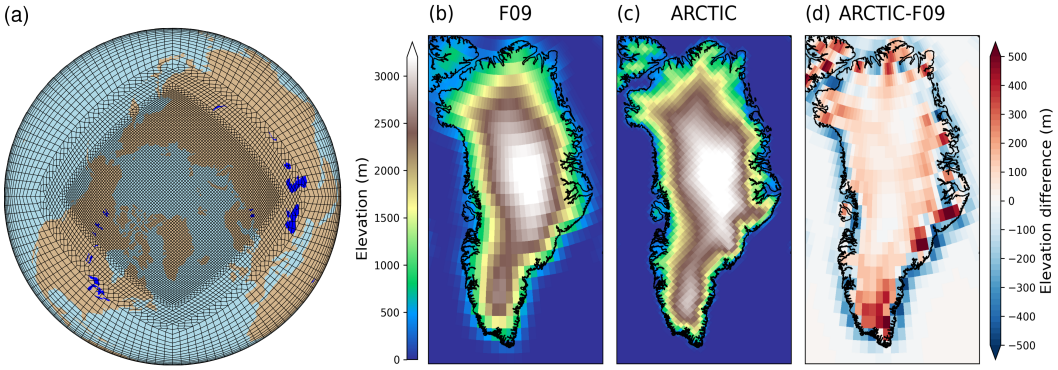


**Figure 1.** (a) The `Arctic` grid (Herrington et al., 2022). Note what is shown is the element grid; the computational grid has 3 × 3 independent grid points per element. Surface topography (m) of the Greenland Ice Sheet represented by (b) the `f09` grid, (c) the `Arctic` grid, and (d) their difference before the start of the warming scenario.

### 2.5 Experiment Design

First, a pre-industrial simulation was branched off from the last leg of the spun-up pre-industrial Earth system/ice sheet state (Lofverstrom et al., 2020). A series of experiments were ran to bring the top of atmosphere radiative forcing into balance using common tuning parameters such `clubb_gamma` (Guo et al., 2015). The tuned pre-industrial control was then run for 180 years until the GrIS achieved near equilibrium state. Then an idealized warming scenario was started, in which the atmospheric $CO_2$ concentration increased by 1% per year until reaching 4× the pre-industrial value after 140 years, followed by a 210-year simulation with the fixed 4× pre-industrial $CO_2$ concentration (Fig.2a). This set of simulations using the `Arctic` grid (hereafter `ARCTIC`) was compared to two sets of simulations under the same forcing but using the f09 grid, in the older CESM2.1 code base. One is from Muntjewerf, Sellevold, et al. (2020) (hereafter `F09M`). In this code base, to reduce the too-high SMB over portions of the GrIS in CESM2 coupled runs, the cold rain (< -2°C) produced by CAM immediately runs off to the ocean instead of being converted to snow by CLM. Also, to facilitate low level convergence and precipitation near the coasts, the sub-grid roughness over Greenland is artificially increased. To limit the differences between models, we ran another set of f09 simulation using CESM2.1 but without these two adjustments (hereafter `F09`).

### 2.6 Analysis

#### *2.6.1 Atmospheric and Oceanic Circulation Metrics*

The Greenland blocking index (GBI) uses the 500-hPa geopotential height ($Z_{500}$) to estimate blocking over the Greenland region (Fang, 2004). Strong and persistent blocking can result in extreme summer melt at the ice sheet surface (Hanna et al., 2014). The revised GBI from Hanna et al. (2018) is used, which is calculated by subtracting the area-averaged $Z_{500}$ over the Arctic region (60°N to 80°N) from the area-averaged $Z_{500}$ over the Greenland region (60°N to 80°N, and 80°W to 20°W). Then the resulting time series is standardized with respect to the last 80 years of the pre-industrial period. Here only the JJA mean GBI is considered.

The North Atlantic Meridional Overturning Circulation (NAMOC) index measures the strength of the North Atlantic Meridional Overturning Circulation, which is predicted to be weaken with the addition of GrIS meltwater to the ocean (Vizcaíno et al., 2010;

Muntjewerf, Sellevold, et al., 2020). The NAMOC index is defined as the maximum of the overturning stream function north of 28°N and below 500-m depth.

#### *2.6.2 Melt/albedo Feedback*

We use the melt/albedo feedback (or albedo feedback) calculations following Box et al. (2012). The albedo feedback ($\alpha_{feedback,a}$) is quantified by regression between 20 annual samples of detrended anomalies of summer (JJA) average net shortwave radiation ($SW_{net}$) and near-surface air temperature ($T_{air}$) in units of W m$^{-2}$ K$^{-1}$, with anomalies indicated by the $'$ character in $\Delta'$:

$$\alpha_{feedback,a} = \Delta' SW_{net} / \Delta' T_{air} \tag{1}$$

The regression uses annual pairs of anomalies instead of successive values in the time series. This pairing is illustrated in Fig.S1. Since this definition of albedo feedback does not include lags that may cause albedo change (e.g., a low albedo year pre-conditions the next year for low albedo), an alternative formulation of albedo feedback (referred to as the bulk albedo feedback ($\alpha_{feedback,b}$) is considered, which is the change in $SW_{net}$ over the change of $T_{air}$:

$$\alpha_{feedback,b} = \Delta SW_{net} / \Delta T_{air} \tag{2}$$

#### *2.6.3 Equilibrium Line Altitude (ELA)*

Equilibrium line has zero annual mean SMB, separating the ice sheet accumulation zone and the ablation zone. To calculate the average ELA of the GrIS in our model, we define the following algorithm: Loop through the ablation grids using the annual mean SMB field. If any of the neighboring grids has positive SMB, compute the elevation where SMB equals zero using the two SMB and elevation values of this positive SMB grid (with grid area $a_p$) and the ablation grid (with grid area $a_n$). Save this computed elevation as one ELA value, with an approximate length of the shared edge of the two grids as the weight. The approximate edge length is calculated by $(\sqrt{a_n}+\sqrt{a_p})/2$. The final average ELA is the length-weighted average of all the saved ELA values.

## 3 Results

### 3.1 Response of the GrIS in the VR Run

To help visualize the spatial change patterns through time and later analyze the differences between `F09M`, `F09`, and `ARCTIC`, we will focus on three time periods: year 131-150, year 231-250, and year 331-350. Year 131-150 represents the $CO_2$ stabilization period. Year 231-250 and year 331-350 are one and two centuries after, respectively, with the latter also representing the end of our simulation.

Since atmospheric $CO_2$ radiative forcing is nearly logarithmic in concentration, the 1% yr$^{-1}$ increase of $CO_2$ causes a nearly linear rise in the annual average near-surface temperature (0.3 K per decade; Fig.2b). By $CO_2$ stabilization, the temperature increase is 5.0 K over the GrIS. Polar amplification (the ratio of Arctic and global temperature increase) is 1.8. GrIS amplification (the ratio of GrIS and global temperature increase) is much smaller (1.1) due to its perennial ice and snow cover. After $CO_2$ stops increasing, the annual average near-surface temperature still rises, albeit more slowly (0.2 K per decade) due to oceanic warming, adding another 3.8 K by the end of the simulation. The relatively small area of the GrIS results in a larger variability of annual average near-surface temperature compared to the Arctic and global mean.

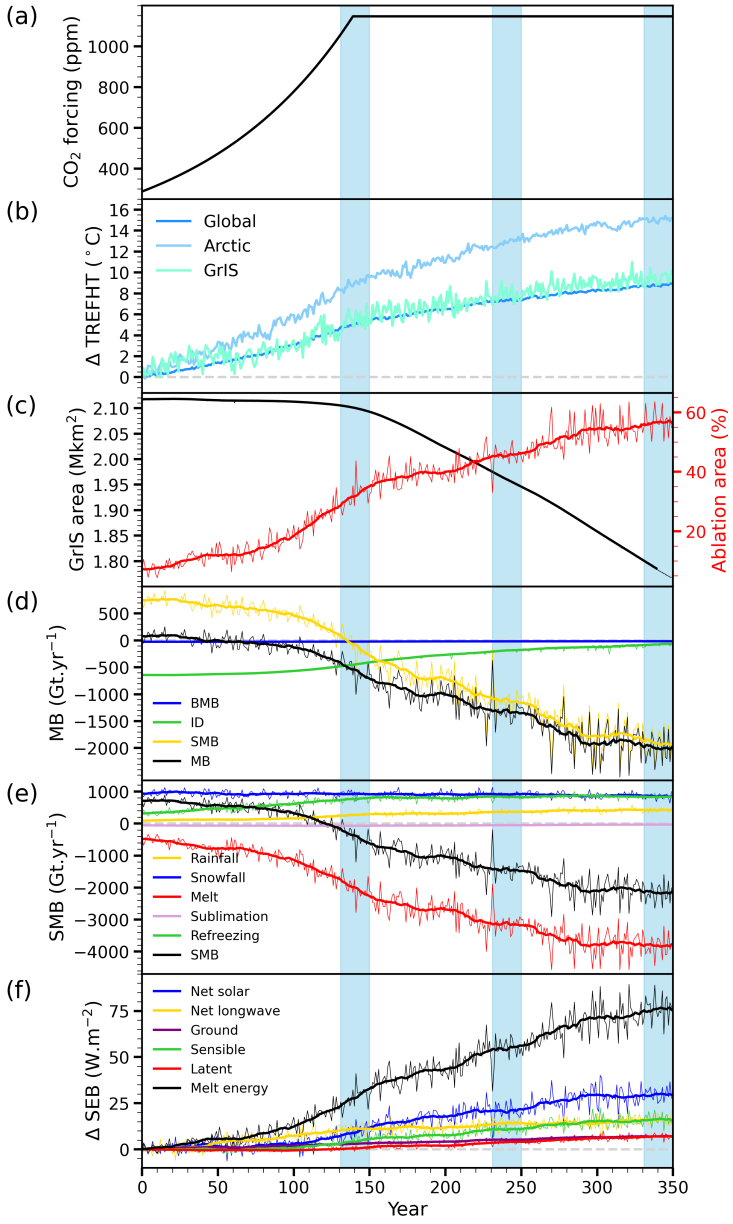


**Figure 2.** Evolution of (a) atmospheric $CO_2$ concentration (ppm), (b) global, GrIS, and Arctic region (north of 60°N) annual near-surface temperature anomaly with respect to the end of pre-industrial period (°C), (c) GrIS total area (left vertical axis, million km$^2$) and ablation area (%; as percentage of total ice sheet area), (d) mass balance (MB, black) and components (Gt yr$^{-1}$), (e) SMB (black) and components (Gt yr$^{-1}$), and (f) JJA anomaly of surface energy balance components compared to the end of pre-industrial period (W m$^{-2}$). The thick lines in (c)-(f) show the 20-year running means. The blue shaded periods are used in subsequent analysis.

Figure 2d shows the evolution of the GrIS-integrated mass balance and components. A similar pattern is found in Muntjewerf, Sellevold, et al. (2020). The mass loss accelerates after about 110 years, rising from 2.4 Gt yr$^{-2}$ before year 110 to 13.0 Gt yr$^{-2}$ between years 111 to 150. Then, after $CO_2$ stabilization, the GrIS mass loss decelerates

gradually, combined with larger oscillations and variability. With the mass loss, the ice sheet area shrinks, decreasing from 2.1 × $10^6$ km$^2$ to 1.8 × $10^6$ km$^2$ (Fig.2c). The cumulative contribution to global mean sea level rise (GMSLR) is 53 mm by year 150 and 831 mm by year 350 (Table 1). The decreasing SMB dominates the mass balance trend (Fig.2d), which becomes negative at around year 130. Ice discharge gradually decreases as marine-terminating outlet glaciers thin, decelerate, and even transition to land-terminating glaciers.

**Table 1.** Annual Rate of Mass Loss (mm yr$^{-1}$), Cumulative GrIS Mass Loss (mm), Mass Balance Components (Gt yr$^{-1}$), GrIS Area ($10^6$ km$^2$), and GrIS Volume ($10^6$ km$^3$).

| | Last 20 yrs of CTRL | | | Years 131-150 | | | Years 231-250 | | | Years 331-350 | | |
|---|---|---|---|---|---|---|---|---|---|---|---|---|
| | F09M | F09 | ARCTIC | F09M | F09 | ARCTIC | F09M | F09 | ARCTIC | F09M | F09 | ARCTIC |
| Annual mass loss | -0.04 | -0.10 | -0.05 | 2.08 | 2.06 | 1.48 | 5.28 | 4.49 | 3.50 | 6.36 | 5.93 | 5.40 |
| Cumulative mass loss | -0.8 | -2.0 | -1.1 | 97 | 84 | 53 | 501 | 447 | 344 | 1,098 | 976 | 831 |
| MB | 19 | 41 | 23 | -776 | -761 | -542 | -1,974 | -1,669 | -1,285 | -2,376 | -2,195 | -2,001 |
| SMB | 616 | 723 | 685 | -380 | -319 | -72 | -1,797 | -1,463 | -1,081 | -2,284 | -2,097 | -1,909 |
| ID | 573 | 654 | 636 | 376 | 420 | 448 | 161 | 187 | 187 | 78 | 81 | 77 |
| BMB | -24 | -27 | -25 | -20 | -22 | -22 | -16 | -18 | -18 | -14 | -16 | -16 |
| GrIS area | 1.97 | 2.00 | 2.02 | 1.92 | 1.96 | 1.99 | 1.77 | 1.80 | 1.83 | 1.60 | 1.64 | 1.66 |
| GrIS volume | 3.23 | 3.27 | 3.25 | 3.20 | 3.24 | 3.23 | 3.05 | 3.10 | 3.12 | 2.81 | 2.89 | 2.93 |

Notes: Mass Balance (MB) = Surface Mass Balance (MB) - Ice Discharge (ID) + Basal Melt Balance (BMB). Variables in this table are calculated using CISM2 outputs.

The accelerating SMB trend (decreasing) is dominated by the surface melt trend. Figure 2e shows the evolution of SMB components. Surface melt increases profoundly: the annual surface melt during year 131-150 and year 331-350 are more than four times and eight times larger than the pre-industrial value, respectively (Table 2). The total precipitation increases from the start due to increased rainfall but decreases during the last century as the decreasing trend of snowfall dominates. By the end of the simulation, the precipitation is about a quarter higher than the pre-industrial value (Table 2). Though snowfall remains the major precipitation type, the proportion of liquid phase precipitation gradually grows through time, making up nearly one-third of the total precipitation by the end of the simulation (Table 2). Refreezing increases before $CO_2$ stabilization as more liquid water is available from both increased rainfall and surface melt, and then becomes relatively stable due to saturated snow cover. This is also reflected by the refreezing capacity - defined as the fraction of refreezing to available liquid water - decreasing from 55.4% pre-industrial to 19.7% by the end of the simulation (Table 2). Sublimation is relatively small throughout the simulation, so is not discussed further.

**Table 2.** Annual Ice Sheet-Integrated Surface Mass Balance and Components Mean (Gt yr$^{-1}$).

| | Last 20 yrs of CTRL | | | Years 131-150 | | | Years 231-250 | | | Years 331-350 | | |
|---|---|---|---|---|---|---|---|---|---|---|---|---|
| | F09M | F09 | ARCTIC | F09M | F09 | ARCTIC | F09M | F09 | ARCTIC | F09M | F09 | ARCTIC |
| SMB (4km) | 616 | 723 | 685 | -380 | -319 | -72 | -1,797 | -1,463 | -1,081 | -2,284 | -2,097 | -1,909 |
| SMB | - | 701 | 651 | -745 | -620 | -369 | -2,213 | -1,752 | -1,398 | -2,552 | -2,254 | -2,159 |
| Precipitation | 942 | 1,026 | 955 | 1,047 | 1,273 | 1,200 | 1,106 | 1,374 | 1,277 | 1,156 | 1,308 | 1,265 |
| Snowfall | 850 | 934 | 869 | 782 | 961 | 930 | 699 | 932 | 913 | 695 | 819 | 849 |
| Rain | 92 | 92 | 86 | 265 | 312 | 270 | 406 | 443 | 364 | 461 | 488 | 416 |
| Refreezing | 142 | 295 | 307 | 680 | 872 | 758 | 784 | 956 | 824 | 781 | 1,019 | 830 |
| Melt | 485 | 476 | 468 | 2,147 | 2,400 | 1,986 | 3,662 | 3,606 | 3,083 | 4,009 | 4,073 | 3,806 |
| Sublimation | - | 52 | 57 | 60 | 53 | 70 | 34 | 34 | 52 | 19 | 19 | 32 |
| Rain (%) | 9.8 | 9.0 | 9.0 | 25.4 | 24.5 | 22.5 | 36.8 | 32.2 | 28.5 | 39.9 | 37.4 | 32.9 |
| Refreezing (%) | 24.6 | 51.9 | 55.4 | 28.2 | 32.2 | 33.6 | 19.3 | 23.6 | 23.9 | 17.5 | 22.3 | 19.7 |

Notes: SMB (4km) is calculated using CISM2 outputs. The other variables are calculated using CLM5 outputs. SMB = Snowfall + Refreezing – Melt – Sublimation. Rain (%) = Rain * 100 / (Snowfall + Rain). Refreezing (%) = Refreezing * 100 / (Rain + Melt).

316 The enhanced surface melt greatly reduces the SMB over the periphery of the GrIS.
317 Fig.3f-h show the spatial distribution of SMB difference compared to the pre-industrial
318 period, indicating the largest SMB decrease occurs along the southeast and west mar-
319 gins ($>$ 5,000 mm yr$^{-1}$ by the end of the simulation). In the ice sheet interior, SMB in-
320 creases due to the locally enhanced hydrological cycle. This spatial pattern of SMB changes
321 results in a similar spatial pattern of the ice sheet thickness changes, with slight thick-
322 ening over the high interior and significant thinning towards the margins (Fig.3j-l). The
323 largest thinning along the western margins can exceed 1000 m by the end of the simu-
324 lation. The surface ice velocity decreases at the ice sheet margins due to the thinning
325 of outlet glaciers, though generally, the surface ice velocity increases due to the steeper
326 surface slopes caused by the thickness changes (Fig.3n-p).

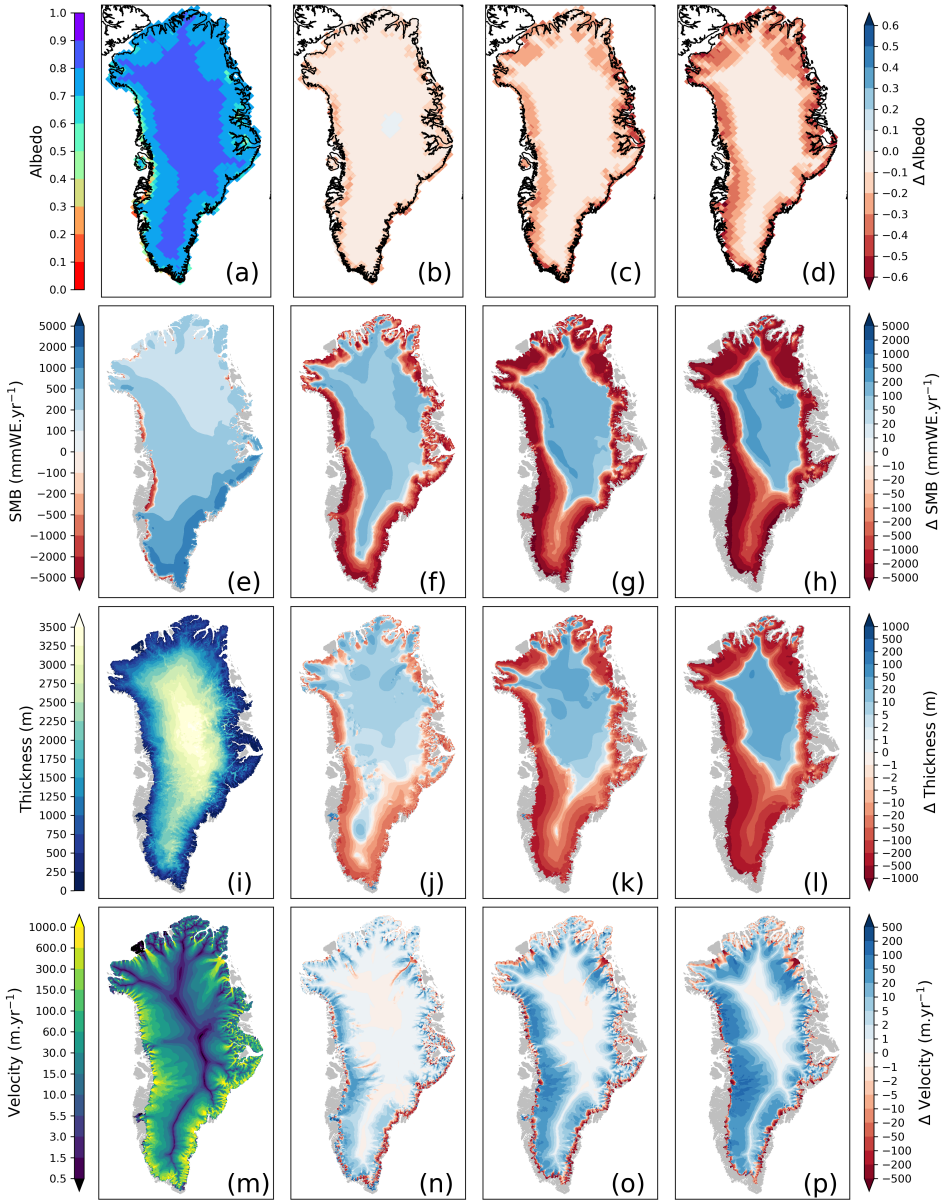


**Figure 3.** Spatial distribution over the GrIS for pre-industrial (first column) and differences with respect to the former by model years 131-150 (second column), 231-250 (thrid column) and 331-350 (forth column). (a-d) JJA mean albedo, (e-h) annual mean surface mass balance (mmWE $yr^{-1}$) with accumulation zones (SMB $> 0$) and ablation zones (SMB $< 0$), (i-l) ice sheet thickness (m), and (m-p) surface velocity (m $yr^{-1}$).

### 3.2 Drivers for melt changes

The spatiotemporal evolution of surface energy balance (SEB) components over the GrIS provides an explanation for the main physical drivers of accelerating surface melt. Figure 2f shows the summer (JJA) average anomalies of surface energy terms compared to the pre-industrial period. During the first century, the enhancement in net longwave radiation (less longwave cooling) from increased atmospheric temperature and cloudiness (Fig.S2a) provides most of the additional melting energy. The increased net short-

wave radiation is dampened by reduced incoming shortwave radiation (Fig.S2b) resulting from enhanced cloudiness (Fig.S2a). At around year 110, the contribution of net shortwave radiation to the melt energy increases rapidly, surpassing net longwave radiation at around year 148, and becoming the dominant melt energy contributor. At the end of the simulation, net shortwave radiation provides 37.3% of the total additional melt energy (Table 3). The accelerated net shortwave radiation increase at about year 110 is speculated to be due to the activation of the melt/albedo feedback. We find that the accelerated net shortwave radiation and melt increase coincides with a faster increase of ablation area (Fig.2c). As the ablation zone expands, darker surfaces with lower albedo are exposed, which absorbs more shortwave radiation and further enhances surface melting. The decrease of surface albedo mainly occurs within the ablation zones, with little change in the ice sheet interior (Fig.3b-d). The ice sheet hypsometry also contributes to the accelerated expansion of the ablation zone - the quasi-parabolic shape favors faster ablation area expansion as it approaches the interior plateau. The turbulent fluxes also increase at around year 110, although at slower speeds. As near-surface air temperature continues to rise, the surface temperature inversion becomes stronger, thus enhancing the turbulent fluxes. The contribution of sensible heat flux to total additional melt energy is comparable to the contribution of net longwave radiation by the end of the simulation (22.5% and 21.5%, respectively; Table 3). The latent heat flux becomes less negative through the simulation, which is potentially due to the decrease of sublimation as well as an increase in deposition and condensation. At the end of the simulation, 10.1% of the additional melt energy comes from latent heat flux (Table 3). The ground heat flux rises from negative to positive, which is potentially a result of more refreezing in the snow layer, and contributes 8.6% of the additional melt energy at the end of the simulation (Table 3).

**Table 3.** Summer GrIS-averaged Albedo, Near-Surface Temperature and Skin Temperature (°C), Incoming Shortwave Radiation, Incoming Longwave Radiation at the Surface, and Surface Energy Balance Components Mean (W $m^{-2}$).

| | Last 20 yrs of CTRL | | | Years 131-150 | | | Years 231-250 | | | Years 331-350 | | |
|---|---|---|---|---|---|---|---|---|---|---|---|---|
| | F09M | F09 | ARCTIC | F09M | F09 | ARCTIC | F09M | F09 | ARCTIC | F09M | F09 | ARCTIC |
| Albedo | 0.78 | 0.78 | 0.78 | 0.71 | 0.72 | 0.73 | 0.64 | 0.66 | 0.68 | 0.61 | 0.62 | 0.65 |
| $T_{2m}$ | -7.00 | -7.05 | -7.34 | -1.22 | -1.11 | -1.88 | 0.50 | 0.43 | -0.22 | 1.03 | 1.21 | 0.79 |
| $T_{skin}$ | -7.83 | -7.83 | -8.42 | -2.14 | -2.15 | -3.10 | -0.74 | -0.85 | -1.74 | -0.31 | -0.20 | -0.96 |
| $SW_{in}$ | 288.3 | 286.4 | 294.3 | 262.0 | 261.7 | 272.6 | 255.9 | 254.9 | 266.6 | 250.9 | 253.4 | 264.0 |
| $LW_{in}$ | 231.0 | 232.6 | 224.1 | 267.7 | 268.5 | 257.8 | 276.1 | 276.8 | 266.7 | 280.3 | 280.7 | 271.6 |
| Melt energy | 8.8 | 8.5 | 8.4 | 40.3 | 43.4 | 35.7 | 71.0 | 68.3 | 59.7 | 84.6 | 83.6 | 80.0 |
| $SW_{net}$ | 64.0 | 62.1 | 64.9 | 73.5 | 72.8 | 73.5 | 89.5 | 84.9 | 83.2 | 94.8 | 92.8 | 91.6 |
| $LW_{net}$ | -50.6 | -49.0 | -55.3 | -38.2 | -37.3 | -44.0 | -36.1 | -34.9 | -41.2 | -34.1 | -34.1 | -39.9 |
| SHF | 4.8 | 4.5 | 7.1 | 8.4 | 10.4 | 11.2 | 14.2 | 14.7 | 17.6 | 16.1 | 16.7 | 23.3 |
| LHF | -8.3 | -8.0 | -7.5 | -6.9 | -5.4 | -7.1 | -2.7 | -2.3 | -3.6 | -0.6 | 0.1 | -0.3 |
| GHF | -1.2 | -1.1 | -0.8 | 3.6 | 2.9 | 2.1 | 6.1 | 5.9 | 3.8 | 8.4 | 8.2 | 5.3 |

Notes: Melt energy = net shortwave radiation $SW_{net}$ + net longwave radiation $LW_{net}$ + sensible heat flux SHF + latent heat flux LHF + ground heat flux GHF.

To examine the role of large scale circulation on summer GrIS surface melt, we calculated the GBI. Figure 4a shows the evolution of the GBI for ARCTIC. There is a negative trend of the GBI before $CO_2$ stabilization, which indicates weakening summer blocking over the Greenland region. This agrees with the result of Sellevold and Vizcaíno (2020), which uses an AMIP style configuration of CESM2.1 under the same 1% $yr^{-1}$ $CO_2$ warming scenario. After $CO_2$ stabilization, there is no significant trend for GBI. Figure 4b shows the linear regression between GrIS-integrated JJA melt, and the JJA GBI. Both variables are filtered with a 10-year high-pass filter, thus representing the sub-decadal timescale. On sub-decadal timescales, the GBI explains 40% of the annual variability of summer surface melt. A more negative GBI results in less surface melt. Therefore, this indicates the GBI (more general the atmospheric circulation pattern) is not a driver of the melt

acceleration at about year 110, but actually counteracts part of the effect of global warming on the surface melt before $CO_2$ stabilization.

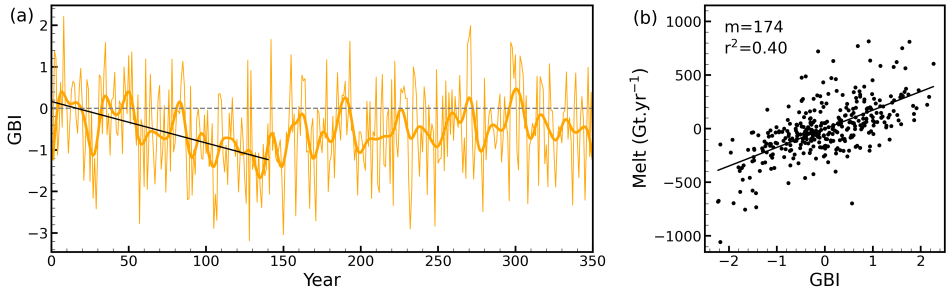


**Figure 4.** Evolution of the Greenland Blocking Index for `ARCTIC` (a), and the regression of JJA GrIS-integrated filtered surface melt (Gt $yr^{-1}$) onto JJA filtered Greenland Blocking Index (b). The thick orange line in (a) shows the 10-year low-pass filtered time series. The timescale of the filtered quantities effectively removes both the mean and the trend of each time series. Black line is drawn where the regression is significant, with an annotated m (slope), and $r^2$ for the explained variance for (b).

## 3.3 Impacts of Enhanced Resolution

### *3.3.1 Large-scale Climate*

Before delving into the simulated GrIS responses, we first compare the representations of large-scale climate conditions between the regionally-refined `ARCTIC` run and the 1° runs. Figure 5a-c show the summer mean 500 hPa geopotential height for `ARCTIC` during the three time periods - year 131-150, year 231-250, and year 331-350. As the atmosphere warms, the 500 hPa geopotential height increases over the northern high latitudes. The differences between `ARCTIC` and the 1° runs show a consistent pattern during each period (Fig.5d-i). Compared to `F09M` and `F09`, `ARCTIC` has significantly lower 500 hPa geopotential height over Greenland except for the period year 331-350 for `ARCTIC` and `F09M`, which possibly indicates weaker blocking and less anticyclonic flows over the GrIS in `ARCTIC`. This lower geopotential region in `ARCTIC` extends over the Canadian Archipelago during year 131-150. There is also significant higher geopotential over subpolar regions in `ARCTIC` compared to `F09M` and `F09`, especially during year 331-350.

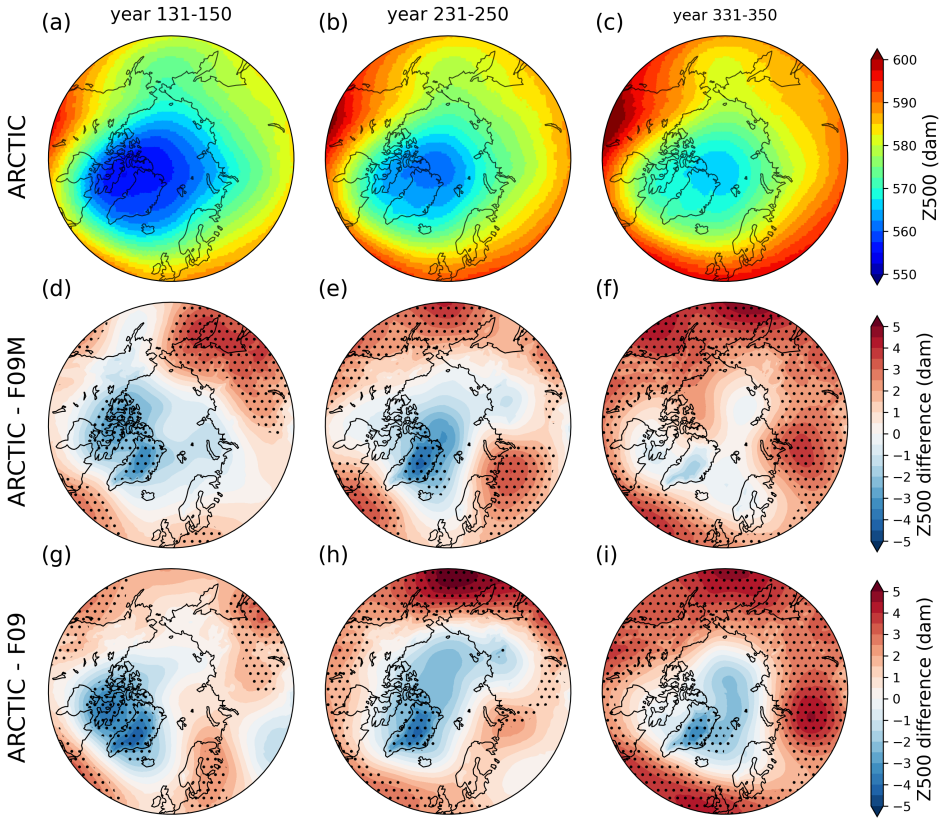


**Figure 5.** Northern hemisphere summer 500 hPa geopotential height (dam) of `ARCTIC` (a-c), and the difference between `ARCTIC` and `F09M` (d-f), `ARCTIC` and `F09` (g-i). The three columns from left to right represent averaged periods year 131-150, year 231-250, and year 331-350, respectively. Dotted regions are where the two simulations are significantly different ($p < 0.05$) by student t test.

Figure 6 compares the summer temperature over the northern hemisphere between `ARCTIC` and the 1° runs. The lower-troposphere summer virtual temperature, computed by equating a layer mean virtual temperature with the 500–1,000 hPa geopotential thickness, is higher in `ARCTIC` over much of the northern hemisphere (Fig.6a-f). This agrees with the common response to increasing horizontal resolution (also reducing physics time step) in general circulations models (GCMs) (Pope & Stratton, 2002; Roeckner et al., 2006) including CAM (Herrington & Reed, 2020): increasing the horizontal resolution warms the climate, since higher resolved vertical velocities generate more condensational heating. However, `F09M` and `F09` have warmer lower troposphere than `ARCTIC` centered over the GrIS, which also extends to Canadian Archipelago and Alaska during year 131-150 (Fig.6a,d) and to East Siberia during year 231-250 (Fig.6b,e). This spatial pattern of lower-troposphere virtual temperature differences agrees with that of the 500 hPa geopotential height difference, indicating that probably the stronger summer blocking over Greenland regions in `F09M` and `F09` causes the higher lower-troposphere virtual temperature there. Compared to the lower troposphere, the near-surface temperature difference shows a distinct spatial pattern with larger magnitudes (Fig.6g-l). Except for some terrestrial regions (e.g., parts of Siberia and Eurasia), `ARCTIC` is significantly cooler than `F09M` and `F09` at near-surface level. This results from the different pre-industrial climate, in which `ARCTIC` is cooler, likely due to increasing the albedo of snow over sea ice to tune this run. The regions where the lower troposphere is cooler in `ARCTIC` during year 131-150 and year

231-250 also have much lower near-surface temperature. However, the near-surface temperature differences over the GrIS are much smaller due to its perennial ice and snow cover. There are also regions at the ice sheet periphery that are warmer in ARCTIC. This is caused by the difference of cloud conditions, which is discussed in Section 3.3.3.

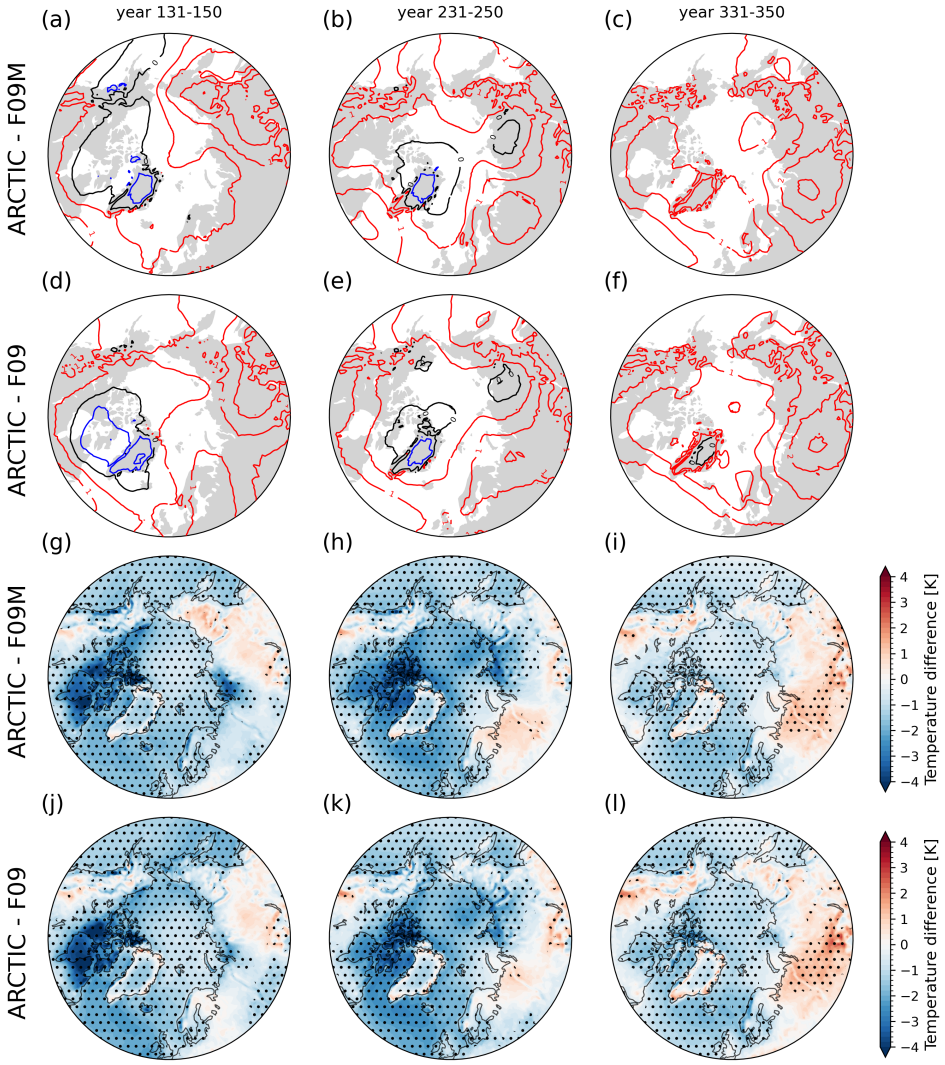


**Figure 6.** Northern hemisphere summer lower troposphere virtual temperature differences (K) between ARCTIC and F09M(a-c), ARCTIC and F09(d-f). Lower troposphere layer mean virtual temperature is derived from the 1,000–500 hPa geopotential thickness, using the hypsometric equation. Northern hemisphere summer near-surface air temperature differences (K) between ARCTIC and F09M(g-i), ARCTIC and F09(j-l). The three columns from left to right represent averaged periods year 131-150, year 231-250, and year 331-350, respectively. Dotted regions are where the two simulations are significantly different ($p < 0.05$) by student t test.

The NAMOC evolution is insensitive to the enhanced resolution in the atmosphere. The three simulations have very similar NAMOC index, and even their initial differences are diminished. During the period of $CO_2$ increase, the NAMOC weakens significantly (Fig.7a, with the NAMOC index decreasing by 0.14 Sv $yr^{-1}$, 0.13 Sv $yr^{-1}$, and 0.12 Sv

414 $yr^{-1}$ in `ARCTIC`, `F09M`, and `F09`, respectively. Then the NAMOC index gradually stabi-
415 lizes and remains at about 5 Sv for almost two centuries. We also compare the evolu-
416 tion of the NAMOC index with the total freshwater flux from the GrIS into the ocean
417 (Fig.7b). The total freshwater flux is calculated by adding up surface runoff, basal melt,
418 and solid ice discharge. The NAMOC index declines at the start of $CO_2$ increase, which
419 is much earlier than the rapid increase freshwater flux at around year 110, and remains
420 stable when the freshwater flux keeps increasing. This relationship is also found in sim-
421 ulations under SSP5-8.5 forcing (Muntjewerf, Petrini, et al., 2020), which suggests the
422 relatively limited role of additional freshwater input from the GrIS on NAMOC weak-
423 ening compared to global warming in CESM2.

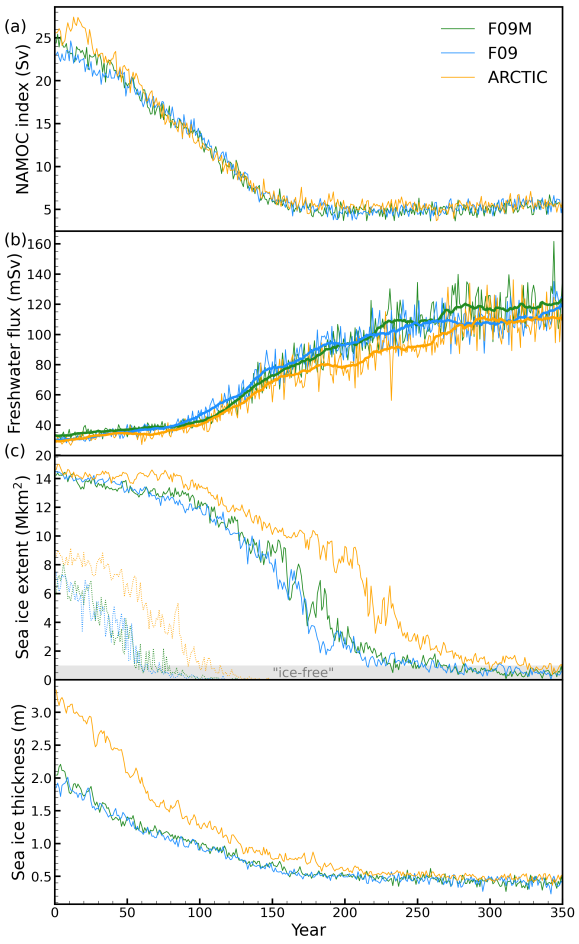


**Figure 7.** Evolution of the annual mean (a) NAMOC index (Sv), (b) total freshwater flux into the ocean (mSv), (c) Northern Hemisphere sea ice extent (million $km^2$; ice concentration > 15%), and (d) averaged sea ice thickness (m). The thick lines in (b) represent 20-year running means. The dotted lines in (c) represent September mean sea ice extent and the gray shaded range represents the "ice-free" condition.

424 Slower decline of Northern Hemisphere sea ice extent is found in `ARCTIC` compared
425 to the 1° runs (Fig.7c). In the 1° runs, the Arctic becomes ice-free (sea ice extent < one
426 million $km^2$) in September after about 60 years, while this happens about five decades
427 later in `ARCTIC`. There is an acceleration of annual sea ice decline ((Fig.7c)) at around

year 90 for all the simulations. This is possibly because the ice-free Arctic ocean absorbs more radiation, which stores more heat in the ocean and slows down sea ice formation in colder seasons, but the reason for the timing needs further investigation. Before the Arctic becomes ice-free all year round by the end of the simulation, `ARCTIC` has larger sea ice extent than the 1° runs due to its slower sea ice decline during the first two centuries. This is mostly driven by the larger initial sea ice thickness in `ARCTIC` of the warming scenario (Fig.7d), which is a result of increasing the albedo of snow over sea ice in `ARCTIC` during the tuning process.

#### *3.3.2 SMB Evolution and Ice Sheet Changes*

The evolution of ice sheet-integrated quantities in the three simulations follows a similar pattern but with different magnitudes and timing. Figure 8b compares the evolution of the GrIS-integrated SMB of the three simulations. Compared to the 1° runs, the SMB in `ARCTIC` decreases more slowly, such that by the end of the simulation, the drop of annual SMB in `ARCTIC` is 306 Gt $yr^{-1}$ and 226 Gt $yr^{-1}$ (∼10%) smaller than `F09M` and `F09`, respectively (Table 1). This SMB difference mainly results from the difference in melt, with `ARCTIC` generally producing less surface melt than `F09M` and `F09`, especially around the period year 180-260 (Fig.8a). During year 231-250, the GrIS-integrated melt in `F09M` and `F09` is 579 Gt $yr^{-1}$ and 523 Gt $yr^{-1}$ larger than `ARCTIC`, respectively (Table 1). The difference in precipitation is relatively small (Fig.8a). `F09` has larger precipitation than `ARCTIC`, which compensates some of its larger melt and results in smaller SMB difference. In `F09M`, the adjustments that direct cold-rain to surface runoff and increase sub-grid roughness over Greenland greatly reduce precipitation. Compared to `F09`, it causes a 204 Gt $yr^{-1}$ reduction of annual total precipitation averaged over the 350 years. The slower SMB decrease of `ARCTIC` causes slower decrease of MB (Fig.8c), and thus slower ice volume decrease (Fig.8d) and smaller global mean sea level rise (GMSLR) contribution (Fig.8e). Over the whole 350 years, `F09M` and `F09` contribute to 267 mm and 145 mm (∼20%) more GMSLR than `ARCTIC`, respectively (Table 1). We note the different initial ice volume and initial mass balance of the three simulations, which will be discussed in Section 4.

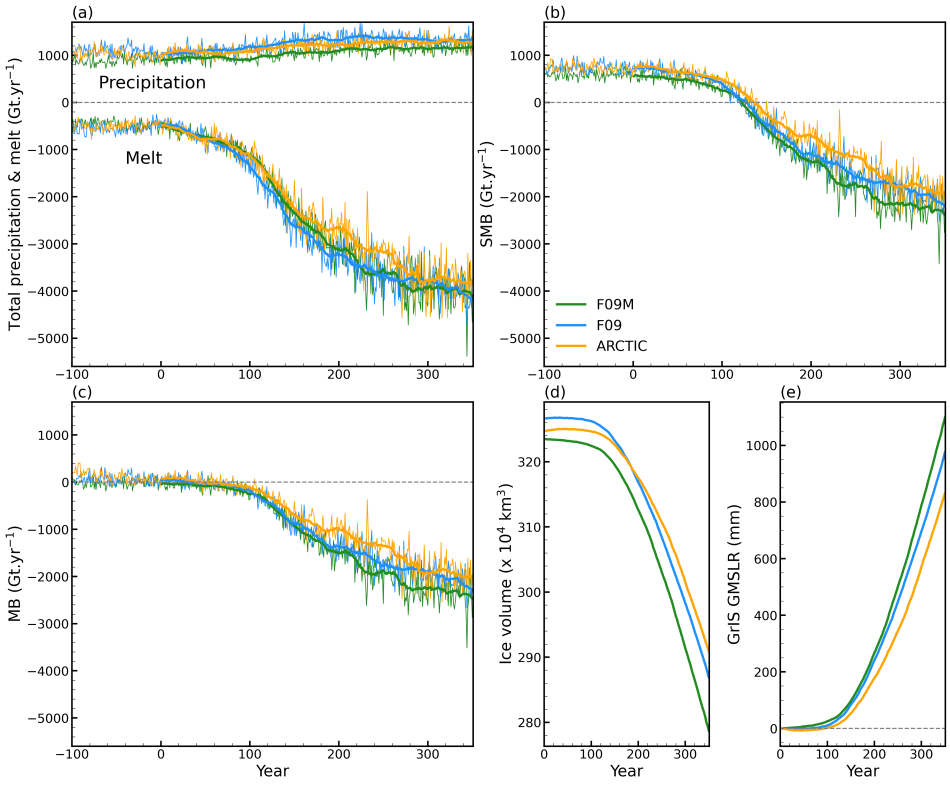


**Figure 8.** Evolution of GrIS-integrated (a) total precipitation and melt (Gt yr$^{-1}$), (b) SMB (Gt yr$^{-1}$), (c) MB (Gt yr$^{-1}$), (d) ice volume ($\times$ 10$^4$ km$^3$), and (e) accumulated contribution to global mean sea level rise (mm) for the three simulations. The thick lines in (a)-(c) represent 20-year running means.

Averaged over the whole 350 years, the smaller melt in `ARCTIC` is most significant along the ice sheet periphery in western and northern GrIS, where `F09M` and `F09` melt over 300 mm more ice each year (Fig.9c,d). The south tip shows the reverse of the larger spatial pattern, with more melt in `ARCTIC`. This is due to the weaker cloud shortwave cooling there in `ARCTIC` (discussed in Section 3.3.3). The spatial pattern of melt difference is consistent for `ARCTIC` compared to `F09M` and `F09` despite their different initial conditions (Fig.8d). The spatial pattern of total precipitation difference is almost the opposite for `ARCTIC` compared to `F09M` and `F09`, with the former having lower precipitation and the latter having larger precipitation centered over the south and southeast coasts (Fig.9a,b). Due to the smoother topography in the 1° grid, there is more moisture penetration into the ice sheet from southeast. For `F09M`, the effect of directing cold-rain to surface runoff and increasing sub-grid roughness is evident, which greatly reduces the total precipitation. Over the 350 years, weaker ice sheet thinning (difference $>$ 100 m) is found in `ARCTIC` especially along the western and northern peripheries compared to the 1° runs (Fig.9e,f). The larger precipitation in `F09` reinforces its smaller melt in the south tip, resulting in less ice sheet thinning there.

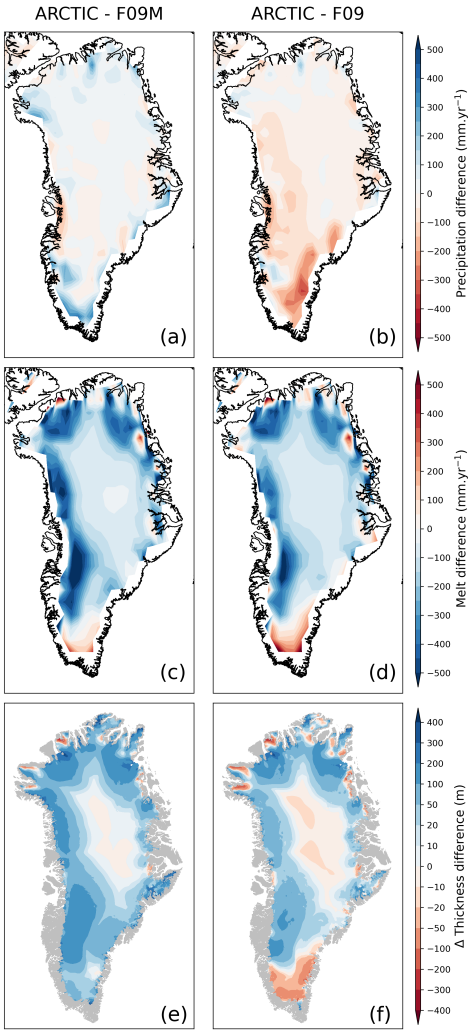


**Figure 9.** Maps of the difference between `ARCTIC` and `F09M` (left column), `ARCTIC` and `F09` (right column): (a-b) annual mean precipitation (mm $yr^{-1}$), (c-d) surface melt (mm $yr^{-1}$) averaged over the whole 350 years, and (e-f) ice thickness change (m) between the end of the simulation and the end of pre-industrial period. Blue color indicates more precipitation, less melt, or less thinning. For precipitation and melt, `ARCTIC` results are remapped to the `f09` grid for the comparison.

### *3.3.3 Surface Energy Balance*

To explain the differences in meltwater production between `ARCTIC` and the 1° runs, we examine how incident radiation is impacted by cloud conditions. Figure 10a,b illustrate the summer mean cloud fraction difference between `ARCTIC` and the 1° runs. There is a ring of cloud fraction surplus around the ocean perimeter of Greenland in `ARCTIC`, which is similar to previous findings in (Herrington et al., 2022). Lower cloud fraction in `ARCTIC` is found in the northern and southern peripheries, while in between the cloud fraction can be higher compared to the 1° runs, especially during year 231-250. This pattern is different to that in Herrington et al. (2022), where the smoother topography in lower resolution runs causes more moisture intrusion thus larger cloud fraction in the ice sheet interior. The higher pressure in the 1° runs over the GrIS (Fig.5) may contribute

to their lower cloud fraction by generating stronger large-scale subsidence and cloud dissipation. The spatial pattern of total cloud liquid water path (LWP) difference over the GrIS generally follows that of cloud fraction difference, except for the much larger LWP in the southern interior in `ARCTIC` (Fig.5c,d). The pattern of cloud difference impacts the incident radiation. In `ARCTIC`, the incident shortwave radiation is generally larger due to less cloud cover or thinner clouds, especially in northern Greenland and along the ice sheet margins (Fig.10e,f). At the same time, smaller incident longwave radiation is found all over the ice sheet for `ARCTIC` (Fig.10g,h), with the largest differences along the north and southeast margins. This is a combined effect of the cloud conditions and lower free atmosphere temperature over Greenland in `ARCTIC`.

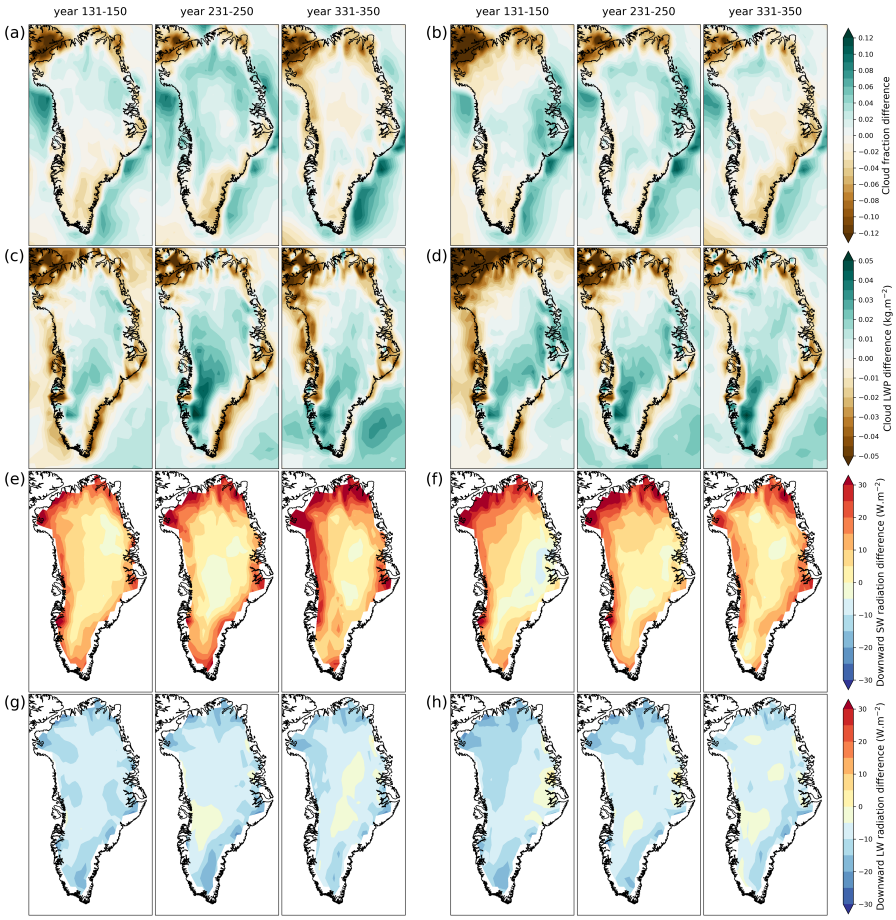


**Figure 10.** Maps of the difference between `ARCTIC` and `F09M` (left three columns), `ARCTIC` and `F09` (right three columns): (a-b) JJA mean cloud fraction, (c-d) total cloud liquid water path (kg m$^{-2}$), (e-f) downward shortwave radiation (W m$^{-2}$), and (g-h) downward longwave radiation (W m$^{-2}$) averaged over three periods: year 131-150, year 231-250, and year 331-350.

Differences in the representation of clouds and the resultant incident radiation have a direct impact on SEB terms and thus total energy available for melt. Despite the overall larger incident shortwave radiation in `ARCTIC`, especially along the ice sheet margins, it has smaller net shortwave radiation in the interior compared to the 1° runs, peaking at the gently sloping ice surface in the western and northern basins (or transitional area) (Fig.11a,b). Therefore, the albedo in these regions of `ARCTIC` must drop more slowly than

those in the 1° runs. The net shortwave radiation difference during year 131-150 is still small, and it becomes dominant in the SEB during year 231-250 and year 331-350. The spatial pattern of net longwave radiation difference (Fig.11c,d) is consistent with the pattern of incident longwave radiation (Fig.10g,h), suggesting the weaker cloud longwave warming effect in `ARCTIC`. The spatial pattern of differences in net longwave radiation is consistent through time. Compared to the radiative fluxes, the difference of turbulent fluxes between `ARCTIC` and the 1° runs is relatively small (Fig.11e-h). The above mentioned gently sloping ice surface in the western and northern basins also favors smaller sensible and latent heat fluxes in `ARCTIC`. Larger sensible heat flux is found in `ARCTIC` along the ice sheet margins especially during year 331-351, which originates from the higher near-surface temperature there (Fig.6g-l). The difference of ground heat flux is small between `ARCTIC` and the 1° runs (not shown). As the sum of the above SEB terms, the total melt energy difference has a spatial pattern that agrees with the averaged melt difference (Fig.9c,d). In the aggregate, the spatial distribution of the lower melt energy in `ARCTIC` (Fig.11a,b) mainly results from the combination of smaller net shortwave radiation due to higher surface albedo and smaller net longwave radiation due to lower cloud fraction.

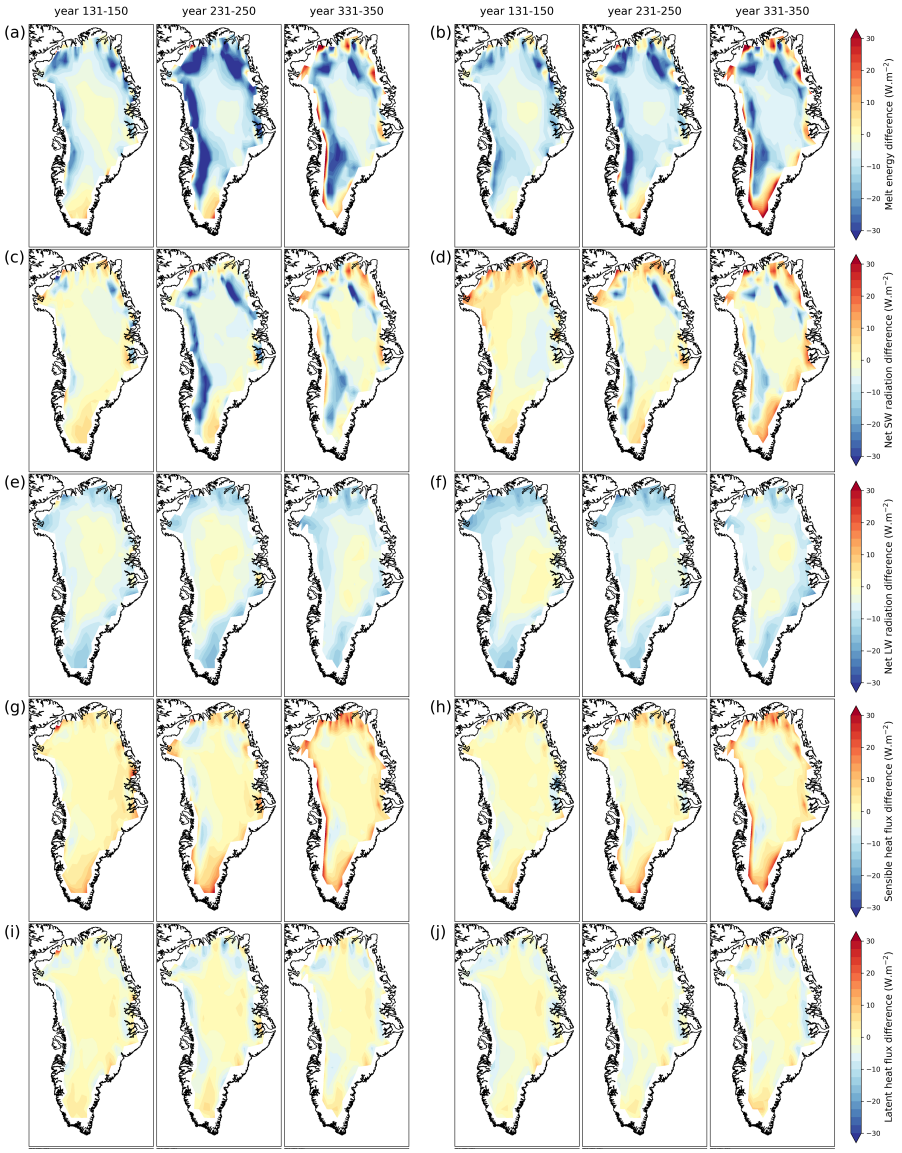


**Figure 11.** Maps of the difference between `ARCTIC` and `F09M` (left three columns), `ARCTIC` and `F09` (right three columns): (a-b) JJA mean total melt energy, (c-d) net shortwave radiation, (e-f) net longwave radiation, (g-h) sensible heat flux, and (i-j) latent heat flux averaged over three periods: year 131-150, year 231-250, and year 331-350 in the unit of W m$^{-2}$. Grids that do not have 100 percent ice fraction were masked out to avoid bias caused by comparing grids with different ice fraction.

### *3.3.4 Melt/albedo Feedback and the Impact of Ice Sheet Hypsometry*

We speculate that the slower decrease in albedo in `ARCTIC` is caused by a weaker albedo feedback. We first examine the bulk albedo feedback (Eq.2), which captures the long-term change in net shortwave radiation versus near-surface temperature when time-lags are considered. Over the whole 350 years, the bulk albedo feedback of `ARCTIC` (Fig.12a) and the 1° runs (not shown) is all positive over the GrIS, meaning more shortwave radiation is absorbed as near-surface temperature rises. The positive bulk albedo feedback is concentrated in the ablation zones, peaking in the lower elevations in the gently slop-

ing western and northern basins (> 15 W m$^{-2}$ K$^{-1}$). Figure 12b and 12c show the difference of the bulk albedo feedback between `ARCTIC` and `F09M`, `ARCTIC` and `F09`, respectively. In general, `ARCTIC` has weaker bulk albedo feedback compared to the 1° runs. A weaker bulk albedo feedback means less shortwave radiation is absorbed given the same amount of near-surface temperature increase. The spatial patterns of the bulk albedo feedback difference agree well with those of the net shortwave radiation difference (Fig.11c,d), indicating a limited role of near-surface temperature increase on causing this pattern. Unlike the bulk albedo feedback that peaks in the lower elevations, the differences are larger over the higher ablation zones. We also examine the albedo feedback (Eq.1) using annual paired detrended anomalies of net shortwave radiation and near-surface temperature over the three 20-year periods. By definition, the albedo feedback reveals an interplay of physical mechanisms, but it is more sensitive to interannual variabilities (e.g., of snowfall), which may make it harder to interpret. The albedo feedback differences show a similar but more variable spatial pattern compared to those of the bulk albedo feedback during year 231-250 and year 331-350 (Fig.S3e-f,h-i) when the albedo feedback is strong (Fig.S3b-c). The difference between bulk albedo feedback and albedo feedback also stresses the importance of melt preconditioning effect on following melt seasons.

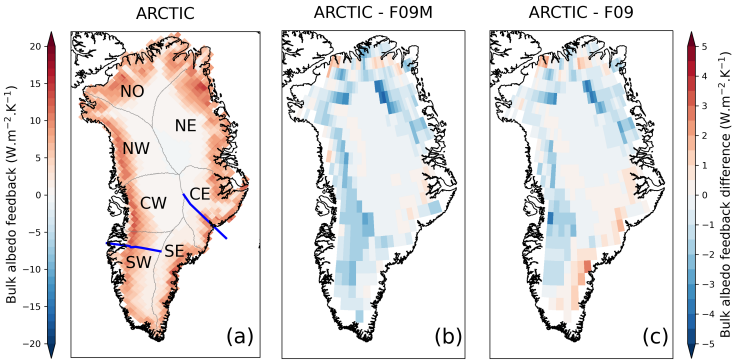


**Figure 12.** Maps of the bulk albedo feedback (W m$^{-2}$ K$^{-1}$) defined by $\Delta SW_{net}/\Delta T_{air}$ of `ARCTIC` (a), and the difference between `ARCTIC` and `F09M` (b), `ARCTIC` and `F09` (c). Time changes from the end of pre-industrial period to the end of the simulation. Gray lines in (a) separate the seven drainage basins defined by Rignot and Mouginot (2012), and blue lines show the location of the two transects plotted in Figure 15.

The difference in albedo feedback between `ARCTIC` and the 1° runs can be largely explained by the different representations of surface topography in different resolution. Figure 13 shows the surface elevation-cumulative area relationships in the three simulations for the whole ice sheet and the individual basins defined by Rignot and Mouginot (2012). A steeper slope in the elevation-cumulative area relationship indicates a larger area increase per meter of elevation rise, thus representing a flatter topography. Ryan et al. (2019) demonstrates the dominant role of Greenland's seasonally fluctuating snowline for reducing ice sheet albedo compared to bare ice albedo reduction caused by melt processes. Here, instead of the end-of-summer snowline elevation, we use the ELA to avoid the possible difficulties of snowline classification. Though different due to processes like superimposed ice formation (Cogley et al., 2011), a significant correlation is found between the ELA and the end-of-summer snowline elevation (Fausto & the PROMICE team*, 2018). For the whole ice sheet, the average ELA rises from around 600 m to 2,500 m over the 350 years. Within this range, `ARCTIC` has a less steep slope of the elevation-cumulative area relationship than the 1° runs (Fig.13a), indicating a smaller area increase with the

same amount of elevation rise. The slope difference between `ARCTIC` and the 1° runs becomes even larger at the end of the simulation compared to the start. Figure 14b shows the relationships between annual mean ELA and ablation area of the three simulations. The match between the simulated ELA-ablation area relationship and the elevation-cumulative area relationship demonstrates the role of topography on regulating the speed of ablation zone expansion. With the same amount of ELA increase, the ablation area increment in `ARCTIC` is smaller due to its steeper topography, which results in a slower ablation zone expansion (Fig.14a) and thus smaller albedo feedback of `ARCTIC` (Fig.12b,c). To further verify the result, the annual mean ablation area and ELA are also computed based on the `ARCTIC` outputs but remapped to the f09 grid (`ARCTIC2f09`) using the Earth System Modeling Framework (ESMF) first-order conservative remapping algorithm (ESMF Joint Specification Team, 2021). A similar slower ablation area expansion and smaller slope of the ELA-ablation area relationship is found for `ARCTIC2f09` (purple line and dots in Fig.14) compared to the 1° runs, which attests our theory.

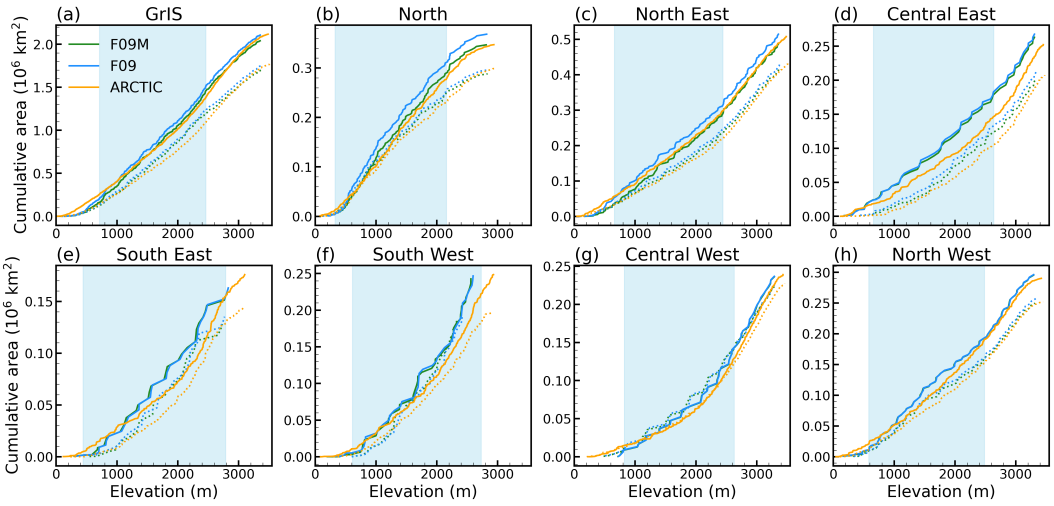


**Figure 13.** Hypsometric surface elevation-area relationships for the whole GrIS (a) and for different basins defined by Rignot and Mouginot (2012) (b-h). For the colored lines, the solid lines represent year 0, and the dotted lines represent year 350. The blue shaded elevation range indicates the annual GrIS- or basin-mean ELA variability in `ARCTIC` during the 350 years.

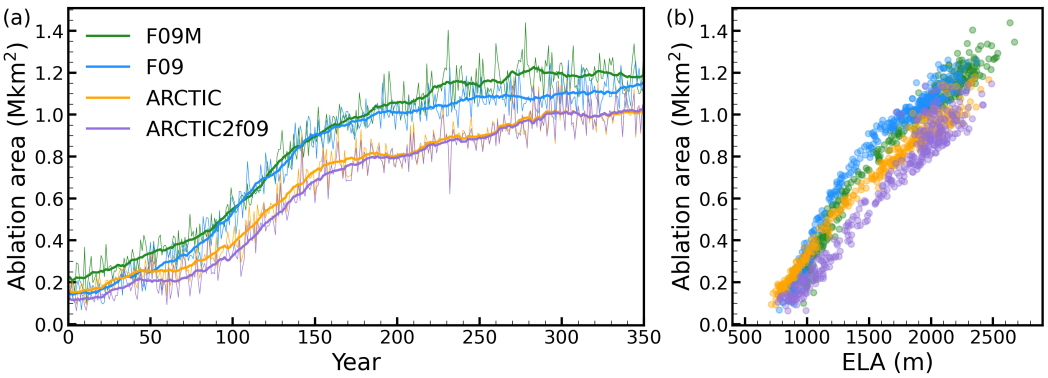


**Figure 14.** Evolution of the annual mean ablation area (Mkm$^2$) (a) and the relationship between ablation area and mean equilibrium line altitude over the Greenland Ice Sheet (b).

Aside from topography, other factors can also affect albedo feedback. Along the southeast coast, the larger precipitation in `F09` (Fig.9b) potentially slows down the albedo reduction more effectively, leading to its smaller bulk albedo feedback there compared to `ARCTIC` (Fig.12c). The impact of clouds on net shortwave radiation also cannot be eliminated from the bulk albedo feedback calculation. However, since the cloud pattern differences that cause more downward shortwave radiation in `ARCTIC` (Fig.10e,f) would play en opposite role, it is not considered as a contributor to the major albedo feedback differences.

Due to the regional dependence of ELA and surface topography, we also check the elevation-cumulative area relationship within separate GrIS drainage basins. The slope difference between `ARCTIC` and the 1° runs is largest within the steepest Central East and South East Basins (Fig.13d,e), but due to the narrow ablation zones and large precipitation in these basins, it does not result in large difference of the albedo feedback. For all the other basins where the albedo feedback is smaller in `ARCTIC` such as the South West, we also find that it has less steep slopes of the elevation-cumulative area relationship compared to the 1° runs (Fig.13f). This consists with our hypothesis that the topography represented in different resolution grids causes the albedo feedback differences.

The different representations of surface topography originate from the grid resolution differences and also the related numerical modeling requirements. Figure 15 shows the representation of the ice sheet surface along two transects (positions shown in Figure 12a) for the three simulations at different times. One is the east-west "K-transect" in southwest Greenland and the other is a transect extending from the central dome down to the Kangerlussuaq glacier on the southeast coast. Compared to `ARCTIC`, the coarser 1° grids have fewer grid cells along the transects, which may result in flatter surfaces locally. Moreover, the smoothing and flattening of the raw topography, necessary to prevent the model from exciting grid-scale numerical modes (Herrington et al., 2022), causes the lower-elevation ablation zones to extend beyond the true ice sheet margin more in the 1° runs. It results in flatter slopes along the transects in `F09M` and `F09`, which favor faster ablation zone expansion. For the more gently sloping K-transect (Fig.15a) with a relatively wide ablation zone (can climbs up the whole transect), this impact of surface slope is more significant as reflected in the bulk albedo feedback (Fig.12b,c). However, for the steeper southeast transect (Fig.15b) where the ablation zone below ∼2600 m is relatively narrow, the impact is limited.

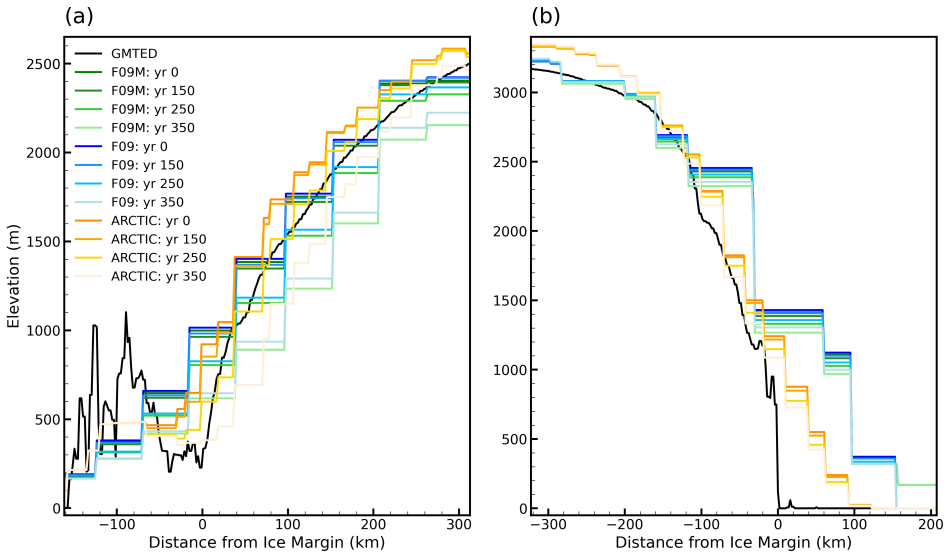


**Figure 15.** Model surface elevation (m) along the (a) K-transect, and (b) a transect spanning the central dome down to the Kangerlussuaq glacier in southeast Greenland, for `F09M`, `F09`, and `ARCTIC` at different times. The GMTED reference surface is a 1 km surface elevation data set Danielson and Gesch (2011) used for generating the CAM topographic boundary conditions.

## 4 Summary and Discussion

In this study, we applied an Arctic-refined variable-resolution grid to a coupled Earth system/ice sheet model, CESM2.2-CISM2.1, to investigate future, multicentury, climate and GrIS evolution. The variable-resolution grid has a horizontal resolution of 1/4° over the broader Arctic region and 1° elsewhere. The simulation was run under a multicentury idealized 4×$CO_2$ scenario and is compared with two other reference simulations under the same forcing scenario but using a lower resolution grid (1° lat-lon grid) to explore the impact of enhanced horizontal resolution.

Though with different magnitudes and timing, the response of the GrIS to the warming climate in the variable-resolution run is similar to what was found in Muntjewerf, Sellevold, et al. (2020). In the variable-resolution run, the global annual average near-surface temperature rises approximately linearly at a speed of 0.33 K per decade during 1% $yr^{-1}$ $CO_2$ increment. Polar amplification is 1.8, while GrIS amplification is much smaller (1.1). After $CO_2$ stabilization, the speed of global annual average near-surface temperature rise decreases more than 40 percents compared to the previous stage (0.19 K per decade). An acceleration of the GrIS mass loss is found at around year 110 (2.4 Gt $yr^{-2}$ before year 110 to 13.0 Gt $yr^{-2}$ during year 111-150), which is driven by faster SMB decrease. At this time, the expansion of the ablation area is large enough to trigger a large melt/albedo feedback, which reinforces the absorption of shortwave radiation and accelerates the melt. The increased sensible and latent heat fluxes also contribute to this process due to expanded and strengthened near-surface temperature inversion. By the end of the simulation, the ablation zone covers 57% of the ice sheet surface. The cumulative contribution from the GrIS to global mean sea level rise is 53 mm by year 150 and 831 mm by year 350, which is about 40% and 20% smaller compared to the 1° runs. The sea level rise contribution from our variable-resolution run by $CO_2$ stabilization is also small compared to other CESM simulations under the CMIP RCP8.5 and SSP5-8.5 scenarios by year 2100 (109 mm in Muntjewerf, Petrini, et al. (2020) and 76 mm in Lipscomb et al. (2013)), when the $CO_2$ concentration is close to 4×$CO_2$. If com-

pared to projections using GrIS models forced by outputs from CMIP5 GCMs (90±50 mm during 2015-2100; Goelzer et al., 2020), our estimation approaches the lower bound.

Compared to the 1° runs, the variable-resolution run has relatively slower MB and SMB decrease. This mainly originates from the smaller surface melt during summer in the variable-resolution run. The SMB difference between the simulations can be smaller than their difference in melt due to compensating terms, which stresses the importance of correctly modeling individual SMB components for making reliable projections of GrIS mass loss. The excessive melt in the 1° runs is concentrated in the western and northern transitional zones towards the margins, produced by the combined effect of greater net longwave and net shortwave radiation, with the latter playing a primary role. The larger net longwave radiation over the ice sheet peripheries in the 1° runs results from their larger and thicker cloud cover over these regions. The net shortwave radiation differences are a product of the stronger albedo feedback over the western and northern basins in the 1° runs. In coarser grids, stronger smoothing and flattening of topography due to grid resolution and necessity to prevent model from exciting grid-scale numerical modes leads to faster ablation zone expansion, thus stronger albedo feedback. Therefore, future sea level projections based on models with a coarse resolution may be biased high due to their inability of adequately resolving the Greenland topography.

Comparisons between these simulations are complicated by differences in grid resolution, physics time step and dynamical core (dycore). Similar to the effect of increasing resolution, reducing physics time step can also increase resolved vertical velocities and thus condensational heating. By comparing two AMIP style CESM2.2 simulations using the same quasi-uniform 1° SE grid but different time steps, Herrington et al. (2022) showed that the simulation with a reduced time step has a warmer troposphere over nearly all latitudes. Then by comparing two simulations using the same time step but different grids - the `Arctic` grid and the quasi-uniform 1° grid, Herrington et al. (2022) showed that the warmer temperature caused by enhanced resolution is confined to the refined Arctic region with a larger magnitude. Therefore, the differences of the simulated climate within the refined Arctic region in this study is more likely a result of changing the horizontal resolution though the impact from changing the physics time step cannot be eliminated. Since the SE dycore is less diffusive than the FV dycore, the resolved vertical velocities are larger in the SE dycore, which can also warm up the atmosphere. It is impossible to fully disentangle the impacts of changing resolution and dynamical core in the current simulations since these factors change simultaneously.

Another uncertainty in this study is the initial condition. The pre-industrial simulations of `ARCTIC` was branched off from an initial condition similar to the initial condition of the `F09M` 1% $CO_2$ simulation. The aim of this is to achieve a near equilibrium state of the GrIS after changing the grid. As a more direct comparison, `F09` went through a similar spin-up process as `ARCTIC`. The resulted initial ice sheet conditions before the start of the idealized warming period are different among the three simulations: `F09` has a larger initial ice volume than `ARCTIC`, while `F09M` has a smaller initial ice volume than `ARCTIC` (Fig.8d). We found that `ARCTIC` has slower SMB decrease and lower melt compared to the 1° runs in multicentury scale, no matter whether their initial ice volume is larger or smaller. Also, `ARCTIC` has a cooler pre-industrial climate than `F09M` and `F09`. The impact of this cooler climate is kept through the whole idealized warming simulation, which is reflected in Figure 6g-l. Moreover, we note that all the three simulations have small positive drifts of GrIS MB before the start of the warming scenario (Table 1). The cooler initial climate in `ARCTIC` results in a longer adjusting time for the GrIS to shift to mass loss, which degrades the specific projections of GrIS sea level rise contribution. However, our result suggests that the near-surface temperature is not the main driver for the different responses of the GrIS among the simulations. Considering all these, we can conclude that our finding is robust.

One limitation of the current model configuration lies in the ice-ocean interface. The direct impact of oceanic thermal forcing on ocean-terminating ice fronts is not included, and the floating criterion used in the calving parameterization is highly idealized. The limited understanding and implementation of processes such as calving and submarine melting in ice sheet models has been identified as a major source of uncertainties for future projections of the GrIS (Goelzer et al., 2020). Oceanic forcing can enhance solid ice discharge (Holland et al., 2008; Wood et al., 2018). Using another coupled Earth system/ice sheet model, EC-Earth-PISM, under the same 1% $yr^{-1}$ $CO_2$ warming scenario, Madsen et al. (2022) showed that even by embedding a constant oceanic thermal forcing and a simple geometric calving criterion, the ice discharge decrease is much smaller after 350 years. Most modeling studies that include oceanic forcing estimate a second order future sea level rise contribution from ice dynamics compared to SMB for the entire ice sheet (Price et al., 2011; Fürst et al., 2015; Aschwanden et al., 2019), but with improved bathymetry and bed topography mapping, Choi et al. (2021) showed that ice dynamics could contribute comparably as SMB or more to GrIS mass loss over this century. These studies illustrate the importance of properly including ice-ocean interactions for future GrIS projections at century to multicentury scale. Currently, the functionality of ice sheet-ocean interaction is under study in CESM and will be included in the future versions. The `Arctic` grid or grids with even higher-resolution refinement will also be helpful by providing a better resolved atmospheric forcing for modeling the ice dynamics in narrow fjords.

In the aggregate, our study demonstrates the value of employing variable-resolution grids for coupled climate-GrIS modeling, providing valuable insights into ice sheet-climate interactions. It underscores the critical role of grid resolution in modeling the evolution of the GrIS on multicentury time scales, particularly in capturing topography-related processes and feedbacks, and thus advances the projection of the GrIS' future sea level rise contribution.

**Acknowledgments**

AH and AG contributions to this material are supported by the National Center for Atmospheric Research (NCAR), a major facility sponsored by the NSF under Cooperative Agreement no. 1852977. Computing and data storage resources, including the Cheyenne supercomputer (Computational and Information Systems Laboratory, 2017), were provided by the Computational and Information Systems Laboratory (CISL) at NCAR, as part of the System for Integrated Modeling of the Atmosphere (SIMA) project. ZY, ACS, JT and RT are supported by the NSF (grant no. OPP 1952199) and HDR iHARP institute (grant no. 2118285).

## Open Research

The data presented in this manuscript are stored in https://doi.org/10.5281/zenodo.10685261, and the code for generating the plots are available at https://github.com/IceZYin/2022-VR-dynamic-GrIS.git.

## References

Aschwanden, A., Fahnestock, M. A., & Truffer, M. (2016). Complex greenland outlet glacier flow captured. *Nature communications*, *7*(1), 10524.

Aschwanden, A., Fahnestock, M. A., Truffer, M., Brinkerhoff, D. J., Hock, R., Khroulev, C., ... Khan, S. A. (2019). Contribution of the greenland ice sheet to sea level over the next millennium. *Science Advances*, *5*(6), eaav9396. Retrieved from https://www.science.org/doi/abs/10.1126/sciadv.aav9396 doi: 10.1126/sciadv.aav9396

Bambach, N. E., Rhoades, A. M., Hatchett, B. J., Jones, A. D., Ullrich, P. A., & Zarzycki, C. M. (2022). Projecting climate change in south america using variable-resolution community earth system model: An application to chile. *International Journal of Climatology*, *42*(4), 2514-2542. doi: https://doi.org/10.1002/joc.7379

Box, J. E., Fettweis, X., Stroeve, J. C., Tedesco, M., Hall, D. K., & Steffen, K. (2012, August). Greenland ice sheet albedo feedback: thermodynamics and atmospheric drivers. *The Cryosphere*, *6*(4), 821–839. Retrieved 2023-07-14, from https://tc.copernicus.org/articles/6/821/2012/ doi: 10.5194/tc-6-821-2012

Choi, Y., Morlighem, M., Rignot, E., & Wood, M. (2021). Ice dynamics will remain a primary driver of greenland ice sheet mass loss over the next century. *Communications Earth & Environment*, *2*(1), 26.

Cogley, J., Hock, R., Rasmussen, L., Arendt, A., Bauder, A., Braithwaite, R., ... Zemp, M. (2011, 01). Glossary of glacier mass balance and related terms. doi: 10.5167/uzh-53475

Computational and Information Systems Laboratory. (2017). *Cheyenne: HPE/SGI ICE XA System (Climate Simulation Laboratory), Boulder, CO: National Center for Atmospheric Research.* doi: 10.5065/D6RX99HX

Danabasoglu, G., Lamarque, J.-F., Bacmeister, J., Bailey, D. A., DuVivier, A. K., Edwards, J., ... Strand, W. G. (2020). The community earth system model version 2 (cesm2). *Journal of Advances in Modeling Earth Systems*, *12*(2), e2019MS001916. doi: https://doi.org/10.1029/2019MS001916

Danielson, J. J., & Gesch, D. B. (2011). Global multi-resolution terrain elevation data 2010 (gmted2010).

Datta, R. T., Herrington, A., Lenaerts, J. T. M., Schneider, D. P., Trusel, L., Yin, Z., & Dunmire, D. (2023). Evaluating the impact of enhanced horizontal resolution over the antarctic domain using a variable-resolution earth system model. *The Cryosphere*, *17*(9), 3847–3866. Retrieved from https://tc.copernicus.org/articles/17/3847/2023/ doi: 10.5194/tc-17-3847-2023

Enderlin, E. M., Howat, I. M., Jeong, S., Noh, M.-J., van Angelen, J. H., & van den Broeke, M. R. (2014). An improved mass budget for the greenland ice sheet. *Geophysical Research Letters*, *41*(3), 866-872. doi: https://doi.org/10.1002/2013GL059010

ESMF Joint Specification Team. (2021). *ESMF user guide* (Tech. Rep.).

Eyring, V., Bony, S., Meehl, G. A., Senior, C. A., Stevens, B., Stouffer, R. J., & Taylor, K. E. (2016). Overview of the coupled model intercomparison project phase 6 (cmip6) experimental design and organization. *Geoscientific Model Development*, *9*(5), 1937–1958. Retrieved from https://gmd.copernicus.org/articles/9/1937/2016/ doi: 10.5194/gmd-9-1937-2016

Fang, Z.-f. (2004). Statistical relationship between the northern hemisphere sea ice and atmospheric circulation during wintertime. In *Observation, theory and modeling of atmospheric variability. world scientific series on meteorology of east asia* (p. 131-141). Singapore: World Scientific Publishing Company. doi: 10.1142/9789812791139_0006

Fausto, R. S., & the PROMICE team*. (2018, Aug.). The greenland ice sheet–snowline elevations at the end of the melt seasons from 2000 to 2017. *GEUS Bulletin*, *41*, 71–74. Retrieved from https://geusbulletin.org/index.php/geusb/article/view/4346 doi: 10.34194/geusb.v41.4346

Fürst, J. J., Goelzer, H., & Huybrechts, P. (2015). Ice-dynamic projections of the greenland ice sheet in response to atmospheric and oceanic warming. *The Cryosphere*, *9*(3), 1039–1062. Retrieved from https://tc.copernicus.org/articles/9/1039/2015/ doi: 10.5194/tc-9-1039-2015

Fyke, J., Sergienko, O., Löfverström, M., Price, S., & Lenaerts, J. T. (2018). An overview of interactions and feedbacks between ice sheets and the earth system. *Reviews of Geophysics*, *56*(2), 361–408.

Gates, W. L. (1992). An ams continuing series: Global change–amip: The atmospheric model intercomparison project. *Bulletin of the American Meteorological Society*, *73*(12), 1962 - 1970. Retrieved from https://journals.ametsoc.org/view/journals/bams/73/12/1520-0477_1992_073_1962_atamip_2_0_co_2.xml doi: https://doi.org/10.1175/1520-0477(1992)073<1962:ATAMIP>2.0.CO;2

Gettelman, A., Callaghan, P., Larson, V. E., Zarzycki, C. M., Bacmeister, J. T., Lauritzen, P. H., ... Neale, R. B. (2018). Regional climate simulations with the community earth system model. *Journal of Advances in Modeling Earth Systems*, *10*(6), 1245-1265. doi: https://doi.org/10.1002/2017MS001227

Gettelman, A., Hannay, C., Bacmeister, J. T., Neale, R. B., Pendergrass, A. G., Danabasoglu, G., ... Mills, M. J. (2019). High climate sensitivity in the community earth system model version 2 (cesm2). *Geophysical Research Letters*, *46*(14), 8329-8337. doi: https://doi.org/10.1029/2019GL083978

Goelzer, H., Nowicki, S., Payne, A., Larour, E., Seroussi, H., Lipscomb, W. H., ... van den Broeke, M. (2020). The future sea-level contribution of the greenland ice sheet: a multi-model ensemble study of ismip6. *The Cryosphere*, *14*(9), 3071–3096. Retrieved from https://tc.copernicus.org/articles/14/3071/2020/ doi: 10.5194/tc-14-3071-2020

Goldberg, D. N. (2011). A variationally derived, depth-integrated approximation to a higher-order glaciological flow model. *Journal of Glaciology*, *57*(201), 157–170.

Guo, Z., Wang, M., Qian, Y., Larson, V. E., Ghan, S., Ovchinnikov, M., ... Zhou, T. (2015). Parametric behaviors of clubb in simulations of low clouds in the community atmosphere model (cam). *Journal of Advances in Modeling Earth Systems*, *7*(3), 1005-1025. Retrieved from https://agupubs.onlinelibrary.wiley.com/doi/abs/10.1002/2014MS000405 doi: https://doi.org/10.1002/2014MS000405

Haarsma, R. J., Roberts, M. J., Vidale, P. L., Senior, C. A., Bellucci, A., Bao, Q., ... von Storch, J.-S. (2016). High resolution model intercomparison project (highresmip v1.0) for cmip6. *Geoscientific Model Development*, *9*(11), 4185–4208. doi: 10.5194/gmd-9-4185-2016

Hanna, E., Cappelen, J., Fettweis, X., Mernild, S. H., Mote, T. L., Mottram, R., ... Hall, R. J. (2021). Greenland surface air temperature changes from 1981 to 2019 and implications for ice-sheet melt and mass-balance change. *International Journal of Climatology*, *41*(S1), E1336-E1352. doi: https://doi.org/10.1002/joc.6771

Hanna, E., Fettweis, X., & Hall, R. J. (2018, October). Brief communication: Recent changes in summer Greenland blocking captured by none of the CMIP5 models. *The Cryosphere*, *12*(10), 3287–3292. doi: 10.5194/tc-12-3287-2018

Hanna, E., Fettweis, X., Mernild, S. H., Cappelen, J., Ribergaard, M. H., Shuman, C. A., ... Mote, T. L. (2014, March). Atmospheric and oceanic climate forcing of the exceptional Greenland ice sheet surface melt in summer 2012: CLIMATE FORCING OF 2012 GREENLAND ICE MELT. *International Journal of Climatology*, *34*(4), 1022–1037. Retrieved 2023-08-28, from https://onlinelibrary.wiley.com/doi/10.1002/joc.3743 doi: 10.1002/joc.3743

Harris, L. M., Lin, S.-J., & Tu, C. (2016). High-resolution climate simulations using gfdl hiram with a stretched global grid. *Journal of Climate*, *29*(11), 4293 - 4314. Retrieved from https://journals.ametsoc.org/view/journals/clim/29/11/jcli-d-15-0389.1.xml doi: https://doi.org/10.1175/JCLI-D-15-0389.1

Herrington, A. R., Lauritzen, P. H., Lofverstrom, M., Lipscomb, W. H., Gettelman, A., & Taylor, M. A. (2022). Impact of grids and dynamical cores in cesm2.2 on the surface mass balance of the greenland ice sheet. *Journal of Advances in Modeling Earth Systems*, *14*(11), e2022MS003192. doi: https://doi.org/10.1029/2022MS003192

Herrington, A. R., & Reed, K. A. (2020). On resolution sensitivity in the community atmosphere model. *Quarterly Journal of the Royal Meteorological Society*, *146*(733), 3789-3807. doi: https://doi.org/10.1002/qj.3873

Holland, D. M., Thomas, R. H., De Young, B., Ribergaard, M. H., & Lyberth, B. (2008). Acceleration of jakobshavn isbræ triggered by warm subsurface ocean waters. *Nature geoscience*, *1*(10), 659–664.

Huang, X., Rhoades, A. M., Ullrich, P. A., & Zarzycki, C. M. (2016). An evaluation of the variable-resolution cesm for modeling california's climate. *Journal of Advances in Modeling Earth Systems*, *8*(1), 345–369.

Huang, X., & Ullrich, P. A. (2017). The changing character of twenty-first-century precipitation over the western united states in the variable-resolution cesm. *Journal of Climate*, *30*(18), 7555 - 7575. doi: https://doi.org/10.1175/JCLI-D-16-0673.1

Hunke, E., Lipscomb, W., Turner, A., Jeffery, N., & Elliott, S. (2015). *Cice: The los alamos sea ice model documentation and software user's manual, version 5.1. tech doc* (Tech. Rep.). T-3 Fluid Dynamics Group, Los Alamos National Laboratory, Tech. Rep. LA-CC-06-012.

Lauritzen, P. H., Bacmeister, J. T., Callaghan, P. F., & Taylor, M. A. (2015). Ncar_topo (v1.0): Ncar global model topography generation software for unstructured grids. *Geoscientific Model Development*, *8*(12), 3975–3986. Retrieved from `https://gmd.copernicus.org/articles/8/3975/2015/` doi: 10.5194/gmd-8-3975-2015

Lauritzen, P. H., Nair, R. D., Herrington, A. R., Callaghan, P., Goldhaber, S., Dennis, J. M., ... Tribbia, J. J. (2018). Ncar release of cam-se in cesm2.0: A reformulation of the spectral element dynamical core in dry-mass vertical coordinates with comprehensive treatment of condensates and energy. *Journal of Advances in Modeling Earth Systems*, *10*(7), 1537-1570. doi: https://doi.org/10.1029/2017MS001257

Lawrence, D. M., Fisher, R. A., Koven, C. D., Oleson, K. W., Swenson, S. C., Bonan, G., ... Zeng, X. (2019). The community land model version 5: Description of new features, benchmarking, and impact of forcing uncertainty. *Journal of Advances in Modeling Earth Systems*, *11*(12), 4245-4287.

Li, H., Wigmosta, M. S., Wu, H., Huang, M., Ke, Y., Coleman, A. M., & Leung, L. R. (2013). A physically based runoff routing model for land surface and earth system models. *Journal of Hydrometeorology*, *14*(3), 808 - 828. doi: https://doi.org/10.1175/JHM-D-12-015.1

Lin, S.-J. (2004). A "vertically lagrangian" finite-volume dynamical core for global models. *Monthly Weather Review*, *132*(10), 2293 - 2307. Retrieved from `https://journals.ametsoc.org/view/journals/mwre/132/10/1520-0493_2004_132_2293_avlfdc_2.0.co_2.xml` doi: https://doi.org/10.1175/1520-0493(2004)132<2293:AVLFDC>2.0.CO;2

Lipscomb, W. H., Fyke, J. G., Vizcaíno, M., Sacks, W. J., Wolfe, J., Vertenstein, M., ... Lawrence, D. M. (2013). Implementation and initial evaluation of the glimmer community ice sheet model in the community earth system model. *Journal of Climate*, *26*(19), 7352 - 7371. Retrieved from `https://journals.ametsoc.org/view/journals/clim/26/19/jcli-d-12-00557.1.xml` doi: https://doi.org/10.1175/JCLI-D-12-00557.1

Lipscomb, W. H., Price, S. F., Hoffman, M. J., Leguy, G. R., Bennett, A. R., Bradley, S. L., ... Worley, P. H. (2019). Description and evaluation of the community ice sheet model (cism) v2.1. *Geoscientific Model Development*,

*12*(1), 387–424. Retrieved from https://gmd.copernicus.org/articles/12/387/2019/ doi: 10.5194/gmd-12-387-2019

Lofverstrom, M., Fyke, J. G., Thayer-Calder, K., Muntjewerf, L., Vizcaino, M., Sacks, W. J., ... Bradley, S. L. (2020). An efficient ice sheet/earth system model spin-up procedure for cesm2-cism2: Description, evaluation, and broader applicability. *Journal of Advances in Modeling Earth Systems*, *12*(8), e2019MS001984. doi: https://doi.org/10.1029/2019MS001984

Madsen, M., Yang, S., Aðalgeirsdóttir, G., Svendsen, S., Rodehacke, C., & Ringgaard, I. (2022). The role of an interactive greenland ice sheet in the coupled climate-ice sheet model ec-earth-pism. *Climate Dynamics*, *59*(3-4), 1189–1211.

Mouginot, J., Rignot, E., Bjørk, A. A., Van den Broeke, M., Millan, R., Morlighem, M., ... Wood, M. (2019). Forty-six years of greenland ice sheet mass balance from 1972 to 2018. *Proceedings of the national academy of sciences*, *116*(19), 9239–9244.

Muntjewerf, L., Petrini, M., Vizcaino, M., Ernani Da Silva, C., Sellevold, R., Scherrenberg, M. D. W., ... Lofverstrom, M. (2020, May). Greenland Ice Sheet Contribution to 21st Century Sea Level Rise as Simulated by the Coupled CESM2.1-CISM2.1. *Geophysical Research Letters*, *47*(9), e2019GL086836. Retrieved 2023-09-26, from https://agupubs.onlinelibrary.wiley.com/doi/10.1029/2019GL086836 doi: 10.1029/2019GL086836

Muntjewerf, L., Sacks, W. J., Lofverstrom, M., Fyke, J., Lipscomb, W. H., Ernani da Silva, C., ... Sellevold, R. (2021). Description and demonstration of the coupled community earth system model v2 – community ice sheet model v2 (cesm2-cism2). *Journal of Advances in Modeling Earth Systems*, *13*(6), e2020MS002356. Retrieved from https://agupubs.onlinelibrary.wiley.com/doi/abs/10.1029/2020MS002356 doi: https://doi.org/10.1029/2020MS002356

Muntjewerf, L., Sellevold, R., Vizcaino, M., Ernani da Silva, C., Petrini, M., Thayer-Calder, K., ... Sacks, W. J. (2020). Accelerated greenland ice sheet mass loss under high greenhouse gas forcing as simulated by the coupled cesm2.1-cism2.1. *Journal of Advances in Modeling Earth Systems*, *12*(10), e2019MS002031. doi: https://doi.org/10.1029/2019MS002031

Nowicki, S. M. J., Payne, A., Larour, E., Seroussi, H., Goelzer, H., Lipscomb, W., ... Shepherd, A. (2016). Ice sheet model intercomparison project (ismip6) contribution to cmip6. *Geoscientific Model Development*, *9*(12), 4521–4545. Retrieved from https://gmd.copernicus.org/articles/9/4521/2016/ doi: 10.5194/gmd-9-4521-2016

Otosaka, I. N., Shepherd, A., Ivins, E. R., Schlegel, N.-J., Amory, C., van den Broeke, M. R., ... Wouters, B. (2023). Mass balance of the greenland and antarctic ice sheets from 1992 to 2020. *Earth System Science Data*, *15*(4), 1597–1616. doi: 10.5194/essd-15-1597-2023

Pollard, D., & Groups, P. P. (2000). Comparisons of ice-sheet surface mass budgets from paleoclimate modeling intercomparison project (pmip) simulations. *Global and Planetary Change*, *24*(2), 79–106.

Pope, V., & Stratton, R. (2002). The processes governing horizontal resolution sensitivity in a climate model. *Climate Dynamics*, *19*, 211–236.

Price, S. F., Payne, A. J., Howat, I. M., & Smith, B. E. (2011, May). Committed sea-level rise for the next century from Greenland ice sheet dynamics during the past decade. *Proceedings of the National Academy of Sciences*, *108*(22), 8978–8983. Retrieved 2023-09-19, from https://pnas.org/doi/full/10.1073/pnas.1017313108 doi: 10.1073/pnas.1017313108

Rahimi, S. R., Wu, C., Liu, X., & Brown, H. (2019). Exploring a variable-resolution approach for simulating regional climate over the tibetan plateau using vr-cesm. *Journal of Geophysical Research: Atmospheres*, *124*(8), 4490-4513. doi: https://doi.org/10.1029/2018JD028925

Rhoades, A. M., Huang, X., Ullrich, P. A., & Zarzycki, C. M. (2016). Characterizing sierra nevada snowpack using variable-resolution cesm. *Journal of Applied Meteorology and Climatology*, *55*(1), 173–196.

Rhoades, A. M., Ullrich, P. A., & Zarzycki, C. M. (2018). Projecting 21st century snowpack trends in western usa mountains using variable-resolution cesm. *Climate Dynamics*, *50*(1-2), 261–288.

Rignot, E., & Mouginot, J. (2012). Ice flow in greenland for the international polar year 2008–2009. *Geophysical Research Letters*, *39*(11). Retrieved from `https://agupubs.onlinelibrary.wiley.com/doi/abs/10.1029/2012GL051634` doi: https://doi.org/10.1029/2012GL051634

Roeckner, E., Brokopf, R., Esch, M., Giorgetta, M., Hagemann, S., Kornblueh, L., ... Schulzweida, U. (2006). Sensitivity of simulated climate to horizontal and vertical resolution in the echam5 atmosphere model. *Journal of Climate*, *19*(16), 3771–3791.

Rutt, I. C., Hagdorn, M., Hulton, N. R. J., & Payne, A. J. (2009). The glimmer community ice sheet model. *Journal of Geophysical Research: Earth Surface*, *114*(F2). Retrieved from `https://agupubs.onlinelibrary.wiley.com/doi/abs/10.1029/2008JF001015` doi: https://doi.org/10.1029/2008JF001015

Ryan, J. C., Smith, L. C., van As, D., Cooley, S. W., Cooper, M. G., Pitcher, L. H., & Hubbard, A. (2019). Greenland ice sheet surface melt amplified by snowline migration and bare ice exposure. *Science Advances*, *5*(3), eaav3738. Retrieved from `https://www.science.org/doi/abs/10.1126/sciadv.aav3738` doi: 10.1126/sciadv.aav3738

Sakaguchi, K., Leung, L. R., Zarzycki, C. M., Jang, J., McGinnis, S., Harrop, B. E., ... Mearns, L. (2023). Technical descriptions of the experimental dynamical downscaling simulations over north america by the cam–mpas variable-resolution model. *Geoscientific Model Development*, *16*(10), 3029–3081. Retrieved from `https://gmd.copernicus.org/articles/16/3029/2023/` doi: 10.5194/gmd-16-3029-2023

Schmidt, F. (1977). Variable fine mesh in spectral global models. *BEITR. PHYS. ATMOSPH.*, *50*, 211-217.

Sellevold, R., van Kampenhout, L., Lenaerts, J. T. M., Noël, B., Lipscomb, W. H., & Vizcaino, M. (2019). Surface mass balance downscaling through elevation classes in an earth system model: application to the greenland ice sheet. *The Cryosphere*, *13*(12), 3193–3208. Retrieved from `https://tc.copernicus.org/articles/13/3193/2019/` doi: 10.5194/tc-13-3193-2019

Sellevold, R., & Vizcaíno, M. (2020, September). Global warming threshold and mechanisms for accelerated greenland ice sheet surface mass loss. *Journal of Advances in Modeling Earth Systems*, *12*(9). Retrieved 2023-08-26, from `https://onlinelibrary.wiley.com/doi/10.1029/2019MS002029` doi: 10.1029/2019MS002029

Smith, R., Jones, P., Briegleb, B., Bryan, F., Danabasoglu, G., Dennis, J., ... others (2010). The parallel ocean program (pop) reference manual ocean component of the community climate system model (ccsm) and community earth system model (cesm). *LAUR-01853*, *141*, 1–140.

Staniforth, A. N., & Mitchell, H. L. (1978). A variable-resolution finite-element technique for regional forecasting with the primitive equations. *Monthly Weather Review*, *106*(4), 439 - 447. doi: https://doi.org/10.1175/1520-0493(1978)106<0439:AVRFET>2.0.CO;2

Straneo, F., & Heimbach, P. (2013). North atlantic warming and the retreat of greenland's outlet glaciers. *Nature*, *504*(7478), 36–43.

Tang, Q., Golaz, J.-C., Van Roekel, L. P., Taylor, M. A., Lin, W., Hillman, B. R., ... Bader, D. C. (2023). The fully coupled regionally refined model of e3sm version 2: overview of the atmosphere, land, and river results. *Geoscientific Model Development*, *16*(13), 3953–3995. Retrieved

from https://gmd.copernicus.org/articles/16/3953/2023/ doi: 10.5194/gmd-16-3953-2023

Tedesco, M., & Fettweis, X. (2020). Unprecedented atmospheric conditions (1948–2019) drive the 2019 exceptional melting season over the greenland ice sheet. *The Cryosphere*, *14*(4), 1209–1223. Retrieved from https://tc.copernicus.org/articles/14/1209/2020/ doi: 10.5194/tc-14-1209-2020

Trusel, L. D., Das, S. B., Osman, M. B., Evans, M. J., Smith, B. E., Fettweis, X., ... van den Broeke, M. R. (2018). Nonlinear rise in greenland runoff in response to post-industrial arctic warming. *Nature*, *564*(7734), 104–108.

van Kampenhout, L., Lenaerts, J. T. M., Lipscomb, W. H., Lhermitte, S., Noël, B., Vizcaíno, M., ... van den Broeke, M. R. (2020). Present-day greenland ice sheet climate and surface mass balance in cesm2. *Journal of Geophysical Research: Earth Surface*, *125*(2), e2019JF005318. Retrieved from https://agupubs.onlinelibrary.wiley.com/doi/abs/10.1029/2019JF005318 doi: https://doi.org/10.1029/2019JF005318

van Kampenhout, L., Rhoades, A. M., Herrington, A. R., Zarzycki, C. M., Lenaerts, J. T. M., Sacks, W. J., & van den Broeke, M. R. (2019). Regional grid refinement in an earth system model: impacts on the simulated greenland surface mass balance. *The Cryosphere*, *13*(6), 1547–1564. doi: 10.5194/tc-13-1547-2019

Vizcaíno, M., Mikolajewicz, U., Jungclaus, J., & Schurgers, G. (2010). Climate modification by future ice sheet changes and consequences for ice sheet mass balance. *Climate Dynamics*, *34*, 301–324.

Wijngaard, R. R., Herrington, A. R., Lipscomb, W. L., Leguy, G. R., & An, S.-I. (2023). Exploring the ability of the variable-resolution cesm to simulate cryospheric-hydrological variables in high mountain asia. *The Cryosphere Discussions*, *2023*, 1–39. Retrieved from https://tc.copernicus.org/preprints/tc-2022-256/ doi: 10.5194/tc-2022-256

Wood, M., Rignot, E., Fenty, I., Menemenlis, D., Millan, R., Morlighem, M., ... Seroussi, H. (2018). Ocean-induced melt triggers glacier retreat in northwest greenland. *Geophysical Research Letters*, *45*(16), 8334-8342. Retrieved from https://agupubs.onlinelibrary.wiley.com/doi/abs/10.1029/2018GL078024 doi: https://doi.org/10.1029/2018GL078024

Wu, C., Liu, X., Lin, Z., Rhoades, A. M., Ullrich, P. A., Zarzycki, C. M., ... Rahimi-Esfarjani, S. R. (2017). Exploring a variable-resolution approach for simulating regional climate in the rocky mountain region using the vr-cesm. *Journal of Geophysical Research: Atmospheres*, *122*(20), 10,939-10,965. doi: https://doi.org/10.1002/2017JD027008

Zängl, G., Reinert, D., & Prill, F. (2022). Grid refinement in icon v2.6.4. *Geoscientific Model Development*, *15*(18), 7153–7176. Retrieved from https://gmd.copernicus.org/articles/15/7153/2022/ doi: 10.5194/gmd-15-7153-2022

Zarzycki, C. M. (2016). Tropical cyclone intensity errors associated with lack of two-way ocean coupling in high-resolution global simulations. *Journal of Climate*, *29*(23), 8589 - 8610. doi: https://doi.org/10.1175/JCLI-D-16-0273.1

Zarzycki, C. M., & Jablonowski, C. (2014). A multidecadal simulation of atlantic tropical cyclones using a variable-resolution global atmospheric general circulation model. *Journal of Advances in Modeling Earth Systems*, *6*(3), 805-828. doi: https://doi.org/10.1002/2014MS000352

Zarzycki, C. M., Jablonowski, C., & Taylor, M. A. (2014). Using variable-resolution meshes to model tropical cyclones in the community atmosphere model. *Monthly Weather Review*, *142*(3), 1221 - 1239. doi: https://doi.org/10.1175/MWR-D-13-00179.1

Zarzycki, C. M., Jablonowski, C., Thatcher, D. R., & Taylor, M. A. (2015). Effects of localized grid refinement on the general circulation and climatology in the

community atmosphere model. *Journal of Climate*, *28*(7), 2777 - 2803. doi: https://doi.org/10.1175/JCLI-D-14-00599.1

# Supporting Information for "Improved Understanding of Multicentury Greenland Ice Sheet Response to Strong Warming in the Coupled CESM2-CISM2 with Regional Grid Refinement"

Ziqi Yin[1], Adam R. Herrington[2], Rajashree Tri Datta[1], Aneesh Subramanian[1], Jan T. M. Lenaerts[1], and Andrew Gettelman[3]

[1]Department of Atmospheric and Oceanic Sciences, University of Colorado Boulder, Boulder, CO, USA

[2]National Center for Atmospheric Research, Boulder, CO, USA

[3]Pacific Northwest National Laboratory, Richland, WA, USA

## Contents of this file

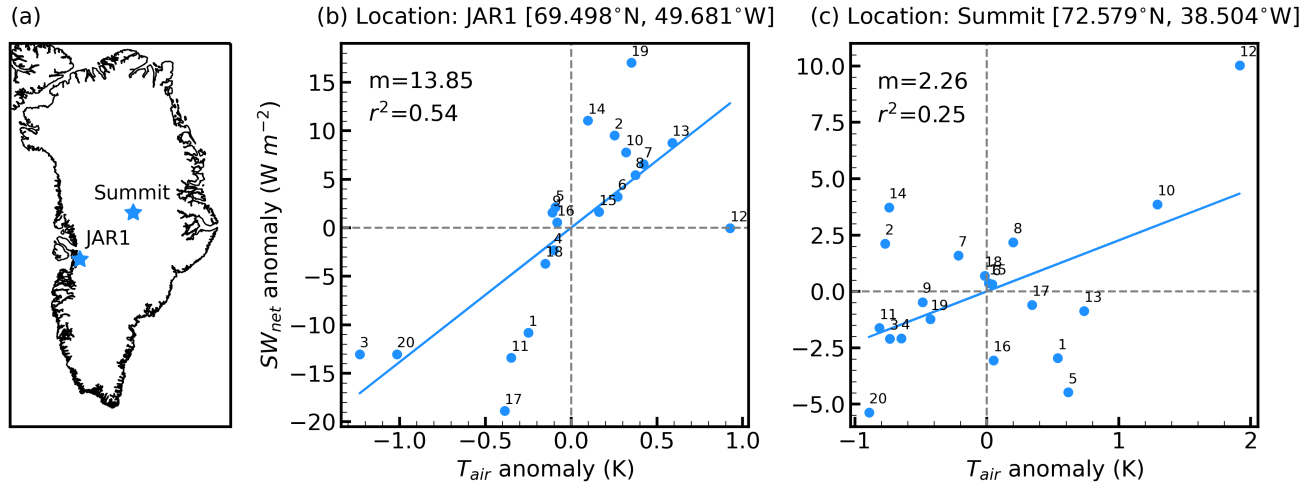


**Figure S1.** Examples of albedo feedback (W $m^{-2}$ $K^{-1}$) calculated by regression of inter annual anomalies. The locations of the two example GC-Net AWS sites (a), one at the ablation zone (JAR1) and the other at the accumulation zone (Summit). The regression of detrended net shortwave radiation and near-surface air temperature anomalies of the grid cell that contains the JAR1 site (b) and the Summit site (c) during $CO_2$ stabilization. The slope $m$ represents the albedo feedback value. The numbers over points represent the year number of the 20-year period.

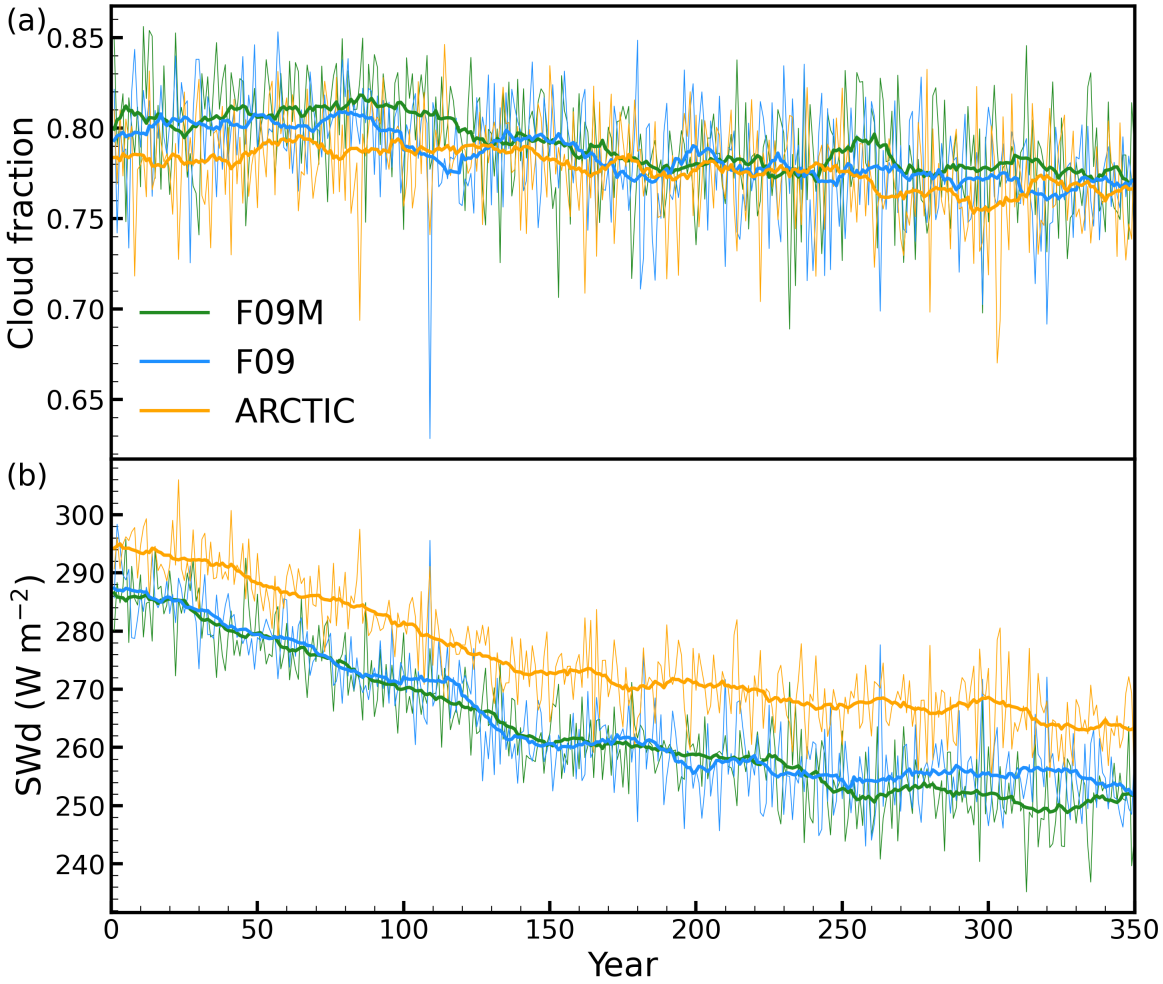


**Figure S2.** Evolution of the annual mean GrIS-averaged cloud fraction (a) and downward shortwave radiation (W m$^{-2}$) (b).

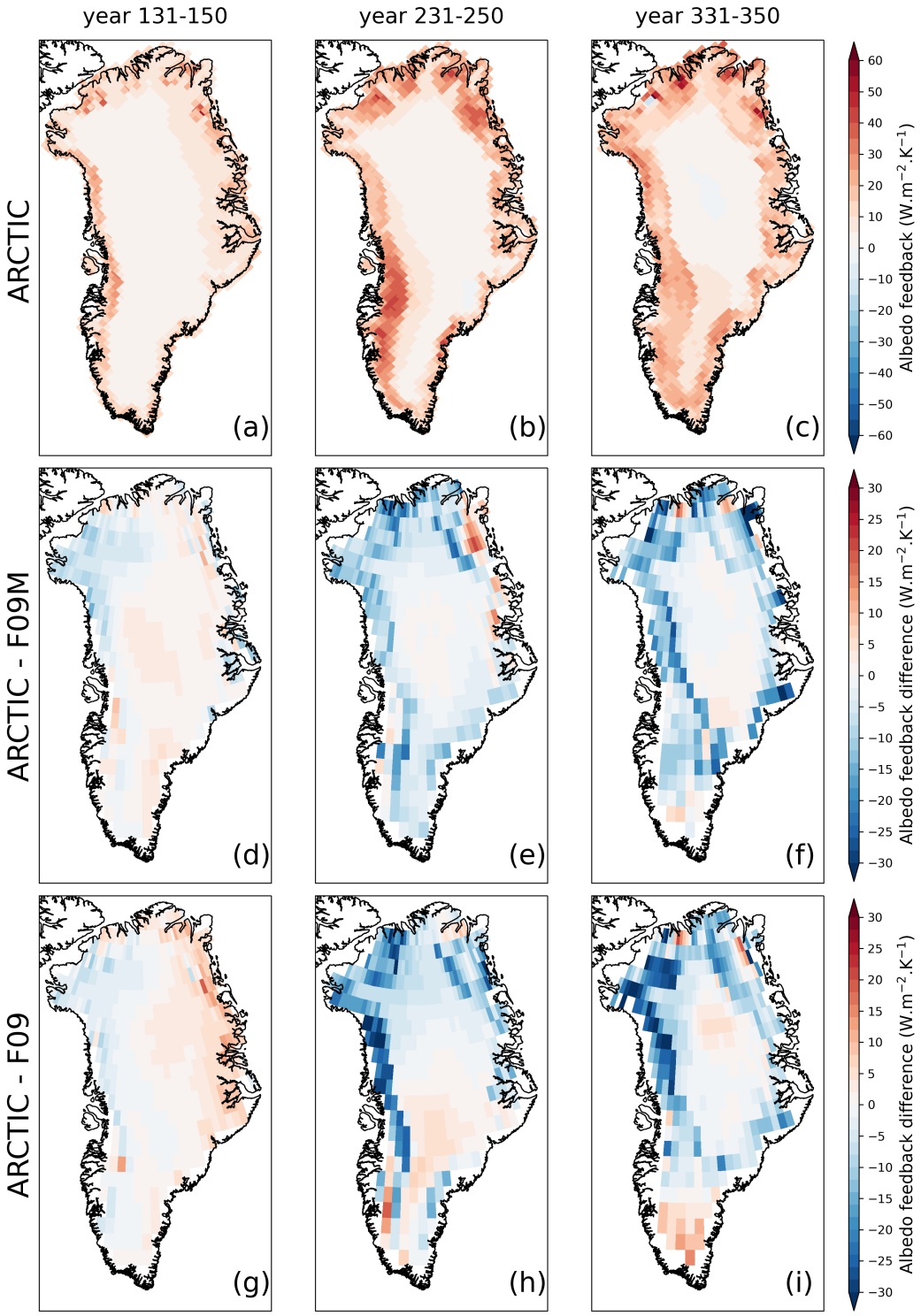


**Figure S3.** Maps of the albedo feedback (W m$^{-2}$ K$^{-1}$) defined by $\Delta' SW_n / \Delta' T_{air}$ of `ARCTIC` (a-c), and the difference between `ARCTIC` and `F09M` (d-f), `ARCTIC` and `F09` (g-i). The three columns from left to right represent averaged periods year 131-150, year 231-250, and year 331-350, respectively.